First Principles Study of Li-based Battery Materials: Electronic Structure, Thermodynamics, and Kinetics

INAUGURAL DISSERTATION

to obtain the academic degree
Doctor rerum naturalium (Dr. rer. nat.)

submitted to

The Department of Biology, Chemistry and Pharmacy

of Freie Universität Berlin

by

Sara Panahian Jand

from Iran

Berlin, 2018

This work was prepared under supervision of

Dr. Payam Kaghazchi (Freie Universität Berlin)

from

February 2014 until February 2018

1st Reviewer: Dr. Payam Kaghazchi

2nd Reviewer: Prof. Dr. Beate Paulus

Date of the defense: 13.06.2018

To my beloved Pouya...

Acknowledgements

The accomplishment of this dissertation would not have been possible at all without the help and support of many people. First, I would like to express my deepest gratitude to my supervisor Dr. Payam Kaghazchi for the chance to work on an exciting research topic and for his support and guidance with patience.

I would also like to express my sincere gratitude to Prof. Dr. Beate Paulus for kindly accepting to review my doctoral dissertation, and her precise and insightful comments and discussions.

For the nice time at the Freie Universität Berlin, I like to appreciate all my colleagues and friends. Many thanks to all the members of the AG Kaghazchi, Pouya, Ashkan, Qian, Melissa and Quan. Also, I am grateful to Prof. Dr. Christina Roth and her research group with whom I had many fruitful discussions led to a successful collaboration. Thanks for a friendly atmosphere during small talks in the coffee kitchen which AG Roth kindly shared with our group. I would like to appreciate Mrs. Julija Djordjevic for all her administrative works specially at the beginning of my PhD studies. I also thank all my friends at Physical and Theoretical Chemistry Group, Francesca, Matthias, Davood, Thomas, Claudia, Tintula, Marcus, Jonathan, Öznur, all who are parts of “healthy Wednesday” lunches and of course “Yoga” sessions.

In addition, I acknowledge the financial support by the Bundesministerium für Bildung und Forschung (BMBF) for this research. Also, the support of the Zentraleinrichtung für Datenverarbeitung (ZEDAT) at the Freie Universität Berlin is gratefully acknowledged.

Most importantly, none of this would have been possible without the patience and encouragement of my family. To my Mom and Dad, and my Aunt who gave me the chance to follow my goals in life, thank you for providing me with all of your unconditional love and support. There are no words to describe how much I love and respect you.

Moreover, I want to thank my lifelong friend Sara, who has always been the closest to me while we are in two differnt parts of the world. Thanks for all the moments that we spent and enjoyed together. You are more than a friend.

Finally, a very special thank goes to my dearest Pouya for continuously and patiently supporting me in every phase of this dissertation. Without you, I would never have finished successfully.

Contents

List of Tables

List of Figures

Chapter 1

INTRODUCTION

Energy-storage devices play a significant role in the future's energy supply, particularly in large-scale renewable energy technologies and transportation. Lithium(Li)-based batteries as one kind of the rechargeable energy-storage systems are widely used in electric vehicles and many portable electronic devices such as cell phones and laptop computers. In addition, the renewable wind and solar energies are intermittent and they need to be connected to Li-based batteries in order to store the energy [1].

The rechargeable batteries are electrochemical devices in which the electrical energy is stored in the form of chemical energy. In Li-ion battery (LIB), low atomic weight of Li, as well as its high electrode potential compared to hydrogen electrode (-3.04 V [2]), results in high energy density. In general, LIBs have taken a large part of market not only because of its high energy density, but also due to its long cyclic life and low self-discharge rate [1,3,4]. However, the new generation of rechargeable batteries needs more research and improvement in order to meet the market demands for even higher energy density, low cost, and improved safety [3,4]. It is hoped that through the combination of theoretical and experimental investigations, researchers can develop the new generation of improved rechargeable batteries. Therefore, the goal of this thesis is to provide a detailed study on several promising materials in Li-based batteries using computational techniques. Two important types of Li-based batteries which are mainly described in this dissertation are lithium-sulfur (Li-S) batteries and all-solid-state Li-ion batteries (ASSLB). Li-S batteries have a high theoretical energy density ($2800\,\mathrm{WhL}^{-1}$) [3,5]. This property, besides the low cost of S and low atomic weight of Li, makes Li-S battery a promising candidate for large-scale applications and transportation systems. In ASSLBs, the replacement of liquid electrolytes by solid electrolytes increases the safety and flexibility in design of such batteries.

1.1 Lithium-ion battery (LIB)

The first rechargeable LIB was developed by Goodenough *et al.* in 1980 [6]. A LIB consists of one or more electrochemical cells which can be connected in parallel or in series. Main components of each electrochemical cell are two electrodes and an electrolyte which is an ionic conductor and electronic insulator. The anode is the negative electrode in which Li oxidation takes place and the electrons get free during discharge process. Most cells commonly employ a carbon- or graphite-based anode. The positive electrode is the cathode where during discharge process, Li is reduced and the electrons coming from the anode are taken up. The cathode is usually a lithium metal oxides, LiMO$_2$ (M: Co, Mn, Ni, etc.). Upon discharging, Li ions migrate from the anode to the Li-based cathode. Simultaneously, electrons move from the anode to the cathode through the external circuit. The reverse process occurs during charging. The schematic view of a typical LIB during charge process is shown in figure 1.1. Electrode reactions that occur in a LIB consisting of graphite and LiMO$_2$ electrodes are:

$$\begin{aligned}
&\text{Anode reaction}: \mathrm{C}_n + x\mathrm{Li}^+ + x\mathrm{e}^- \underset{\text{discharge}}{\overset{\text{charge}}{\rightleftarrows}} \mathrm{Li}_x\mathrm{C}_n \qquad (1.1.1)\\
&\text{Cathode reaction}: \mathrm{LiMO}_2 \underset{\text{discharge}}{\overset{\text{charge}}{\rightleftarrows}} \mathrm{Li}_{1-x}\mathrm{MO}_2 + x\mathrm{Li}^+ + x\mathrm{e}^-\\
&\text{Overall reaction}: \mathrm{C}_n + \mathrm{LiMO}_2 \underset{\text{discharge}}{\overset{\text{charge}}{\rightleftarrows}} \mathrm{Li}_x\mathrm{C}_n + \mathrm{Li}_{1-x}\mathrm{MO}_2
\end{aligned}$$

In reality, besides the mentioned reactions, several side reactions occur during charge/discharge cycle and consume Li ions and/or active electrode materials. For example, during the first

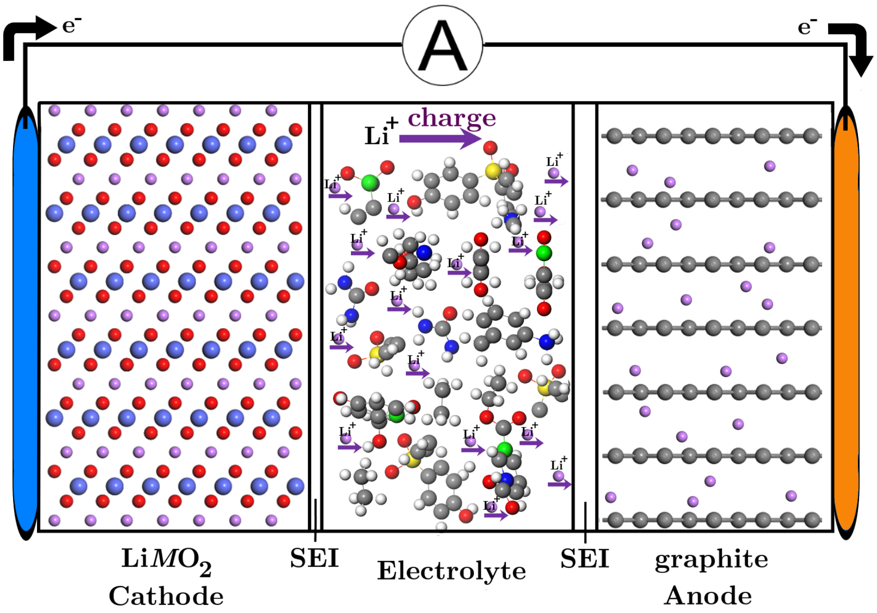

Figure 1.1: Schematic view of a typical LIB upon charging. During charging process, Li ions move from cathode to the anode through electrolyte, while they move in opposite direction during discharging.

charging cycles a solid electrolyte interphase (SEI) is generated on the surface of electrodes (usually anode) due to reduction or oxidation of electrolyte species [7, 8](as shown in figure 1.1). The formation of SEI layer is irreversible and results in a loss of capacity. In addition, the Li^+ diffusion rate through SEI layer is lower than in the electrolyte and electrodes. On the other hand, SEI layer acts as an electronically insulating protective layer between the electrolyte and the electrode, and prevents further undesired decomposition of the electrolyte. Hence, it is essential in the performance of LIBs [9].

1.2 Lithium-Sulfur Batteries

As shown in figure 1.2, a Li-S battery works based on the electrochemical dissolution of lithium from metal Li anode and lithiation of sulfur at S cathode during discharge cycles. In reverse, delithiation of sulfur from S cathode and deposition of lithiums at the anode occur while charging. Naturally, S exists in the form of ring structure with eight atoms, S_8, and its reduction in a Li-S battery is a multistep process accompanied by the formation of various Li-polysulfides as intermediate products:

$$S_8 \rightarrow Li_2S_8 \rightarrow Li_2S_6 \rightarrow Li_2S_4 \rightarrow Li_2S_2 \rightarrow Li_2S.$$

During the discharge process, long-chain Li-polysulfides which are soluble in the electrolyte are reduced to the insoluble Li_2S_2 and Li_2S. In addition, migration of the Li-polysulfides to the Li anode (shuttle effect) can form an electronically inactive layer of Li_2S_2 and Li_2S on Li that can obstruct the diffusion of Li^+ into the electrolyte. Consequently, this leads to a hindrance in further reduction of sulfur, and it results in a poor utilization of active material. Moreover, the shuttle effect causes an irreversibe capacity fade as well as poor coulombic efficiency and degradation of the Li anode.

Theoretically, a cell with the Li anode can provide the greatest energy among all rechargeable batteries [3]. However the reactions between liquid electrolytes and Li electrode during charge/discharge cycles form a moss-like Li dendrite with a large surface area. When the dendrite grows and reaches the opposite electrode, the short circuit occurs. Then, the current density passing through this dendrite can quickly increase the temperature up to the melting point of metallic Li, and under this situation, explosion ("thermal runaway") may happen. As mentioned, the safety issue is one of the technical barriers for commercialization of the Li-S

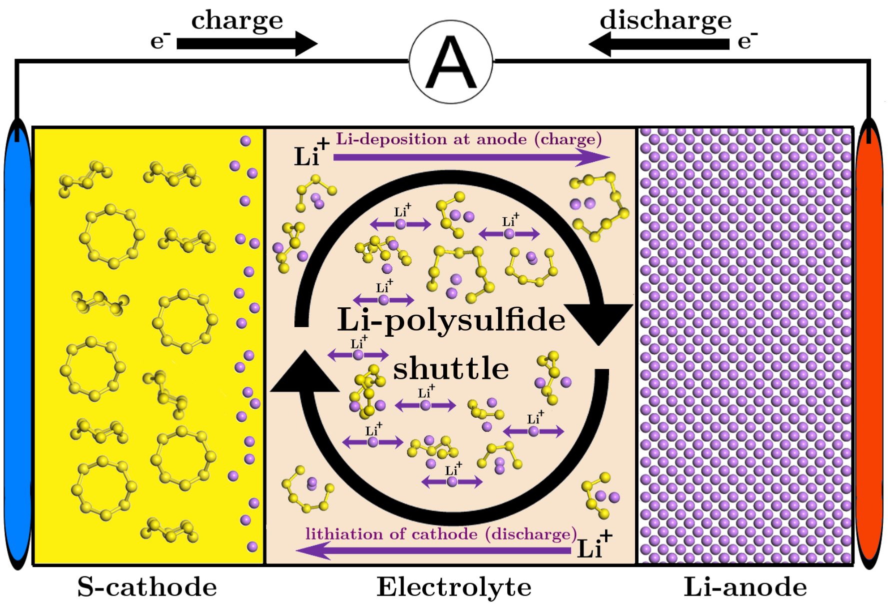

Figure 1.2: Schematic view of a typical Li-S battery and mechanism of the shuttle effect.

batteries. In recent years, researchers have proposed various methods to overcome the shortcomings and improve the performance of the Li-S batteries. Some of these approaches have been focused on the electrolyte and its particular Li salts that can decrease the shuttle effect. There are several experimental studies that have examined the effect of different Li salts, such as lithium hexafluorophosphate ($LiPF_6$), in the electrolyte of the Li-S batteries [10–16]. In addition, in a few theoretical works, the structures of Li-polysulfides in the solvent-salt complex have been studied using density functional theory (DFT) [17–19]. Furthermore, employing a solid-state electrolyte can suppress the Li anode degradation and improve the safety in the Li-S batteries. Different electrolyte materials such as Lithium borohydride (LiBH4) [20], polymer electrolytes [21, 22], and Li_2S/P_2S_5-based electrolytes [23–26] have been recently proposed as promising candidates in all-solid-state Li-S batteries. An alternative approach to enhance the electrochemical performance in Li-S batteries is to design electrically conductive cathode materials which can hinder the shuttle effect. This issue will be discussed in more details in the next section.

1.2.1 Cathode Materials in Li-S Batteries

In the early Li-S batteries, a simple mixture of carbon and sulfur was used as a cathode. These cells had low capacity due to low electrical conductivity of S. In 1989, Peled $et\ al.$ [27] introduced loading S on the porous structures of carbon to have a more efficient electronic contact. Afterwards, different approaches were proposed to improve the electrical conductivity of cathode material such as using carbon-coated sulfur cathodes [28], sulfur/multiwalled carbon nanotube (S/MWCNT) composites [29], S encapsulated in porous carbon nanofibers [30–32]. However, adding more carbon to S cathode decreases the energy density. In general, electrically conductive materials with an especial closed structures, such as carbon nanofibers, are good candidates for the cathode in Li-S batteries. In these closed structures, Li-polysulfides can be encapsulated and immobilized. Furthermore, coated layers on anode or cathode can adsorb the

Li-polysulfides and minimize the shuttle effect. Although several experimental researches have been carried out to diminish the shuttle effect, studying the adsorption of Li-polysulfides at the atomic scale is still challenging. Previously, the DFT calculations have been performed to investigate the structures and stabilities of Li-polysulfides in vacuum and electrolyte [18, 33, 34]. However, the mechanism of the Li-polysulfides adsorption on the cathode or the anode has not been established yet. In particular, there is a possibilty of the Li-polysulfides trapping by graphene in cathode which should be investigated at the atomistic level of details.

In the conventional Li-S battery, S cathode has to be paired with metallic Li anode as the only source of Li. The replacement of S with Li_2S as a cathode material in Li-S battery can provide the possibility of employing the Li-free anodes (such as graphite, Si, Sn). Therefore, the Li dendrites formation is avoided, and eventually the safety of the battery is improved. Li_2S has a high theoretical capacity of 1166 $mAhg^{-1}$, but poor conductivity. Therefore, carbon additives have been used to enhance the electrical conductivity of Li_2S-based cathodes [35–38]. In addition, ionic conductivity in Li-based compounds has a key role in their applications in Li-based batteries. Non-defective Li_2S has a low ionic conductivity at room temperature [39, 40], but combining this material with other solid composites results in promising electrolyte which can hinder the Li-polysulfide migration and increase the energy capacity [23–26, 41, 42].

Superionic conducting behavior of Li_2S at high temperatures has been first observed by Altorfer $et\ al.$ [39, 40] through the quasielastic neutron scattering study. However, Li-ion conductivity in Li_2S has not been theoretically studied so far.

1.3 All-Solid-State Li-Ion Batteries

An answer to the safety problem associated with the Li anode degradation can be using the solid-state electrolytes. This type of electrolytes can improve safety and cyclic performance of batteries by protecting the Li anode from dendrite formation and eventually avoiding the short-circuit [43,44]. Therefore, solid-state electrolytes are promising substitutes for the conventional liquid electrolytes.

Along with a high ionic conductivity (more than 10^{-4} S cm^{-1} at room temperature), a potential solid electrolyte material must have a chemical and electrochemical stabilities. Additionally, it should be non-toxic and inexpensive to be employed in the commercial all-solid-state Li-ion batteries (ASSLB). There are various types of solid-state Li-ion conductors, but most of them cannot be referred to as a standard solid electrolyte in commercial applications. Some examples of common solid-electrolyte materials are perovskite-type oxides such as lithium lanthanum titanate (LLTO) [45,46], sulfide-based glass/ceramic such as Li_2S–P_2S_5 [47,48], and garnet-type materials [49,50]. Garnet-type solid-state electrolytes have attracted an increasing interest in the last decade due to their high ionic conductivity and excellent environmental stability [49,51,52].

1.3.1 Garnet-Type Lithium Ion Conductors

Although the garnet-type materials have been well-understood structures, the first Li-ion conducting garnet oxide, $Li_5La_3M_2O_{12}$ (M = Nb, Ta), was reported by Thangadurai $et\ al.$ in 2003 [49]. The Li garnet structure has the general formula of $Li_xA_3B_2O_{12}$ ($5 \leq x \leq 7$) in which A and B can be substituted by different metal ions such as A = La, Ba, Sr, etc and B = Zr, Nb, Ta, etc [51–55]. The neutron diffraction studies have shown that in these structures Li ions are located on both octahedral and tetrahedral sites, and vacancies also exist on both sites (as illustrated in figure 1.3) [56,57]. One of the most promising Li garnet material is $Li_7La_3Zr_2O_{12}$ (LLZO) which has been synthesized by Murugan $et\ al.$ in 2007 [54]. This structure has relatively high stability against metallic Li due to its low reduction rate in contact with Li anode. LLZO is known to have two polymorphs with the cubic [54, 58–60] and tetragonal symmetry [61,62]. The ionic conductivity was reported to be 10^{-6} S cm^{-1} for tetragonal structure [54] and greater than 10^{-4} S cm^{-1} for cubic structure at room temperature [62–65], which is quite proper for thin film batteries. A problem of LLZO is that the cubic phase is not stable and with-

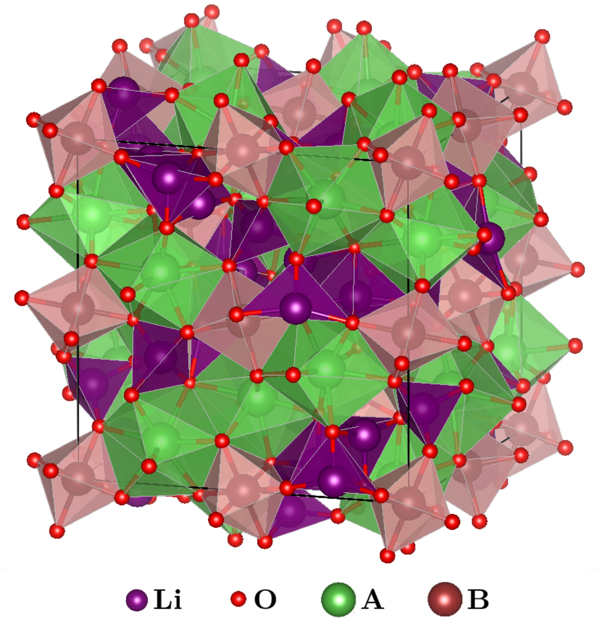

Figure 1.3: Crystal structure of cubic Li garnet oxide ($\mathrm{Li}_xA_3B_2\mathrm{O}_{12}$).

out doping with Al_2O_3 or Ga_2O_3 during synthesis process, a tetragonal phase is produced [60]. Cubic LLZO doped by Al_2O_3 has been reported to have the ionic conductivity of 4×10^{-4} S cm^{-1} [60], and the conductivity of LLZO stabilized with Ga_2O_3 is 5.4×10^{-4} S cm^{-1} [66].

Despite high Li-ion conductivity, ASSLBs constructed from these garnet materials have not been commercialized yet. Many experimental studies have reported a high interfacial resistance between LLZO and electrode materials [67–70]. Using energy dispersive X-ray spectroscopy (EDS) analysis, a cross diffusion of elements at the interface of LLZO (electrolyte) and $LiCoO_2$ (cathode) has been shown by Ogumi *et al.* [71]. In a recently published paper, confirming the formation of an intermediate layer at the interface of LLZO/$LiCoO_2$, Goodenough *et al.* [72] have proposed a surface modification of LLZO to improve the electrochemical performance at the interface. Despite all experimental studies on the interface of solid electrolyte/electrode, there are still several unclear interface properties which have not been understood yet. This originates from the failure of existing experimental techniques to elucidate the electronic structure as well as lack of theoretical studies at such interfaces. Recently, a few theoretical works have been dedicated to investigate the solid-solid interfaces in the Li batteries. Using DFT calculations, the possibility of the interfacial layer formation at LLZO/Li has been shown by Ma $et\ al.$ [73]. In this paper, the potential energies for the cubic and tetragonal structures of $Li_xAl_{0.25}La_3Zr_2O_{12}$ have been calculated and compared with each other [73]. In addition, Siegel $et\ al.$ have studied the interfacial resistance at LLZO/Li via DFT calculations [74, 75]. However, due to the large-size unit cell of LLZO, studying the interface between LLZO and other complex system is a challenging task. Accordingly, the electronic and atomic structure of LLZO/cathode interface have not been reported so far.

1.4 Goals of This Thesis

The present work focuses on problems and issues in LIB as future energy storage devices, specially Li-S batteries and ASSLBs. The main idea is that *first-principles* methods, in particular DFT calculations, can be applied to investigate the electronic structure of Li-based systems in order to better understand different mechanisms in LIB during charge/discharge cycles.

This thesis is organized into five chapters:

After current introduction, chapter 2 is dedicated to the theoretical background of the methods used in the present study. This chapter provides a brief insight into the many-body problem and DFT. Also the basics of DFT application in solids, some thermodynamic properties, and *ab initio* molecular dynamics (AIMD) simulations are described in details.

In chapter 3, using DFT calculations the adsorption of Li_2S_x polysulfides on pristine and defective graphene is studied, and the atomic structures, binding energies, dispersion interactions, and Gibbs free energies for these systems are presented. These findings lead to determination of more suitable candidates for the cathode materials in Li-S batteries.

Furthermore, in chapter 4, regarding the fact that Li diffusion in Li_2S cathode material is an important process in the performance of the LIB, the mechanism of superionic phase transition in Li_2S is presented. Also combining AIMD and DFT calculations, Li-ion conductivity is calculated and compared with experimental results.

In the case of ASSLBs, the computational simulation is expected to clarify the properties of solid electrolyte/electrode interface. Therefore, in chapter 5 the electronic and atomic structures as well as ion distribution at a model system for the electrolyte/electrode interface, namely the LLZO/$LiCoO_2$ interface, are investigated. Moreover, we study the possibility of cation interchange, which is assumed to be the reason for low rate of Li diffusion at the interface. Using different exchange-correlation functionals, bulk LLZO and bulk $LiCoO_2$, which include cation interchange, are optimized to minimize the stress induced by cation defect. Then, it is shown whether stress on the interface can change the possibilty of cation interchange at this system. The presented approach can also be used to study other complex solid/solid interfaces in ASSLBs.

Chapter 2

THEORETICAL BACKGROUND AND METHODS

2.1 Introduction

In the beginning of the twentieth century, classical mechanics was seriously challenged on relativistic and microscopic aspects [76, 77]. Physicists came to the conclusion that classical mechanics could not correctly explain the phenomena at speeds comparable to that of light, as well as the behavior of subatomic particles such as the electrons. In these years, the series of breakthroughs, from Planck's quantum concept, and Einstein's proposition on photons, to Bohr's model for hydrogen atom motivated scientists to find theoretical foundation behind these new ideas [78, 79]. Finally, in the mid-1920s, Heisenberg and Schrödinger independently developed formulations of quantum mechanics to describe electronic structures of microscopic systems [76, 79]. Heisenberg proposed his formulation as a matrix eigenvalue problem [80], while Schrödinger described the motion of microscopic particles by means of a wave function [81]. Both formulations work only for nonrelativistic phenomena, and despite their differences, represent the same concept from different perspectives. The Schrödinger equation is one of the cornerstones in quantum mechanics. The non-relativistic time-dependent Schrödinger equation is written as follows:

$$i\hbar\frac{\partial\psi(\mathbf{r},\sigma,t)}{\partial t} = \hat{H}\psi(\mathbf{r},\sigma,t), \tag{2.1.1}$$

where $\hat{H}$ is the Hamiltonian operator, and $\psi(\mathbf{r},\sigma,t)$ is the wave function which describes the state of any physical system at time t with σ as the spin coordinates and $\mathbf{r}$ as the position of all particles. The Hamiltonian for a particle of mass m moving in a time-dependent potential $V(\mathbf{r},t)$ is given by

$$\hat{H} = \frac{\hat{\mathbf{P}}^2}{2m} + \hat{V}(\mathbf{r},t), \tag{2.1.2}$$

where the first term is kinetic energy operator and $\hat{P} = i\hbar\nabla$. The Schrödinger equation has the following form:

$$i\hbar\frac{\partial\phi(\mathbf{r},\sigma,t)}{\partial t} = -\frac{\hbar^2}{2m}\nabla^2\phi(\mathbf{r},\sigma,t) + \hat{V}(\mathbf{r},t)\phi(\mathbf{r},\sigma,t), \tag{2.1.3}$$

in which $\phi(\mathbf{r},\sigma,t)$ represents the one-particle orbital with spin σ at position $\mathbf{r}$ and time t. If we consider the special case of time-independent potentials: $\hat{V}(\mathbf{r},t) = \hat{V}(\mathbf{r})$, the spatial and the spin parts of the orbital can be treated separately from its time-dependent part.

2.2 Many-Body Problem

In general, the systems of interest in quantum chemistry and solid-state physics consist of many particles. These systems are usually described by many-body time-independent Hamiltonian which takes the form as: (the atomic units are employed from now on throughout this thesis.)

$$\begin{aligned}\hat{H} = &-\sum_{i=1}^{N}(\frac{1}{2}\nabla_i^2) - \sum_{I=1}^{M}(\frac{1}{2M_I}\nabla_I^2) \\ &-\sum_{i=1}^{N}\sum_{I=1}^{M}\frac{Z_I}{|\mathbf{r}_i - \mathbf{R}_I|} + \sum_{i=1}^{N}\sum_{j>i}^{N}\frac{1}{|\mathbf{r}_i - \mathbf{r}_j|} + \sum_{I=1}^{M}\sum_{J>I}^{M}\frac{Z_I Z_J}{|\mathbf{R}_I - \mathbf{R}_J|},\end{aligned} \tag{2.2.1}$$

where the indices i, j are used for electrons and I, J are used for atomic nuclei. M_I denotes nuclear masses. $\mathbf{R}_I$ and $\mathbf{r}_i$ stand for nuclear and electron coordinates, respectively, and Z_I denotes atomic number.

The exact solution to time-independent many-body Schrödinger equation is only possible for a few very small systems like hydrogen atom. Therefore, different approximations should be considered for real systems.

2.3 Born-Oppenheimer Approximation

In 1927, Max Born and J. Robert Oppenheimer [82] justified that the molecular wave function of a system consisting of nuclei and electrons can be approximated as

$$\Psi = \psi_{\mathrm{el}}\psi_{\mathrm{nucl}}, \tag{2.3.1}$$

which means that the electron and the nucleus states can be treated separately in Schrödinger equation. The main idea of Born-Oppenheimer (BO) approximation is that the nuclei are more massive than electrons, so their velocities are comparatively lower. Therefore, the electrons can be assumed to be completely relaxed at any moment of atomic movement, and nuclei moving in much slower velocities seem static to the electrons. Considering BO approximation, the many-body problem is reduced to the problem of electrons moving in an external field which is due to static nuclei. Thus, the many-body, time-independent purely-electronic Hamiltonian is given by

$$\hat{H}_{\mathrm{el}} = -\frac{1}{2}\sum_{i=1}^{N}\nabla_i^2 + \sum_{i=1}^{N}\sum_{j>i}^{N}\frac{1}{|\mathbf{r}_i - \mathbf{r}_j|} - \sum_{i=1}^{N}\sum_{I=1}^{M}\frac{Z_I}{|\mathbf{r}_i - \mathbf{R}_I|}, \tag{2.3.2}$$

and

$$\hat{H}_{\mathrm{el}}\psi_{\mathrm{el}}(\mathbf{r}) = E_{\mathrm{el}}\psi_{\mathrm{el}}(\mathbf{r}). \tag{2.3.3}$$

In Eq. 2.3.2, the first term is kinetic energy operator, the second term represents the electron-electron repulsion, and the last term represents the electron-ion interaction (external potential). Then, the electronic energy including internuclear repulsion is obtained by

$$E_{\mathrm{el+nucl}} = E_{\mathrm{el}} + \sum_{I=1}^{M}\sum_{J>I}^{M}\frac{Z_I Z_J}{|\mathbf{R}_I - \mathbf{R}_J|}. \tag{2.3.4}$$

As most of the problems that we deal with in Chemistry and Physics focus on the electronic part, from now on the $\hat{H}$ and E will be used instead of $\hat{H}_{\mathrm{el}}$ and E_{el}, respectively. In Eq. 2.3.2, the electron-electron Coulomb repulsion term introduces the correlated motion of electrons.

Therefore, the Schrödinger equation cannot be exactly solved for a system with more than a few electrons! That is, although the BO approximation is a great step forward to solve the Schrödinger equation, further approximations are still needed.

2.4 Hartree-Fock Approach

In the Hartree method [83], the wave function of an N-electron system is approximated by a set of N orthogonal spin orbitals $\phi_i(\mathbf{x})$:

$$\psi(\mathbf{x}) \equiv \psi_{\mathrm{H}}(\mathbf{x}_1, \mathbf{x}_2, ..., \mathbf{x}_N) = \phi_1(\mathbf{x}_1)\phi_2(\mathbf{x}_2)...\phi_N(\mathbf{x}_N), \tag{2.4.1}$$

where the electronic variable $\mathbf{x}$ includes the spatial coordinate $\mathbf{r}$ as well as the spin coordinate σ. $\phi_i(\mathbf{x})$ is the single-electron orbital that describes both the spatial and the spin parts. In this approach, the N-electron wave function is approximated by a simple product which is not suitable for describing fermions. However, in the Hartree-Fock (HF) approach [84, 85], an antisymmetrized wave function of the N-electron system which can be written as a Slater determinant [86] is used instead of a simple product of spin orbitals $\phi_i(\mathbf{x})$:

$$\psi(\mathbf{x}) \equiv \psi_{\mathrm{HF}}(\mathbf{x}_1, \mathbf{x}_2, ..., \mathbf{x}_N) = \frac{1}{\sqrt{N!}} \begin{vmatrix} \phi_1(\mathbf{x}_1) & \phi_1(\mathbf{x}_2) & ... & \phi_1(\mathbf{x}_N) \\ \phi_2(\mathbf{x}_1) & \phi_2(\mathbf{x}_2) & ... & \phi_1(\mathbf{x}_N) \\ . & & & . \\ . & & & . \\ . & & & . \\ \phi_N(\mathbf{x}_1) & \phi_N(\mathbf{x}_2) & ... & \phi_N(\mathbf{x}_N) \end{vmatrix} . \tag{2.4.2}$$

The ground-state configuration is determined by occupying the lowest energy levels according to the Pauli exclusion principle.

The next step is to find a set of ϕ_i's through variational principle by minimizing the total energy with respect to the coefficients of a trial wave function. According to the variational principle, the "best" set of these spin orbitals in the slater determinant is the one which minimizes the electronic energy. This method originates from the fact that the expectation value of the Hamiltonian for any trial wave function is always equal or greater than the ground-state energy (variational principle).

In addition, to solve the Schrödinger equation, the electrons are assumed to move independently in an effective potential (V_{eff}) which includes the interaction of each electron with all nuclei and the other electrons. Hence, using the HF wave function, the energy expectation value can be written as

$$\begin{aligned} E_{\text{HF}} &= \left\langle \psi_{\text{HF}} \middle| \hat{H} \middle| \psi_{\text{HF}} \right\rangle = \left\langle \psi_{\text{HF}} \middle| -\frac{\nabla^2}{2} + \hat{V}_{\text{eff}} \middle| \psi_{\text{HF}} \right\rangle \\ &= \sum_{i=1}^{N} \int \phi_i^*(\mathbf{x}) \left[-\frac{1}{2}\nabla_i^2 - \sum_{I=1}^{M} \frac{Z_I}{|\mathbf{r}_i - \mathbf{R}_I|} \right] \phi_i(\mathbf{x}) d\mathbf{x} + \frac{1}{2} \sum_{i=1}^{N} \sum_{j=1}^{N} (J_{ij} - K_{ij}), \end{aligned} \tag{2.4.3}$$

where

$$\begin{aligned} J_{ij} &= \int\int \phi_i^*(\mathbf{x})\phi_i(\mathbf{x}) \frac{1}{|\mathbf{r}_i - \mathbf{r}_j|} \phi_j^*(\mathbf{x}')\phi_j(\mathbf{x}') d\mathbf{x} d\mathbf{x}' \\ K_{ij} &= \int\int \phi_i^*(\mathbf{x})\phi_j(\mathbf{x}) \frac{1}{|\mathbf{r}_i - \mathbf{r}_j|} \phi_j^*(\mathbf{x}')\phi_i(\mathbf{x}') d\mathbf{x} d\mathbf{x}'. \end{aligned} \tag{2.4.4}$$

The J_{ij} are called Coulomb integrals and the K_{ij} are exchange integrals. Therefore, instead of solving the N-electron Schrödinger equation, the N one-electron HF equations should be solved:

$$\hat{F}_i \phi_i(\mathbf{x}) = \varepsilon_i \phi_i(\mathbf{x}), \tag{2.4.5}$$

in which $\hat{F}_i$ is the Fock operator and takes the following form:

$$\hat{F}_i = -\frac{1}{2}\nabla_i^2 - \sum_{I=1}^{M} \frac{Z_I}{|\mathbf{r}_i - \mathbf{R}_I|} + \sum_{j \neq i} (\hat{J}_j - \hat{K}_j). \tag{2.4.6}$$

It should be noted that in HF approach the effect of "exchange" is included although the electron-electron correlations are neglected [87].

2.5 Density Functional Theory

Since in the HF-based methods one needs to calculate the many-body wave function of the system, these methods become computationally demanding for large systems. An alternative approach to obtain the physical properties of the system is using the electronic charge density instead of many-body wave function which can reduce the number of spatial variables for an N-electron system from 3N to only 3. The original idea of using the electron density as a central quantity was first proposed in Thomas-Fermi model.

2.5.1 Thomas-Fermi Model

In 1927, Thomas and Fermi (TF) used a simple model of homogeneous electron gas to describe the kinetic energy based on constant electron density [88,89]. As the electron gas is not uniform in real atoms and molecules, Thomas-Fermi (TF) model fails to express the energy of an atom. Dirac improved TF model by adding an exchange term to the total energy [90]:

$$\begin{aligned} E_{\mathrm{TF}}[\rho(\mathbf{r})] = &\frac{3}{10}(3\pi^2)^{2/3}\int \rho^{5/3}(\mathbf{r})d\mathbf{r} - Z\int \frac{\rho(\mathbf{r})}{\mathbf{r}}d\mathbf{r} \\ &+ \frac{1}{2}\int\int \frac{\rho(\mathbf{r})\rho(\mathbf{r}')}{|\mathbf{r}-\mathbf{r}'|}d\mathbf{r}d\mathbf{r}' - \underbrace{\frac{3}{4}\left(\frac{3}{\pi}\right)^{1/3}\int \rho(\mathbf{r})^{4/3}d\mathbf{r}}_{E_{\mathrm{X}}^{\mathrm{Dirac}}[\rho(\mathbf{r})]}. \end{aligned} \tag{2.5.1}$$

The kinetic energy, electron-nuclei interaction energy, the electron-electron repulsion energy, and finally the exchange energy are sequentially shown in Eq. 2.5.1. All terms are functions of the charge density which is itself a function of $\mathbf{r}$. Therefore, they are called functionals and their arguments are shown in square brackets.

2.5.2 Hohenberg-Kohn Theory

Starting point of Density Functional Theory (DFT) is a paper written by Hohenberg and Kohn in 1964 [91]. They considered a system of charged spinless electrons with a non-degenerate ground state described by a nonrelativistic time-independent Hamiltonian and showed that the ground-state electron density, in principle, contains all the information included in many-electron wave function. So there is no need to find the wave function for the determination of the ground state of a system. According to their first theorem, the ground-state electron density uniquely determines the external potential $\hat{V}_{\text{ext}}$ within a trivial additive constant. By knowing the external potential, the electronic Hamiltonian $\hat{H}$ can be solved. This statement shows the uniqueness of solution, $\rho(\mathbf{r})$. Then, the total energy functional can be written as:

$$E[\rho] = F[\rho] + \int V_{\text{ext}}(\mathbf{r})\rho(\mathbf{r})d\mathbf{r}, \tag{2.5.2}$$

in which $F[\rho]$ is the Hohenberg-Kohn functional and includes the kinetic energy and the electron-electron interaction energy functionals. $F[\rho]$ is a universal functional irrespective of the system, that is, its mathematical form will be the same for a helium molecule, an ionic material, or even a metal.

Their second theorem states that, if and only if the trial density is the true ground-state density, the total energy functional delivers the lowest ground-state energy based on the variational principle.

Therefore, the only task is to find the $\rho(\mathbf{r})$ function which minimizes the energy. But in practice, it is not as simple as it might seem! Finding the correct $F[\rho]$ is practically impossible, and different approximations are needed to be adapted. A first approximation for $F[\rho]$ was introduced by Kohn and Sham in 1965 [92] providing a practical procedure to find the ground-state charge density, $\rho(\mathbf{r})$.

2.5.3 Kohn-Sham Ansatz

The Kohn-Sham (KS) definition for $F[\rho]$ is as follows:

$$F[\rho] = T_{\text{S}}[\rho] + \frac{1}{2}\int\int \frac{\rho(\mathbf{r})\rho(\mathbf{r}')}{|\mathbf{r}-\mathbf{r}'|}d\mathbf{r}d\mathbf{r}' + E_{\text{XC}}[\rho], \tag{2.5.3}$$

while $T_{\text{S}}[\rho]$ is the kinetic energy of a non-interacting electron gas, the second term is the classical Coulomb interaction energy, and last term $E_{\text{XC}}[\rho]$ is the exchange and correlation energy.

The last two terms include all many-body quantum effects. According to KS approach, one can *map* the many-body system of interacting electrons onto a system with noninteracting particles with the same ground-state density $\rho(\mathbf{r})$.

First, we consider a system of noninteracting particles moving in an effective potential, V_{eff} (like a homogeneous electron gas). The energy functional for this system is

$$E[\rho] = T_{\text{S}}[\rho] + \int V_{\text{eff}}(\mathbf{r})\rho(\mathbf{r})d\mathbf{r}. \tag{2.5.4}$$

Employing the variational principle

$$\delta E[\rho] = 0, \tag{2.5.5}$$

the energy is minimized with respect to small variations of the electron density under the constraint of $\int \rho(\mathbf{r})d(\mathbf{r}) = N$. Then, using the method of Lagrange multiplier, we can write:

$$\mu = \frac{\delta E[\rho]}{\delta\rho(\mathbf{r})} = \frac{\delta T_{\text{S}}[\rho]}{\delta\rho(\mathbf{r})} + V_{\text{eff}}. \tag{2.5.6}$$

μ is Lagrange multiplier and is defined as the derivative of the energy with respect to the density. Moreover, for a many-body system, μ has the following form for energy obtained by substituting Eq. 2.5.3 into Eq. 2.5.2:

$$\mu = \frac{\delta E[\rho]}{\delta\rho(\mathbf{r})} = \frac{\delta T_{\text{S}}[\rho]}{\delta\rho(\mathbf{r})} + \int \frac{\rho(\mathbf{r}')}{|\mathbf{r}-\mathbf{r}'|}d\mathbf{r}' + \frac{\delta E_{\text{XC}}[\rho]}{\delta\rho(\mathbf{r})} + V_{\text{ext}}. \tag{2.5.7}$$

Comparing Eqs. 2.5.6 and 2.5.7, V_{eff} is obtained as:

$$V_{\text{eff}} = \int \frac{\rho(\mathbf{r}')}{|\mathbf{r}-\mathbf{r}'|}d\mathbf{r}' + V_{\text{ext}} + \underbrace{\frac{\delta E_{\text{XC}}[\rho]}{\delta\rho(\mathbf{r})}}_{V_{\text{XC}}}, \tag{2.5.8}$$

where the last term is the exchange-correlation (XC) potential.

We should keep in mind that all the functionals can include the spin degree of freedom by defining two charge densities, one for spin up and the other for spin down electrons. The many-particle problem can be reduced to a single-particle formulation. Therefore, set of one-electron

Schrödinger-like equations with corresponding Hamiltonian $\hat{H}_{\text{eff}}$ can be written as:

$$\hat{H}_{\text{eff}}(\mathbf{r})\phi_i(\mathbf{r}) = \left[-\frac{1}{2}\nabla^2 + \hat{V}_{\text{eff}}(\mathbf{r})\right]\phi_i(\mathbf{r}) = \varepsilon_i\phi_i(\mathbf{r}), \tag{2.5.9}$$

where each ϕ_i is a single-particle orbital. The Eqs. 2.5.9 are called Kohn-Sham (KS) equations. The Eqs. 2.5.9 imply that each electron is moving in a mean-field effective potential of its surrounding. The KS equations are solved iteratively as follows: After an initial guess for the electron density, the effective potential V_{eff} is calculated, and by solving KS equations, the orbitals (KS eigenfunctions) are found. With the newly obtained orbitals, a new electron density is generated. If the new electron density is not equal to the previous one within a given threshold, a new cycle of calculation starts, using the recently-calculated electron density as a new input. This cycle is called a self-consistent cycle.

In Eq. 2.5.8, all unknown parts are gathered in the exchange-correlation functional E_{XC}. This term have to be chosen in a way that it accurately describes all many-body effects. The main challenge in DFT is to find a good approximation for this term.

2.5.4 Approximations to the Exchange-Correlation Functional

As mentioned, a good approximation to $E_{\text{XC}}[\rho]$ is crucial in order to get an accurate result in a DFT calculation. One should note that as soon as adapting any approximation, the variational principle is no longer valid. Therefore, there is no guarantee that minimization of the approximate energy functional gives the upper bound to the true exact ground-state energy. Nevertheless, the variational principle is still applied, and the obtained electron density is considered as an approximation for the true ground-state density.

It is appropriate to use the concept of the exchange-correlation hole $\rho_{\text{XC}}(\mathbf{r}, \mathbf{r}')$ (Fermi-Coloumb hole) in order to estimate the exchange-correlation energy E_{XC}. The origin of the XC hole is that each electron, whose motion is correlated to that of the other electrons, creates an empty hole around itself based on Pauli exchange principle, since based on this principle, the probability of finding two electrons with the same quantum numbers at the same point in space is zero. According to sum rule:

$$\forall \mathbf{r} \quad : \qquad \int \rho_{\mathrm{XC}}(\mathbf{r}, \mathbf{r}')d\mathbf{r}' = -1. \tag{2.5.10}$$

The exchange part of the XC hole is called the Fermi hole, while the correlation part results in the Coulomb hole. The Fermi hole integrates to -1, therefore, it is negative everywhere. As a result, the integral of the Coulomb hole should be 0. Therefore, the XC hole density has a negative sign, and the interaction of electron with this hole, which is attractive, can define the XC energy in the KS equation:

$$E_{\mathrm{XC}}[\rho] = \frac{1}{2}\int\int \rho(\mathbf{r})\frac{1}{|\mathbf{r}-\mathbf{r}'|}\rho_{\mathrm{XC}}(\mathbf{r}, \mathbf{r}')d\mathbf{r}d\mathbf{r}'. \tag{2.5.11}$$

Here some of the famous XC functionals are listed:

Local Density Approximation

The first approximation to explicitly find a expression for the E_{XC} is based on a homogenous electron gas. That is, the real inhomogeneous electron gas is assumed to consist of small cells while in each of them the electron density is constant. This assumption is called local density approximation (LDA), and the XC functional is given by:

$$E_{\mathrm{XC}}^{\mathrm{LDA}}[\rho(\mathbf{r})] = \int \rho(\mathbf{r})\varepsilon_{\mathrm{XC}}(\rho)d\mathbf{r}, \tag{2.5.12}$$

where $\varepsilon_{\mathrm{XC}}(\rho)$ is the exchange-correlation energy per electron of mentioned homogeneous gas and it can be split into exchange and correlation contributions,

$$\varepsilon_{\mathrm{XC}}(\rho) = \varepsilon_{\mathrm{X}}(\rho) + \varepsilon_{\mathrm{C}}(\rho). \tag{2.5.13}$$

The exchange part is obtained through Dirac exchange term $E_{\mathrm{X}}^{\mathrm{Dirac}}$ in Eq.2.5.1,

$$\varepsilon_{\mathrm{X}}(\rho) = -\frac{3}{4}\left(\frac{3\rho(\mathbf{r})}{\pi}\right)^{1/3}. \tag{2.5.14}$$

There is no explicit expression for the correlation part, while it has been determined by highly accurate quantum Monte Carlo (MC) simulations of the uniform electron gas [93].

LDA usually underestimates bond lengths and lattice constants, and overestimates the binding energies specially for the systems with nonuniform electron densities. However, LDA surprisingly shows a good performance in a wide range of problems. This arises from the fact that LDA satisfies the sum rule of negative values for the Fermi hole.

Generalized Gradient Approximation

Employing higher orders of density gradient in the XC functional can improve its approximation. In generalized gradient approximation (GGA), the first derivative of the density as well as the density itself are included in the XC functional:

$$E_{\mathrm{XC}}^{\mathrm{GGA}}[\rho(\mathbf{r})] = \int \rho(\mathbf{r}) f(\rho, |\nabla\rho|) d\mathbf{r}, \tag{2.5.15}$$

where $f(\rho, |\nabla\rho|)$ is found in such a way that the resulting functional is consistent with different criteria and sum rules. In general, GGA can deliver more reliable results compared to LDA, specially in systems with inhomogeneous electronic charge distribution. Different GGA functionals have been proposed like PW91 [94] and its close relatives PBE [95], RPBE [96], MPBE [97]. Employing the PBE functional, which has been widely used, the overestimation of binding energies is considerably corrected compared to LDA.

Moreover, if we enter second-order density gradient into the expression of the XC functional, as in meta-GGA functionals such as that of Tao, Perdew, Staroverov and Scuseria (TPSS) [98], better results compared to those of LDA and GGA functionals can be achieved. However, meta-GGA functionals are much more computationally demanding compared to LDA and GGA ones.

Further Improvements to Density Functional Formalism

In the case of strongly correlated electron systems such as transition metal oxides, lanthanides, actinides, and their compounds, electrons are significantly localized on transition metal atoms.

Therefore, they cannot easily be approximated using a mean-field approach such as the KS formalism. The error partly comes from the unphysical self interaction in the common LDA and GGA functionals. A correction, based on the fact that the self interactions are completely cancelled in the HF approach, is added to the approximate XC functionals. This approach is called the self-interaction correction (SIC) method [99].

DFT+U Method: The other approach is adding the Hubbard U term to the KS Hamiltonian. In 1963 and 1964, Hubbard applied a simple extension of the tight-binding model to describe the magnetism coming from electronic correlations [100–102]. Adding such a potential term in the KS Hamiltonian introduces an orbital-dependent interaction, and causes an energy shift for the localized orbitals due to the on-site Coulomb repulsion.

Hybrid Functionals: Further improvements to the GGA and meta-GGA functionals can be achieved by using hybrid functionals. In this kind of XC functionals, the HF exact exchange is partially added to the LDA and GGA exchanges. One of the most popular hybrid functional is the Heyd-Scuseria-Ernzerhof (HSE) [103, 104] functional which employs a screened-exchange potential. The idea behind the screened functional is that the Coulomb potential in the HF exchange is a long-range potential. Therefore, the calculations on large systems using HF exact exchange are computationally demanding. Furthermore, the interactions between electrons which are far from each other can be screened by polarization effects. Thus, the contribution of the HF exact exchange can be restricted only to the short range while the long-range part of the exchange can be taken from the PBE functional. The HSE hybrid density functional takes the form of:

$$E_{\mathrm{XC}}^{\mathrm{HSE}} = \alpha E_{\mathrm{X}}^{\mathrm{HF,SR}}(\mu) + (1-\alpha) E_{\mathrm{X}}^{\mathrm{PBE,SR}}(\mu) + E_{\mathrm{X}}^{\mathrm{PBE,LR}}(\mu) + E_{\mathrm{C}}^{\mathrm{PBE}}, \tag{2.5.16}$$

where μ and α are the screening and the mixing parameters respectively. $E_{\mathrm{X}}^{\mathrm{PBE,SR}}$ and $E_{\mathrm{X}}^{\mathrm{PBE,LR}}$ are the short-range and long-range contributions from the PBE exchange energy, $E_{\mathrm{X}}^{\mathrm{HF,SR}}$ is the short-range exact-exchange energy, and $E_{\mathrm{C}}^{\mathrm{PBE}}$ is the PBE correlation energy.

In this thesis, the PBE functional is applied in most of the DFT calculations. In the case of transition metals, the PBE+U method is used. Moreover, some of the calculations are carried out using the HSE(06) hybrid functional and compared to the same calculations performed with the PBE+U approach.

Dispersion Corrections: Long-range interactions between instantaneous dipole moments assigned to different fragments of the charge distribution in a system are commonly referred to as dispersion interactions. DFT in its local or semilocal approximations is unable to cerrectly account for such long-range correlations. Therefore, several approaches have been proposed to correct the DFT energies and forces to include dispersion interactions. Here, Grimme's DFT-D2 [105] and DFT-D3 [106] methods are briefly explained.

Grimme and co-workers added an empirical long-range $-C_6R^{-6}$ energy correction to account for dispersion interactions in DFT calculations (DFT-D) [107]. This method was improved over the time to DFT-D2 [105] and DFT-D3 [106]. The general form of the dispersion correction in DFT-D and DFT-D2 can be written as:

$$E_{\mathrm{disp}} = -s_6 \sum_{I=1}^{M-1} \sum_{J=I+1}^{M} \frac{C_6^{IJ}}{R_{IJ}^6} f_{\mathrm{dmp}}(R_{IJ}), \tag{2.5.17}$$

where M is the number of atoms, s_6 is a scaling factor, R_{IJ} is the interatomic distance, and C_6^{IJ} is the dispersion coefficient for the atom pair (IJ). A damping function (f_{dmp}) is introduced to avoid double counting and the singularities at short distances where DFT can already give the correct results. In DFT-D3 framework [106], the two-body interaction is described by also adding R^{-8} and R^{-10} contributions. In addition, many-body dispersion interactions are included in this method up to three-body interaction by the third-order perturbation theory for three atoms.

2.6 DFT Calculations in Solids

The many-body problem is mapped to a single-particle problem using Kohn-Sham ansatz which results in the KS equations 2.5.9. However, finding the electronic structure of the extended crystals with an infinitely large number of electrons using the KS equations is not a straightforward task. One way to reduce the complexity of this problem is to decrease the system size using the symmetry properties.

A crystalline solid consists of periodic arrangements of atoms that repeat endlessly. The repeating blocks, which are usually referred to as unit cells, should be chosen in a way that it can generate the whole crystal system by translational vectors. As such, all points can be defined by a translational vector of Bravais lattice $\mathbf{R}$:

$$\mathbf{R} = u\mathbf{a}_1 + v\mathbf{a}_2 + w\mathbf{a}_3, \tag{2.6.1}$$

where the primitive vectors $\mathbf{a}_1$, $\mathbf{a}_2$ and $\mathbf{a}_3$ are not all on the same plane, and u, v and w are integer values. Thus, the whole crystal can be described completely by focusing on one unit cell and applying periodic boundary conditions (PBC) to the Schrödinger equation. According to the PBC, a single-electron orbital satisfies the following condition [108]:

$$\phi(\mathbf{r} + N_i\mathbf{a}_i) = \phi(\mathbf{r}) \qquad i = 1, 2, 3, \tag{2.6.2}$$

where the $\mathbf{a}_i$ are three primitive vectors and the N_i are the number of unit cells along $\mathbf{a}_i$ in crystal.

Another concept which is important in finding the electronic structure of periodic systems is reciprocal lattice. The reciprocal lattice is defined as the Fourier transform of the Bravais lattice in real space. Considering the plane wave $e^{i\mathbf{k}\cdot\mathbf{r}}$, all wave vectors $\mathbf{K}$ belong to the reciprocal lattice if they meet this requirement:

$$e^{i\mathbf{K}\cdot(\mathbf{r}+\mathbf{R})} = e^{i\mathbf{K}\cdot\mathbf{r}}, \qquad \Longrightarrow \qquad e^{i\mathbf{K}\cdot\mathbf{R}} = 1, \tag{2.6.3}$$

for all $\mathbf{R}$ in the Bravais lattice. Any vector $\mathbf{K}$ can be written as a function of three reciprocal primitive vectors $\mathbf{b}_i$:

$$\mathbf{K} = h\mathbf{b}_1 + k\mathbf{b}_2 + l\mathbf{b}_3, \tag{2.6.4}$$

where integers h, k and l are called Miller indices. A reciprocal lattice vector $h\mathbf{b}_1 + k\mathbf{b}_2 + l\mathbf{b}_3$ is normal to the plane (h, k, l), since $\mathbf{a}_\mathrm{i} \cdot \mathbf{b}_\mathrm{j} = 2\pi\delta_{\mathrm{i,j}}$. The primitive unit cell in the reciprocal lattice is called Brillouin zone.

2.6.1 Bloch's Theorem

Since the ions in a crystal are periodically arranged in space, one can consider the effective potential $V_{\mathrm{eff}}(\mathbf{r})$, defined in Eq. 2.5.9, to have the same lattice periodicity. According to the Bloch's theorem, the single-electron orbital in a periodic structure can be written as a product of a plane wave and a function with the periodicity of the Bravais lattice:

$$\phi_{n\mathbf{k}}(\mathbf{r}) = e^{i\mathbf{k}\cdot\mathbf{r}} u_{n\mathbf{k}}(\mathbf{r}), \tag{2.6.5}$$

where $u_{n\mathbf{k}}(\mathbf{r} + \mathbf{R}) = u_{n\mathbf{k}}(\mathbf{r})$ for all $\mathbf{R}$ in the Bravais lattice. The index n is called the band index which refers to independent KS orbitals for a given $\mathbf{k}$, due to the PBC 2.6.2. It can be shown that the wave functions of the form 2.6.5 have the following properties:

$$\phi_{n\mathbf{k}}(\mathbf{r} + \mathbf{R}) = e^{i\mathbf{k}\cdot\mathbf{R}} \phi_{n\mathbf{k}}(\mathbf{r}), \tag{2.6.6}$$

$$\phi_{n,\mathbf{k}+\mathbf{K}}(\mathbf{r}) = \phi_{n\mathbf{k}}(\mathbf{r}),$$

$$\varepsilon_{n,\mathbf{k}+\mathbf{K}} = \varepsilon_{n\mathbf{k}},$$

where $\varepsilon_{n\mathbf{k}}$ represents the energy of the electron with wave vector $\mathbf{k}$ in band n. The last two equations show that the crystal orbitals and the energies of two states defering by a reciprocal lattice vector $\mathbf{K}$ are identical. This allows us to confine our electronic structure calculations to the first Brillouin zone. For many physical properties such as electronic charge density and density of states, it is necessary to have a proper $\mathbf{k}$-point sampling in the first Brillouin zone. In the electronic structure calculations, the $\mathbf{k}$-point sampling is done using different approaches. The most commonly used method is the Monkhorst-Pack scheme [109] which employs an unbiased method to choose a set of $\mathbf{k}$ points for efficient sampling of the Brillouin zone.

2.7 Basis Sets

All the studies on the electronic structure of systems are based on expansion of an unknown orbital in terms of a known basis set. Two types of basis functions, which are usually used to represent the unknown wave functions, are plane waves and atomic orbitals.

2.7.1 Plane-Wave Basis Sets

Plane waves (PWs) form a complete set of functions which do not depend on atomic positions. The periodic part of the Bloch function can be expanded in terms of plane waves as:

$$u_{n\mathbf{k}}(\mathbf{r}) = \frac{1}{\sqrt{\Omega}} \sum_{\mathbf{K}} c_{n\mathbf{k},\mathbf{K}} e^{i\mathbf{K}\cdot\mathbf{r}}, \tag{2.7.1}$$

in which Ω is the volume of the real space unit cell, $\mathbf{K}$ is a reciprocal lattice vector, and $c_{n\mathbf{k}}$ is the independent coefficient. Therefore, the Bloch functions can be written as:

$$\phi_{n\mathbf{k}}(\mathbf{r}) = \frac{1}{\sqrt{\Omega}} \sum_{\mathbf{K}} c_{n\mathbf{k},\mathbf{K}} e^{i(\mathbf{k}+\mathbf{K})\cdot\mathbf{r}}. \tag{2.7.2}$$

In order to correctly describe the electronic wave function of the system, lots of PWs are needed which expand over the whole system. This makes the Hamiltonian matrix very large. Therefore, only the PWs with kinetic energy lower than a predefined cutoff (E_{cutoff}) are included in the basis set,

$$\frac{1}{2}|\mathbf{k}+\mathbf{K}|^2 < E_{\text{cutoff}}. \tag{2.7.3}$$

In addition, the PW codes usually use pseudopotentials to approximate the effect of the core electrons together with the nuclei by an effective potential which acts on the valence electrons [110–112]. Pseudopotential approximation will be discussed later in this chapter.

2.7.2 Atomic-Orbital Basis Sets

A promising alternative for the PW basis sets are localized atomic orbitals. In most of the DFT codes employing localized basis sets, electronic orbital $\phi_i(\mathbf{r})$ in a unit cell is constructed as a linear combination of normalized atomic orbitals (LCAO),

$$\phi_i(\mathbf{r}) = \sum_{\alpha=1}^{M} c_{\alpha i} \chi_\alpha^M(\mathbf{r}), \tag{2.7.4}$$

in which χ_α^M is the atomic orbital centered at nucleus M in the unit cell. For non-periodic calculations, one can use Eq. 2.7.4 in order to construct the KS Hamiltonian. However, for periodic calculations, the fact that the atomic orbitals, χ_α^M, are essentially of the Bloch form should be taken into account. Therefore, according to Eqs. 2.6.6, each atomic orbital can be written as [113, 114]:

$$\chi_\alpha^M(\mathbf{r}) = \frac{1}{\sqrt{N}} \sum_{\mathbf{R}}^{N} e^{i\mathbf{k}\cdot\mathbf{R}} \chi^M(\mathbf{r} - \mathbf{R}), \tag{2.7.5}$$

where N is the total number of unit cells in the whole crystal according to the PBC Eq. 2.6.2, and $\mathbf{R}$ is the real-space lattice vector. Due to the finite range of atomic orbitals, the KS Hamiltonian becomes sparse. The Hamiltonian matrix elements involving two atomic basis functions which are far away from each other can be immediately set to zero as soon as their distance is longer than the sum of their individual spatial range. This is a direct consequence of the "near-sightedness" of the electronic systems [115]. Another advantage of using the atomic orbitals as basis functions is the ability of performing the all-electron calculations.

The Gaussian Basis Functions

One of the most popular forms for atomic-orbital basis sets are Gaussian functions. The Gaussian-type orbitals have the following form in spherical coordinates [116, 117]:

$$\chi_{\zeta,n,l,m}(r, \theta, \varphi) = A Y_{l,m}(\theta, \varphi) r^{2n-2-l} e^{-\zeta r^2}, \tag{2.7.6}$$

where n, l, and m are the quantum numbers, ζ exponent is a constant related to the effective charge of the nucleus, A is a normalization factor, and $Y_{l,m}$ are the spherical harmonic functions. The function in Eq. 2.7.6 is generally referred to as the primitive Gaussian function. It is common to use a contracted Gaussian function which includes fixed linear combinations of primitive functions [114]. In a contracted basis set, there is a limited number of variational parameters. Thus, using this kind of basis functions considerably reduces the computational cost.

However, it is always a formidable task to guess how many basis functions should be employed for the system of interest. For instance, the smallest number of functions in the case of a hydrogen atom is a single s-function. For lithium, two s-functions are required, but it is better to also consider a set of p-functions. To improve the employed basis set, the number of basis functions is doubled. Such basis set is called double zeta (DZ). For example, two s-functions with different ζ exponents are used for hydrogen. Similarly, triple zeta (TZ) and quadruple zeta (QZ) basis functions contain respectively three and four basis functions for each element in the system. The next improvement is using the polarization functions. Chemically bonded atoms usually possess some distortions in their electron density compared to their isolated shapes. In order to describe the charge polarization effects, higher angular momentum functions are added to the basis set, for example p-functions for hydrogen atom, and d-functions for first-row elements.

Nevertheless, employing atomic-orbital basis functions is not always problem-free. For example, using localilzed basis functions can cause an error in calculating the interaction energies of different fragments of the system, which is known as basis set super position error (BSSE) [118]. Assuming A and B are two fragments interacting with each other, the interaction energy of the total system AB at its optimized geometry is usually calculated as the energy difference between the total system AB, and the isolated fragments A and B:

$$\Delta E_{\text{int}} = E_{\text{ab}}(\text{AB}) - E_{\text{a}}(\text{A}) - E_{\text{b}}(\text{B}), \tag{2.7.7}$$

where $E_{\text{ab}}(\text{AB})$, $E_{\text{a}}(\text{A})$, and $E_{\text{b}}(\text{B})$ are the energies of the total system AB, the isolated fragment A, and the isolated fragment B, respectively. The subscripts a and b respectively indicate the basis functions of fragment A and B. Therefore, $E_{\text{a}}(\text{A})$ refers to the total energy of the fragment A calculated using only the basis functions of A. However, in the total system AB, basis functions of the fragment A can be "borrowed" by the fragment B and vice versa. Thus, as is clear in Eq. 2.7.7, the three Hamiltonians which have been used to estimate the three total energies do not have the same dimension. This indicates an underlying error due to incompleteness of the basis sets. A method that is widely applied to correct the BSSE is the Counterpoise correction scheme of Boys and Bernardi [119]. In the Counterpoise method, the total energy of the fragment A (B) is calculated in the presence of all the basis functions of the fragment B (A) on the atomic centers of B (A) without considering the electrons and the nuclear charges of B (A). These basis functions, located at the A or B fragments without electrons and nuclear charges, are referred to as "ghost functions". Therefore the interaction energy is computed as:

$$\Delta E_{\text{int}} = E_{\text{ab}}(\text{AB}) - E_{\text{ab}}(\text{A}) - E_{\text{ab}}(\text{B}), \tag{2.7.8}$$

In this dissertation, localized basis sets represented by contracted Gaussian functions are applied using the SeqQuest code [120, 121]. We use DZ basis set together with the polarization function. The BSSE is corrected using the Counterpoise method in all the interaction energy calculations. Furthermore, the PW basis sets are employed in the calculations using the Vienna Ab initio simulation package (VASP) [122–125]. In addition, we use the CP2K Quickstep code [126–129] to simulate the large systems with more than 300 atoms employing mixed Gaussian and PW basis sets.

2.8 Pseudopotential Approximation

Most of the electronic properties in solids are determined by the valence electrons. Moreover, representing the orbitals of core electrons requires lots of basis functions that increases the computational cost. Thus, to reduce the size of the basis set without compromising accuracy, the strong ionic core potential is replaced by an effective weak pseudopotential, and smoothly varying pseudo-orbitals are used instead of valence electron orbitals within the core region [130–132]. However, outside the core region, the pseudopotentionl and pseudo-orbitals are required to be the same as the corresponding all-electron ones.

One important class of pseudopotentials is norm-conserving pseudopotentials [133, 134]. In this scheme, the all-electron orbitals and pseudo-orbitals must have the same norm. Therefore, the pseudo charge and the pseudo electron density are identical to true charge and true electron density in the core region. Various types of norm-conserving pseudopotentials are introduced by different researchers such as Bachelet-Hamann-Schlüter [135], Troullier and Martins [136], and Goedecker-Teter-Hutter [137].

2.9 *First-Principles* Thermodynamics

DFT is a technique that gives a detailed insight on the electronic structure of materials. However, to explain the phenomena in the large time and length scales, an appropriate connection between the microscopic, the mesoscopic, and the macroscopic regimes is needed. Thermodynamics and statistical mechanics can establish such a link by combining the macroscopic concepts with the microscopic aspects provided by DFT calculations. Thus, this approach is often referred to as *first-principles* thermodynamics.

Typically, we only have access to zero-temperature and zero-pressure results from DFT calculations. The Gibbs free energy enables us to relate these results to finite temperatures and pressures. For a closed system with volume V, at temperature T and pressure p, the Gibbs free energy G is given by

$$G = E_{\text{tot}} + F_{\text{vib}} - TS_{\text{conf}} + pV, \tag{2.9.1}$$

where E_{tot} is the total electronic energy directly obtained from the DFT calculations. S_{conf} is the configurational entropy, and F_{vib} is the vibrational free energy. Configurational entropy consists of translational and rotational contributions [138]. The translational entropy is expressed in terms of the thermal wavelength and it is usually calculated using the Sackur-Tetrode equation in ideal gas approximation [139, 140]:

$$S_{\text{t}} = k_{\text{B}}N\left[\frac{5}{2} + \ln\left(\frac{v}{N\Lambda^3}\right)\right], \tag{2.9.2}$$

where k_{B} is the Boltzmann constant, and v is the volume per mole of the molecule. The thermal wavelength is defined as $\Lambda = h/(\sqrt{2\pi m k_{\text{B}}T})$, in which h is Planck's constant and m is the molar mass of the molecule. Moreover, the rotational entropy is expressed using the inertia momenta (I_1, I_2, I_3) [140, 141]:

$$S_{\text{r}} = k_{\text{B}}N\left[\frac{3}{2} + \ln\left(\frac{\sqrt{\pi}}{\sigma}\left(\frac{2k_{\text{B}}T}{\hbar^2}\right)^{3/2}\right)\sqrt{I_1 I_2 I_3}\right], \tag{2.9.3}$$

in which σ is the symmetry number and it is equal to 1 for most molecules, except for those with rotational symmetry.

The vibrational free energy is calculated based on the vibrational entropy S_{vib}:

$$F_{\text{vib}} = -TS_{\text{vib}} = -k_{\text{B}}T\ln\left[\frac{e^{-\frac{\varepsilon}{k_{\text{B}}T}}}{\sum_n e^{-\frac{\varepsilon_n}{k_{\text{B}}T}}}\right]. \tag{2.9.4}$$

Within the harmonic approximation ($\varepsilon_n = (n + \frac{1}{2})\hbar\omega$), the partition function Z takes the following form,

$$Z = \sum_{n=0}^{\infty} e^{-\frac{\varepsilon_n}{k_{\text{B}}T}} = e^{-\frac{\hbar\omega}{2k_{\text{B}}T}} \sum_n \left(e^{-\frac{\hbar\omega}{k_{\text{B}}T}}\right)^n = \frac{e^{-\frac{\hbar\omega}{2k_{\text{B}}T}}}{1 - e^{-\frac{\hbar\omega}{k_{\text{B}}T}}}. \tag{2.9.5}$$

Therefore, the vibrational contribution depends on temperature T and frequency ω

$$F_{\text{vib}}(T, \omega) = \frac{1}{2}\hbar\omega + k_{\text{B}}T\ln\left[1 - e^{-\frac{\hbar\omega}{k_{\text{B}}T}}\right]. \tag{2.9.6}$$

At $T = 0$, only the first term in Eq. 2.9.6 remains which gives the zero-point energy of the vibrational mode ω.

2.9.1 Surface Energy

On a surface, there is no periodicity along the normal direction. Thus, different models are presented to choose the smallest unit cell that can periodically reproduce the whole system. One of these simulation models is the supercell approach in which the crystal slabs are separated by a vacuum layer in the direction perpendicular to the surface [142]. In order to have a proper description for the surfaces, the vacuum gap between two slabs has to be large enough to completely decouple the slabs. Also to model a semi-infinite crystal, the slab thickness has to be sufficiently large. Therefore, to find the appropriate width of the vacuum gap and the slab thickness, convergence tests are required. Moreover, in the slab calculations, it is convenient to set the lattice parameters based on the theoretically optimized bulk structure. Thus, the surface periodic unit is written based on the strain-free bulk unit cell.

In studying surfaces, it is important to know how much energy is required to cut a bulk sample, and create a unit surface area. Creating surfaces by cleaving a solid is not an spontaneous process, since during this process the Gibbs free energy increases [143]. As a result, the most stable surface at a certain T and p is the one that has the lowest surface energy. The surface free energy for a slab with two equivalent surfaces in the supercell model can be written as

$$\gamma = \frac{1}{2A}\left[G_{\mathrm{slab}} - nG_{\mathrm{bulk}}\right], \tag{2.9.7}$$

where A and G_{slab} are the surface area and the Gibbs free energy of the slab, while G_{bulk} and n are the Gibbs free energy per unit cell of the bulk and the numbers of the bulk units in the slab, respectively. In solids, the difference between the configurational and vibrational contributions in the surface and those ones in the bulk is usually very small. The pV term is also negligible for solids at pressures up to 1 atm [144]. Therefore, in Eq. 2.9.7, instead of evaluating the

Gibbs free energies, the total DFT energy values are calculated, and the surface free energy is expressed as

$$\gamma = \frac{1}{2A}\left[E_{\mathrm{slab}} - nE_{\mathrm{bulk}}\right], \tag{2.9.8}$$

in which E_{slab} and E_{bulk} are the total electronic energies of the slab and the bulk unit cell, respectively. In order to have an accurate estimation for the surface free energy, all energies in Eq. 2.9.8 have to be calculated at the same level of theory, that is using the same basis sets and k-point sampling.

2.10 Molecular Dynamics Simulations

It is generally important to study a system under realistic conditions, that is finite temperatures and/or pressure. For this purpose, a class of simulations can be employed in which the evolution of a system can be tracked in time. These classes of simulations are usually referred to as molecular dynamics (MD) simulations [145, 146]. MD simulations allow for prediction of the time evolution of different systems consisting of interacting particles by numerically solving the classical equations of motions. With the most general form for the potential energy function of the system, $U(\mathbf{R}_1, \mathbf{R}_2, ..., \mathbf{R}_N)$, structural evolution of the system can be obtained by calculating the forces acting on atoms through

$$\mathbf{F}_I = -\nabla_I U(\mathbf{R}_1, \mathbf{R}_2, ..., \mathbf{R}_N), \tag{2.10.1}$$

where $\mathbf{R}_I$ denotes the instantaneous position of atom I. By knowing the atomic positions and forces at time t, one can, in principle, predict them at later times via integrating the equation of motion. Generally, there are two main families of MD simulations which differ in the way they estimate the potential energy function, U. In classical MD simulations, U is obtained using parametric interatomic potentials, whereas in *ab initio* MD simulations it is computed through employing an electronic structure method, such as DFT. In *ab initio* MD simulations, the forces $\mathbf{F}_I$ are calculated “on-the-fly” using an electronic structure method [147].

2.10.1 Integrating the Equations of Motion

Irrespective of the approach used to describe the potential energy function, one needs to numerically integrate the equation of motion for the atoms which are usually treated as classical particle.

The Verlet Algorithm

The widely used Verlet algorithm [148] uses the positions and the forces at time t together with the atomic positions at $t-\Delta t$ in order to predict the positions at time $t+\Delta t$. A Taylor expansion of the position of the particle I at time $t+\Delta t$ gives

$$\mathbf{R}_I(t+\Delta t) \approx \mathbf{R}_I(t) + (\Delta t)\mathbf{V}_I(t) + \frac{(\Delta t)^2}{2M_I}\mathbf{F}_I(t), \tag{2.10.2}$$

where $\mathbf{V}_I$ and M_I are the velocity and the mass of the particle I, respectively. By performing a similar Taylor expansion for the particle I at time $t-\Delta t$, and adding these two equations together, the following expression for the position is obtained

$$\mathbf{R}_I(t+\Delta t) \approx 2\mathbf{R}_I(t) - \mathbf{R}_I(t-\Delta t) + \frac{(\Delta t)^2}{M_I}\mathbf{F}_I(t). \tag{2.10.3}$$

Equation 2.10.3 is known as the Verlet integrator [148], which can be used to propagate the trajectory of a particle by time step Δt. Although in the Verlet algorithm the velocities are not used to find the positions in the next time steps, but one can easily compute them via

$$\mathbf{V}_I(t) = \frac{\mathbf{R}_I(t+\Delta t) - \mathbf{R}_I(t-\Delta t)}{2(\Delta t)}. \tag{2.10.4}$$

The Velocity Verlet Algorithm

The Verlet algorithm has the disadvantage of not propagating the complete phase space trajectory, that is the positions as well as the velocities. Another drawback of the algorithm is that the positions need to be stored in memory at both times t and $t-\Delta t$. In order to overcome these shortcomings, one use the time-reversibility of the Newton's equations of motion. It means that one will get to the same observed points in the phase space if the trajectory is propagated backwards in time. Thus, if the starting time in Eq. 2.10.2 is $t + \Delta t$ and the time step of the motion is $-\Delta t$, it will be obtained

$$\mathbf{R}_I(t) \approx \mathbf{R}_I(t + \Delta t) + (-\Delta t)\mathbf{V}_I(t + \Delta t) + \frac{(\Delta t)^2}{2M_I}\mathbf{F}_I(t + \Delta t). \tag{2.10.5}$$

By substituting $\mathbf{R}_I(t + \Delta t)$ from Eq. 2.10.2 to the above equation, one can find

$$\mathbf{V}_I(t + \Delta t) \approx \mathbf{V}_I(t) + \frac{\Delta t}{2M_I}\left[\mathbf{F}_I(t) + \mathbf{F}_I(t + \Delta t)\right]. \tag{2.10.6}$$

Equations 2.10.2 and 2.10.6 are known as the velocity Verlet algorithm [149] and they propagate the positions and the velocities simultaneously. Time-reversal symmetry is a fundamental property of classical equations of motion and it should be preserved in order to achieve the numerical stability. It is indeed preserved by both the Verlet and velocity Verlet algorithms.

2.10.2 MD Simulations in Canonical Ensemble

According to the ergodic hypothesis, an ensemble average of an observable can be obtained by calculating the time average of the observable over a long period of time [146]. Starting with a fixed number of particles, N, in a fixed volume, V, one can study the evolution of the system at constant energy, E, in the phase space using the algorithms mentioned in previous section. This corresponds to micro-canonical (NVE) ensemble. However, to study a system under more realistic conditions, it is necessary to investigate its evolutions in canonical (NVT) ensemble. This can be achieved by coupling the system to a heat bath using a thermostat which keeps the temperature constant.

Nosé-Hoover Thermostat

One of the widely used thermostats was first introduced by Nosé [150, 151] and later modified by Hoover [152] which adapts an extended-ensemble approach. The Hamiltonian of a system of N particles with an extra degree of freedom, s, and its conjugate momentum, P_s, is written as [146]

$$\hat{H}_{\mathrm{Nose}} = \sum_{I=1}^{N} \frac{\hat{\mathbf{P}}_I^2}{2M_I^2} + \hat{U}(\mathbf{R}_1, \mathbf{R}_2, ..., \mathbf{R}_N) + \frac{P_s^2}{2Q} + gk_{\mathrm{B}}T \ln s, \tag{2.10.7}$$

where k_{B} and T are the Boltzmann constant and target temperature, respectively, and g is equal to $3N + 1$. In the course of the MD simulation, the additional degree of freedom, s, scales the velocities to push the instantaneous kinetic energy towards the target value. Q is a parameter with the unit of energy × time^2, and determines the time scale on which the thermostat interacts with the system. It can be viewed as an "effective mass" for s. In the extended system described by Eq. 2.10.7, the total energy is conserved, that is we have micro-canonical ensemble. However, the "potential" for s, that is $gk_{\mathrm{B}}T \ln s$ is chosen in such a way that the micro-canonical distribution of H_{Nose} gives the canonical distribution of the real physical system [146]. It can be shown that in this formulation, the equation for momentum had a friction term which is proportional to the conjugate momentum of the extra degree of freedom, P_s. Moreover, the evolution of P_s is given by the difference between the instantaneous kinetic energy and its canonical average, $gk_{\mathrm{B}}T$. Therefore, the friction term controls the fluctuations of the kinetic energy and hence acts as a "thermostat".

2.10.3 *Ab initio* Molecular Dynamics

Reliability of empirical potentials (force fields) as well as their transferability to different systems are questionable [147, 153, 154]. This is due to the fact that the electronic structure of the system is completely neglected in force-field-based simulations, where the potential energy function U in Eq. 2.10.1 is approximated by parametric interatomic potentials. In contrast to the classical MD simulations, in *ab initio* molecular dynamics simulations (AIMD) the forces are obtained using the expectation value of the total energy in the electronic ground state via

$$\mathbf{F}_I = -\nabla_I \left\langle \psi_0 \middle| \hat{H} \middle| \psi_0 \right\rangle, \tag{2.10.8}$$

where $\hat{H}$ is the total Hamiltonian of the system while ψ_0 denotes the electronic ground-state wave function with energy $E_0(\{\mathbf{R}_I\})$, that is $\hat{H}\,|\psi_0\rangle = E_0\,|\psi_0\rangle$. $\mathbf{R}_I$'s are the atomic positions. At each AIMD step, new electronic ground state, characterized by the atomic positions, is solved and the forces are obtained using Eq. 2.10.8. The electronic charge distribution attributed to this ground state acts as an external field for the nuclei. Afterwards, the nuclei, which are usually treated classically, are propagated in time with the algorithms introduced above. This is exactly the BO approximation which treats the electrons and the nuclei separately [82,147], and the approach for AIMD simulation is often called Born-Oppenheimer MD. Calculation of the derivatives in Eq. 2.10.8 is usually performed using the Hellmann-Feynman theorem [155,156],

$$\begin{aligned}-\nabla_I \left\langle \psi_0 \middle| \hat{H} \middle| \psi_0 \right\rangle &= -E_0 \left\langle \nabla_I \psi_0 | \psi_0 \right\rangle - \left\langle \psi_0 | \nabla_I \psi_0 \right\rangle E_0 - \left\langle \psi_0 \middle| \nabla_I \hat{H} \middle| \psi_0 \right\rangle \\ &= -E_0 \nabla_I \left\langle \psi_0 | \psi_0 \right\rangle - \left\langle \psi_0 \middle| \nabla_I \hat{H} \middle| \psi_0 \right\rangle \qquad (2.10.9)\end{aligned}$$

Considering the orthonormality condition ($\langle \psi_0 | \psi_0 \rangle = 1$),

$$\mathbf{F}_I = -\left\langle \psi_0 \middle| \nabla_I \hat{H} \middle| \psi_0 \right\rangle \qquad (2.10.10)$$

Additionally, the basis functions which expand the ground-state wave function need to be independent of the atomic positions. This condition is satisfied when a PW basis set is used. However, in the case of atomic-orbital basis functions, Eq. 2.10.10 is not valid anymore and extra terms appear on the right-hand side. These additional term are generally referred to as Pulay forces. Nevertheless, the Pulay forces vanish if the basis set is complete [157].

Part of this thesis is dedicated to the investigation of Li diffusion in defective bulk structure of Li_2S using AIMD simulations. These calculations are performed in the canonical (NVT) ensemble while the temperature of the system is controlled by the Nosé-Hoover thermostat. The details are described in chapter 4.

Chapter 3

ADSORPTION OF LI-POLYSULFIDES (Li_2S_x) ON PRISTINE AND DEFECTIVE GRAPHENE [1]

3.1 Introduction

As discussed in the section 1.2.1, in the Li-S batteries, several electrochemical reactions happen during the charge and discharge process [159]. In general, the discharge reactions can be explained by $S_8 \rightarrow$ Li-polysulfides $\rightarrow Li_2S$, in which the intermediate Li-polysulfides are Li_2S_8, Li_2S_6, Li_2S_4, and Li_2S_2. An important problem in this kind of batteries is that electrolyte-soluble Li-polysulfides diffuse to the Li anode (shuttle effect). They reduce at the anode, corrode the Li metal and form the Li_2S_2 and Li_2S. As a consequence, the Li ion diffusion is inhibited, and the reduction of active S material becomes limited, which finally causes the capacity fade. In order to hinder the shuttle effect, it is recommended to use an electrically conductive cathode which can also trap the Li-polysulfides. Therefore, carbon and sulfur composites are good candidates for such a cathode. Although many DFT studies have been carried out on cathode materials in Li-ion batteries (LIBs), less attention has been paid to sulfur cathode materials in the Li-S batteries. In one of the few theoretical works on cathode materials, Wang *et al.* [18] have calculated the atomic structures of Li_2S_4, Li_2S_6, and Li_2S_8 using B3LYP exchange-correlation functional [160–162] and 6-311G basis set, and they have investigated the mechanisms of reactions at sulfur cathode during the discharging.

---

[1] This chapter is based on the results presented in Ref. [158]

In addition, graphene can be introduced in the sulfur cathodes to increase their electrical conductivity. The Li-S batteries with cathodes such as graphene-S composites [163, 164], porous carbon-S composites [165–167], and graphene oxide-S composites [168, 169] have been reported to have high energy capacities. In this chapter, considering graphene in the cathode, the most favorable atomic structures and adsorption energies of Li-polysulfides on pristine and defective graphene are studied using dispersion-corrected DFT calculations. Furthermore, the ability of the graphene with a single vacancy to trap the $\mathrm{Li_2S}_x$ is investigated, and it is discussed whether the defective graphene can avoid the shuttle effect in Li-S batteries.

3.2 Graphene Structure

A two-dimensional sheet of graphene has a hexagonal structure. In this structure, each C atom forms 3 covalent bonds with its nearest neighbors (honeycomb lattice). The fourth valence electron does not participate in the covalent bonding, and the corresponding $2p_z$ orbital is oriented perpendicular to the graphene sheet. The primitive unit cell of graphene contains two carbon atoms. One possible choice of unit cell vectors is shown in Fig. 3.1.a. A and B are carbon atoms, and the primitive vectors $\mathbf{a}_1$ and $\mathbf{a}_2$ are written as:

$$\begin{aligned} \mathbf{a}_1 &= \frac{AB}{2}\left(3, \sqrt{3}\right), \\ \mathbf{a}_2 &= \frac{AB}{2}\left(3, -\sqrt{3}\right), \end{aligned} \tag{3.2.1}$$

where AB is the distance between the nearest neighbor carbons.

Defects can change the electronic and chemical properties of graphene. Therefore, here we study the effect of the common graphene defects in trapping the Li-polysulfides. One of the topological defects in carbon-based structures with honeycomb lattice is Stone-Wales (SW) defect. It is formed by a 90 degree rotation of a carbon-carbon bond in the graphene plane with respect to the midpoint of the bond, forming two pentagons-heptagons out of four hexagones (SW 55-77) as in Fig. 3.1.c. Stone-Wales-like defects are formed by rotation of more than one

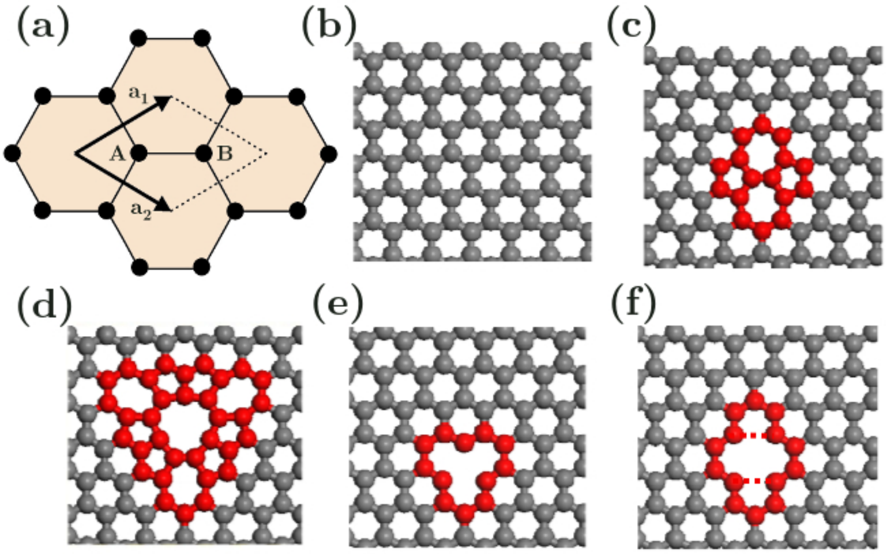

Figure 3.1: (a) Schematic view of the graphene primitive unit cell. Top views of (b) pristine, (c) SW 55-77, (d) SW-like 555555-777-9, (e) monovacant graphene, and (f) divacant graphene structures.

pair of carbons, leading to more pentagons, heptagons, and other n-gons. None of the atoms in such defects has dangling bonds (see Fig. 3.1.d). Point defects are also created in graphene during some processes such as synthesis or irradiation. Monovacancy, formed through removal of a carbon atom from the graphene sheet, initially creates three dangling bonds (Fig. 3.1.e). By removing the other carbon atom from the three unsaturated carbons in Fig. 3.1.f, divacancy is formed which builds a pentagon-octagon-pentagon (5-8-5) structure.

3.3 Method of Calculations

In this research, the graphene sheets are modelled using supercell approach with 6×6 unit cells. To study the adsorption of the Li-polysulfides on the graphene, a supercell which includes a Li_2S_x (x =4, 6, 8) molecule on the graphene sheet is used. The vacuum thickness between the images is 17 Å . To reduce the computational effort the Li-polysulfide molecules with even number of S are studied. Integrations in reciprocal space are performed on a 3×3 Monkhorst-Pack k-point mesh grid for the surface unit cell. The full geometry optimization is done for Li_2S_x as well as pristine and defective graphene with and without Li_2S_x. All geometry optimizations are performed using the SeqQuest program [120, 121], which is a DFT code with localized basis sets represented by linear combinations of contracted Gaussian functions (double-zeta plus polarization) and norm-conserving pseudopotentials. The exchange-correlation energies are evaluated with the Perdew-Burke-Ernzerhof (PBE) functional [95], and the dispersion effects for van der Waals interactions are introduced by DFT-D2 method [105]. In our present study, this correction considerably strengthen the calculated interaction energy between $\mathrm{Li_2S}_x$ and graphene. Therefore, the distance between the Li-polysulfide molecules and graphene is shorter with dispersion correction. Here, we do not consider the effect of the graphene ripples because of the small size of the $\mathrm{Li_2S}_x$ molecules (< 6 Å) compared to the average wavelength of the ripples ($\lambda \sim 55$ Å [170]). Moreover, in order to correct for the basis set super position erros (BSSE), the Counterpoise method [119] is used. It is found that BSSE in current calculations results in over-binding by 17-19% which is calculated from the difference of biding energies evaluated with and without considering BSSE correction.

The zero point energies (ZPE) and vibrational free energies are obtained from the frequencies through Eq. 2.9.6. In order to estimate the rotational and translational entropy contributions to the Gibbs free energy (Eq. 2.9.1) at room temperature, the TURBOMOLE package of programs [171, 172] is employed. The rigid rotor and ideal gas approximations are used to respectively calculate the rotational and translational entropy for the Li-polysulfide molecules.

3.4 Results and Discussion

3.4.1 Li-Polysulfides

First, we study different possible arrangements of Li and S atoms in $\mathrm{Li_2S}_x$ ($x = 4, 6, 8$). The structures reported in Ref. [18] are also considered. Figure 3.2 illustrates our obtained minimum-energy structures. The most stable geometries are found to be like an open ring which are in agreement with the previous results [18]. Also the bond lengths in the $\mathrm{Li_2S}_x$ molecules are calculated. Table 3.1 presents the distance between two bonded atoms for all structures in

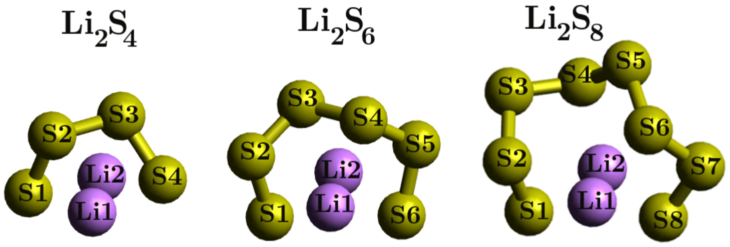

Figure 3.2: Atomic structures of Li_2S_4, Li_2S_6, and Li_2S_8 molecules.

our calculations and in Ref. [18]. It is demonstrated that at the open ends of each Li_2S_x ring, the bond lengths between sulfur atoms are slightly shorter than that of the other S–S bonds. It is also found that the lengths of the Li–S ionic bonds are the same in all Li_2S_x molecules. However, the larger the x value in Li_2S_x, the shorter the Li–Li bond length.

Table 3.1: Bond lengths (in Å) for S–S, S–Li, and Li–Li atoms in Li_2S_x molecules presented in Fig. 3.2. The values in parentheses are from Ref. [18]. Included with permission from Jand *et al.* [158](© 2016 Elsevier B.V.)

	Li_2S_4	Li_2S_6	Li_2S_8
S1–S2	2.11 (2.103)	2.08 (2.094)	2.09
S2–S3	2.14 (2.118)	2.08 (2.078)	2.08
S3–S4	2.12 (2.103)	2.24 (2.092)	2.14
S4–S5	–	2.07 (2.079)	2.09
S5–S6	–	2.09 (2.094)	2.12
S6–S7	–	–	2.10
S7–S8	–	–	2.08
Li1–Li2	2.79	2.63	2.58
S1–Li1	2.37	2.41	2.42

In order to study the atomic charge distribution in Li-polysulfides, the Mulliken charge populations [173] on the Li and S atoms are calculated (listed in Tab. 3.2). Mulliken population analysis usually gives a qualitative estimation of partial atomic charges. The binding of the Li atoms to the S atoms induces the charge redistribution from Li to S at the open ends of all the studied Li-polysulfide molecules.

3.4.2 The Pristine and Defective Graphene

In the next step, the geometries and the total energies of pristine and defective graphenes are calculated. To estimate the formation energies of the defective graphene structures, we use the equation

$$E_{\mathrm{d}} = E^{\mathrm{tot}}_{\mathrm{defective}} - E^{\mathrm{tot}}_{\mathrm{pristine}} + n_{\mathrm{v}} E^{\mathrm{tot}}_{\mathrm{C}}, \tag{3.4.1}$$

in which $E^{\mathrm{tot}}_{\mathrm{defective}}$, $E^{\mathrm{tot}}_{\mathrm{pristine}}$, and $E^{\mathrm{tot}}_{\mathrm{C}}$ are respectively the total energy of the defective and the pristine graphene sample, and energy per carbon of pristine graphene. n_{v} is the number of vacant C atoms in the graphene samples with vacancy.

The obtained formation energy of a 55-77 SW defect is calculated to be 5.27 eV, while the structure with the SW-like 555555-777-9 defect has the formation energy of 16.75 eV. $E_{\mathrm{d}}^{\mathrm{SW}}$=5.27 eV is in agreement with another DFT study [174], where the formation energy for a SW on graphene has been reported to be 5.53 eV using PBE functional and plane-wave basis set. Our calculated formation energy for a monovacancy on graphene is $E_{\mathrm{d}}^{\mathrm{MV}}$=7.76 eV, which is consistent with the result of a DFT-GGA study using PW functional and numerical basis set (7.63 eV) [175], and with the result of another theoretical research using the same functional but double numerical basis set with polarization (7.85 eV) [176], as well as experimental value of 7.0±0.5 eV [177]. Furthermore, in agreement with reported $E_{\mathrm{d}}^{\mathrm{DV}}$=8.08 eV in the former DFT-PW study [175], we calculate the formation energy of the divacant structure to be 8.03 eV. The results show that graphene with divacancy is slightly less favorable than the monovacant structure. In general, it is indicated that graphene with the 55-77 SW defect is more stable than the structures with the SW-like 555555-777-9 defect or point-defects. Moreover, the most unfavorable defect in our study is found to be the SW-like 555555-777-9 defect.

Table 3.2: Mulliken population analysis (MPA) for $\mathrm{Li_2S}_x$ molecules presented in Fig. 3.2. Included with permission from Jand *et al.* [158](© 2016 Elsevier B.V.)

	Li1	Li2	S1	S2	S3	S4	S5	S6	S7	S8
$\mathrm{Li_2S_4}$	0.369	0.373	-0.324	-0.048	-0.047	-0.323	–	–	–	–
$\mathrm{Li_2S_6}$	0.346	0.347	-0.288	-0.003	-0.057	-0.058	-0.001	-0.286	–	–
$\mathrm{Li_2S_8}$	0.346	0.336	-0.282	-0.035	0.021	-0.054	0.019	-0.056	0.013	-0.308

3.4.3 Li-Polysulfides on the Pristine and Defective Graphene

The adsorption of Li_2S_x ($x = 4$, 6, 8) molecules on the most favorable structures of graphene, namely pristine, SW-defective, and monovacant graphene, is studied. First, we consider different possible orientations of the Li_2S_x molecules at various sites of the pristine graphene (Fig. 3.3), and by calculating the binding energies, we investigate the feasibility of Li_2S_x adsorption on graphene. It is indicated that the binding of Li_2S_4 via S atom to the graphene sheet is very weak ($\geq -0.17\,\text{eV}$). Therefore, we only focus on the adsorption of Li_2S_x on graphene through Li atoms. The binding energies of Li-polysulfides to the pristine graphene at 0 K without ZPE corrections are presented in Fig. 3.3. It is shown that in all the studied cases, Li atoms tend to bind to the hollow site on graphene. We also examine various configurations of the

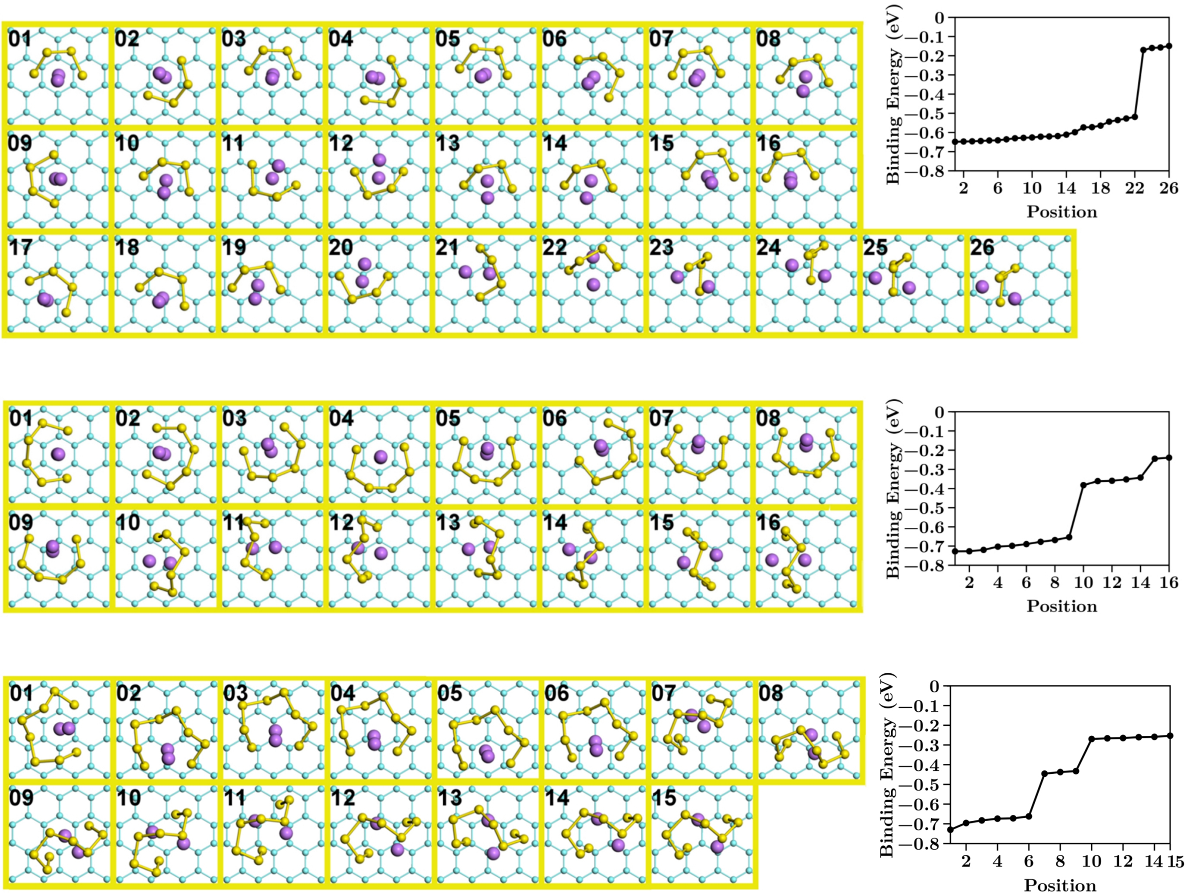

Figure 3.3: Top views of the considered structures and binding energies of Li_2S_4, Li_2S_6, and Li_2S_8 on pristine graphene. Included with permission from Jand *et al.* [158](© 2016 Elsevier B.V.)

Table 3.3: Binding energies (in eV) of $\mathrm{Li_2S}_x$ molecules on pristine as well as defective SW 55-77, monovacant, and S-doped graphene. ΔE values are binding energies at 0 K (without zero-point energy correction). ΔG is the change in Gibbs free energy of adsorption with respect to an ideal gas phase of the molecules at 300 K and 1 atm.

	(eV)	$\mathrm{Li_2S_4}$	$\mathrm{Li_2S_6}$	$\mathrm{Li_2S_8}$
pristine	$\Delta E =$	-0.65	-0.72	-0.73
pristine	$\Delta G =$	0.02	-0.04	-0.03
SW 55-77	$\Delta E =$	-0.70	-0.78	-0.86
SW 55-77	$\Delta G =$	0.05	-0.04	-0.05
1-vac	$\Delta E =$	-3.83	-4.48	-4.64
1-vac	$\Delta G =$	-2.85	-3.27	-3.51
1-vac+1S	$\Delta E =$	-0.76	-0.83	-0.71
1-vac+1S	$\Delta G =$	-0.08	-0.09	0.00

$\mathrm{Li_2S}_x$ molecules on graphene with the SW defect. Table 3.3 shows the adsorption energy (ΔE) of the most favorable structures of the Li-polysulfides on the pristine graphene as well as the SW-defective graphene. The binding energy of the latter system is calculated to be marginally larger. Moreover, to study the effect of dispersion correction on the binding energies, ΔE values for the adsorption of the $\mathrm{Li_2S}_x$ ($x = 4, 6, 8$) on pristine graphene are calculated without considering the dispersion correction. These values are $-0.02\,\mathrm{eV}$, $-0.04\,\mathrm{eV}$, and $-0.06\,\mathrm{eV}$, respectively.

To estimate the error in the calculations of binding energies, AIMD simulations for all the optimized structures presented in Tab. 3.3 are carried out in microcanonical ensemble (NVE) for 100 steps. For each step, the (BSSE-free) binding energy is calculated. Then, the standard deviation for binding energies of all snapshots is considered as the error in each Li-polysulfide case. These values are compared to the binding energies reported in Tab. 3.3, and they are found to be less than 2% for all cases.

For a more accurate study of the $\mathrm{Li_2S}_x$ adsorptions on graphene, the change of the Gibbs free energy (ΔG) during the adsorption process is calculated. To evaluate ΔG, total energies, ZPEs, PV term, as well as vibrational, rotational, and translational contributions of thermal energy and entropy are computed. In Tab. 3.3, ΔG for the Li-polysulfides on the pristine and the SW-defective graphene at 300 K and 1 atm are provided. In the case of Li_2S_4, the positive value of ΔG proves the unfavorable process of binding to graphene. On the other hand, change in the Gibbs free energies for adsorption of Li_2S_6 and Li_2S_8 on the pristine and the SW-defective graphene are slightly negative, which we interpret as the spontaneous adsorptions. However, the small values of ΔG show a physical binding (physisorption) of the Li_2S_x ($x = 6, 8$) to graphene. The other reason to describe the binding processes of the Li_2S_6 and Li_2S_8 molecules to graphene as physisorption is the considerable difference between the adsorption energies calculated with and without dispersion correction, which shows that in both cases the main interaction energy is due to van der Waals interaction.

Similar calculations to evaluate ΔE and ΔG are carried out for the monovacant graphene, and the obtained values are presented in Tab. 3.3. In addition, we investigate the adsorption of the Li-polysulfide molecules with odd number of S atoms (Li_2S_x ($x = 3, 5, 7$)) as well as S_8 molecule on the graphene with monovacancy. In all the studied Li-polysulfides, a sulfur from the open end of Li_2S_x ring binds to the vacant site on the graphene during geometry optimization. Figure 3.4 indicates that the mentioned S atom is dissociated from the molecule,

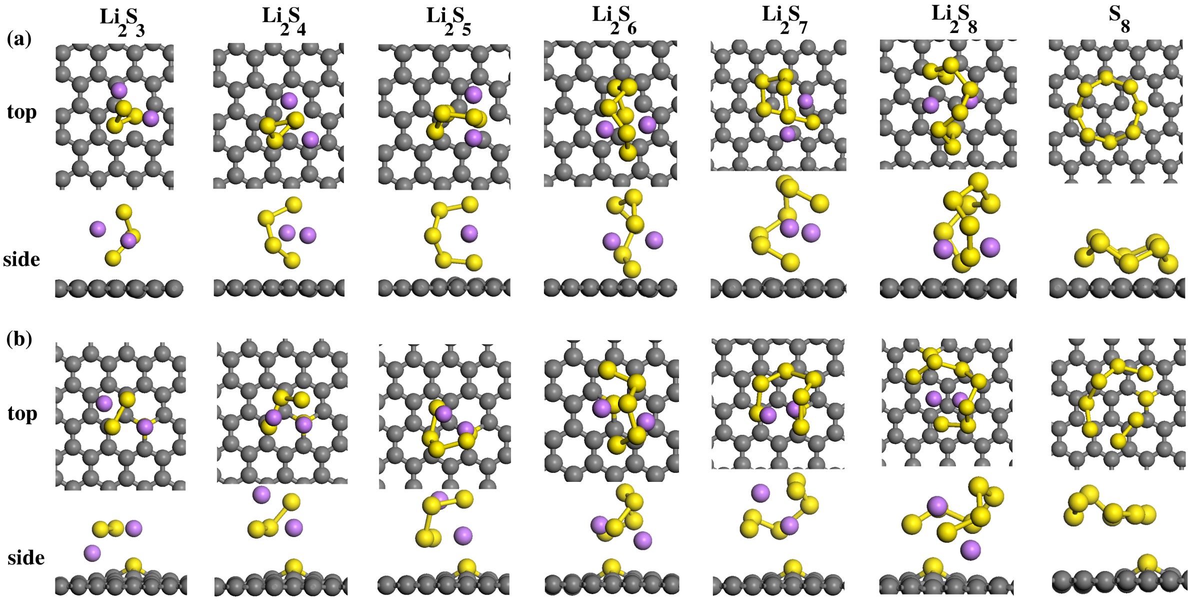

Figure 3.4: (a) Initial and (b) final structures for the dissociation of Li_2S_x ($x = 3, 4, 5, 6, 7, 8$) and S_8 on monovacant graphene. Included with permission from Jand *et al.* [158](© 2016 Elsevier B.V.)

and consequently, Li_2S_{x-1} molecule is formed. Also in the case of S_8, one S atom above the vacancy is separated from the molecule. The detached S atom makes a strong bond with the C atoms around the vacancy on graphene. Estimation of the bond lengths of dissociated sulfur and its nearest Li atom in Li_2S_4 before and after the geometry relaxation gives the values of 2.37 Å and 2.55 Å, respectively. This longer Li–S distance is due to the strong interaction of the S atom with the carbon dangling bonds, since the local charge redistribution around the dangling bonds brings about a large tendency towards interaction with electronegative elements [178].

Moreover, the binding of the detached S atom on the graphene to its former molecule is studied by calculating the interaction energies of Li_2S_{x-1}/(S-graphene) and Li_2S_{x-1}/(monovacant graphene) (x =4, 6, 8). Figure 3.5 is an illustration of the structures of Li_2S_5/(S-graphene) and Li_2S_5/(monovacant graphene). The interaction energy between Li_2S_{x-1} and the S-doped graphene is calculated using

$$\Delta E_{\mathrm{a}} = E_{\mathrm{tot}}^{\mathrm{LS_{x-1}/S-g}} - E_{\mathrm{tot}}^{\mathrm{S-g}} - E_{\mathrm{tot}}^{\mathrm{LS_{x-1}}}, \tag{3.4.2}$$

where $E_{\mathrm{tot}}^{\mathrm{LS_{x-1}/S-g}}$, $E_{\mathrm{tot}}^{\mathrm{S-g}}$, and $E_{\mathrm{tot}}^{\mathrm{LS_{x-1}}}$ are the total energies of the final structure, the isolated S-doped graphene, and the Li_2S_{x-1} structures, respectively. The last two energies are obtained by single point energy calculations when the structures are fixed in the positions of the re-

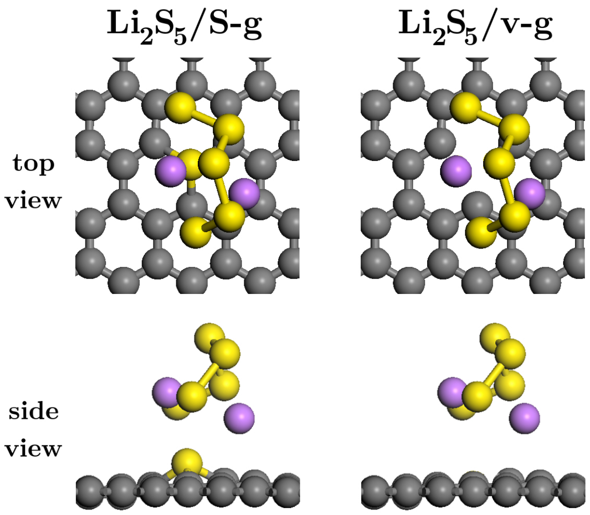

Figure 3.5: The structures of Li_2S_5/(S-graphene) and Li_2S_5/(monovacant graphene).

laxed Li_2S_{x-1}/(S-graphene) structure. Then, the interaction energy of the Li_2S_{x-1}/(monovacant graphene-without S) is evaluated by the single point calculations:

$$\Delta E_{\mathrm{b}} = E_{\mathrm{tot}}^{\mathrm{LS_{x-1}/v-g}} - E_{\mathrm{tot}}^{\mathrm{v-g}} - E_{\mathrm{tot}}^{\mathrm{LS_{x-1}}}, \tag{3.4.3}$$

in which $E_{\mathrm{tot}}^{\mathrm{LS_{x-1}/v-g}}$ and $E_{\mathrm{tot}}^{\mathrm{v-g}}$ are respectively the total energies of Li_2S_{x-1}/(monovacant graphene) and graphene with monovacancy as the atomic positions are set fixed to the relaxed Li_2S_{x-1}/(S-graphene) structure. Comparing the values of ΔE_{a} and ΔE_{b} (see Tab. 3.4), it is pointed out that ΔE_{a}-ΔE_{b} is very small, and the interaction energy of Li_2S_{x-1}/(S-graphene) is mainly due to Li_2S_{x-1}/(monovacant graphene) interaction. Therefore, we can conclude that the detached S binds weakly to the Li-polysulfide molecule.

In addition, the dissociation energies of a sulfur atom from the Li_2S_x ($x = 4, 6, 8$) and S_8 are calculated as 3.62 eV, 3.33 eV, 3.20 eV, and 3.33 eV, respectively. Moreover, the adsorption energy of a sulfur to the monovacant graphene is evaluated as 6.99 eV, which is larger than the energy loss during a S dissociation from the Li_2S_x molecules. Hence, a S atom can detach from the Li-polysulfide and bind to the vacant site of the graphene while the detachment activation energy is provided by the energy gain through adsorption of S to the graphene. In other words, the interaction of the Li_2S_x molecules with the monovacant site leads to graphene doping. It is expected that S dopant remains in its position on graphene during the charge/discharge cycles due to the strong binding of the sulfur to the carbon atoms at the vacant site. Thus, the S dopant can change the ability of the graphene to trap the Li-polysulfide.

Table 3.4: Binding energies (in eV) between Li_2S_x molecules and S/single-vacancy-graphene (ΔE_{a}) as well as between Li_2S_x molecules and single-vacancy-graphene (ΔE_{b}) as defined in Eqs. 3.4.2 and 3.4.3. Included with permission from Jand *et al.* [158](© 2016 Elsevier B.V.)

(eV)	Li_2S_3/S-g	(Li_2S_5)/S-g	(Li_2S_7)/S-g
ΔE_{a}	-0.41	-0.86	-0.85
ΔE_{b}	-0.29	-0.83	-0.77

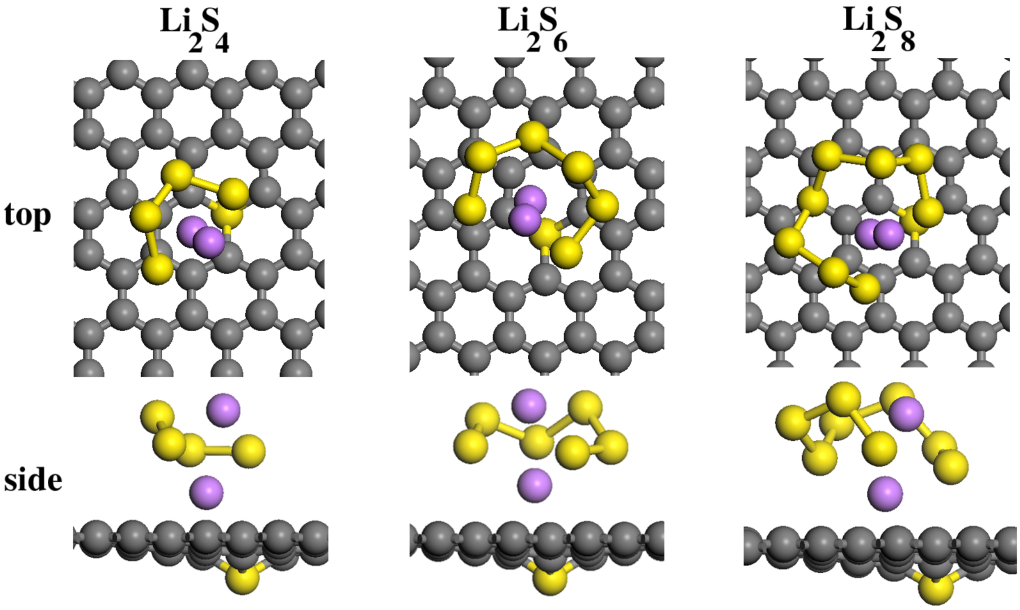

Figure 3.6: Top and side views of structures for adsorption of $\mathrm{Li_2S}_x$ (x = 4, 6, 8) on the S-doped graphene. Included with permission from Jand *et al.* [158](© 2016 Elsevier B.V.)

3.4.4 Li-Polysulfides on the S-Doped Graphene

Inspired by our previous results, we focus on the adsorption of the $\mathrm{Li_2S}_x$ ($x = 4$, 6, 8) on the S-doped graphene. Geometry optimizations done for the graphene with a S atom as dopant clarify that the sulfur atom tends to be located out of the plane of graphene. The S–C bond length in the most stable structure is 1.75Å, while for C–C is 1.42Å. When the Li-polysulfide molecule is placed on the graphene, the most favorable configuration is the one in which the S dopant and the molecule are on two opposite sides of the vacancy on the graphene sheet, and the $\mathrm{Li_2S}_x$ interacts via its Li side with graphene (Fig. 3.6). The binding energies and the Gibbs free energy differences for these structures are calculated (see Tab. 3.3). It is proven that the S-doped graphene cannot decrease the shuttle effect since the values of ΔE and ΔG only show a weak physisorption, and the Li-polysulfides cannot be trapped.

3.5 Conclusions

In this chapter, the ability of pristine and defective graphene to immobilize the Li-polysulfide has been studied. The atomic structures and the total energies of the $\mathrm{Li_2S}_x$ and the $\mathrm{Li_2S}_x$/graphene systems have been obtained at the DFT-PBE level of theory considering the dispersion correction. We have employed localized atomic double-zeta basis set plus polarization. Also the BSSE correction has been included in the interaction energies. It has been found that the main source of the binding between the $\mathrm{Li_2S}_x$ molecules and graphene is the dispersion energy. In all the studied pristine and (SW- and monovacant-) defective graphene samples, the binding energy of the $\mathrm{Li_2S}_x$ molecules and graphene increases with the number of S atoms (x). In the case of the monovacant graphene, a spontaneous dissociation of a S atom from the Li-polysulfides has been observed during geometry optimization. This sulfur atom binds to the vacant site resulting in a graphene doping. Its binding energy to the graphene is comparable to the energy required for detachment of a C atom from graphene. Therefore, the S atom should remain binded to the graphene during charging/discharging cycles. In the next step, the adsorption of the $\mathrm{Li_2S}_x$ molecules on the S-doped graphene has been investigated. It is found that the interaction energies of the $\mathrm{Li_2S}_x$ with the S-doped graphene are of the same order of magnitude as their interaction energies with the pristine and the SW-defective graphene samples. These energies are rather too small to make a strong binding between the molecules and graphene. In other words, the studied cases of graphene are not able to immobilize the Li-polysulfide molecules and they cannot improve the performance of the sulfur cathodes in the Li-S batteries. This result confirms the experimental finding that the suitable choices for the cathode material in such batteries are the carbon-S composites with closed structures to trap the Li-polysulfides, such as carbon nanofibers [31, 164]. In addition, some previous studies indicate that N-doped [179] or NP-doped [180] graphene may interact more strongly with the Li-polysulfides than graphene. Therefore, the effect of graphene doping with different dopants such as nitrogen and phosphorus on immobilization of the Li-polysulfides should still be thoroughly studied by theoretical modelling in order to find a promising cathode system for a high performance Li-S batteries.

Chapter 4

A THEORETICAL APPROACH TO STUDY SUPERIONIC PHASE TRANSITION IN Li_2S AS AN IONIC CRYSTAL [1]

4.1 Introduction

Superionic conductors are materials with highly mobile ions. The mobility of ions is often initiated by a high temperature or a high defect concentration [182]. The effect of temperature is very significant in superionic conductors. In these type of materials, above the threshold temperature of the superionic phase transition, one or more of the ion sublattices becomes disordered leading to a super-high ionic conductivity while the whole material structure remains solid. Superionic compounds have attracted increasing interest due to their applications in all-solid-state Li-ion batteries (ASSLB), fuel cells, and chemical sensors [44,183–187]. In ASSLBs, the ionic diffusion occurs via the hopping of ions in the crystal structure of a superionic material without the need for a liquid electrolyte. As it was mentioned in Chapter 1, replacing the organic liquid electrolyte with a solid ionic conductor can extremely improve the device safety and overcome one of the barriers for large-scale application of the Li-based batteries. Over the last few years, sulfur-based solid electrolytes have been reported to exhibit relatively higher ionic conductivity than those of standard liquid electrolytes. $Li_{10}GeP_2S_{12}$ with ionic conductivity of 1.2×10^{-2} S/cm [188] and Li_2S-P_2S_5 with ionic conductivity of 1.7×10^{-2} S/cm [189] are the examples of such solid electrolytes.

---

[1] This chapter is based on the results presented in Ref. [181]

Lithium sulfide (Li_2S) is a solid-state compound which has received much attention due to its applications in the Li-S batteries. In these batteries, the metallic lithium anode can be avoided by using Li_2S as a prelithiated cathode which is coupled by Si or Sn as an anode [36,190,191]. The electrical conductivity of the Li_2S cathode can be improved by adding carbon. Li_2S-C composites are promising cathode materials which can offer an opportunity to develop the Li-S batteries with higher energy density [37, 38, 192]. In addition, the ionic conductivity of Li_2S shows a higher value through the combination with solid electrolytes, e.g. Li_2S-P_2S_5 [189, 193]. Moreover, it has been experimentally reported that lithium sulfide exhibits a superionic conductivity at temperatures higher than $\sim$ 900 K [39], and its Li-ion conductivity has been reported to be 1.27×10^{-1} S/cm at 1170 K [40]. As the mechanism and rate of ionic diffusion in superionic solids play important roles in the performance and development of the Li-ion batteries, they have been studied experimentally and theoretically [194–201]. The common techniques to characterize the ionic conductivity in such systems are the experimental X-ray and neutron diffraction measurements [194–197] and theoretical molecular dynamics (MD) simulations [198–201]. In an experimental study, by using quasielastic neutron scattering, Altorfer $et\ al.$ [40] have suggested two models for the diffusion mechanism in the superionic phase of Li_2S, model (I) corresponds to vacancy hopping over Li Bravais lattice sites, and model (II) corresponds to Li jumps from regular sites to interstitial sites and vice versa. However, an atomic-scale picture of the conduction mechanisms in lithium sulfide is still missing. This information is necessary for developing methods to improve the ionic conductivity in the next-generation battery materials.

In this chapter, the crystal structures of the pristine Li_2S and Li_2S with a single vacancy are studied using *first-principles* computations. To investigate the Li-ion transport mechanism, we use a theoretical approach that can be applied to study the supersonic phase transition in arbitrary ionic structures. In this approach, we employ density functional theory (DFT) together with *ab initio* molecular dynamics (AIMD) simulations and thermodynamics of defects to calculate the concentration of mobile ions. Finally, the Li-ion conductivity is determined as a function of temperature.

4.2 Defect Formation Energy

Formation of defects can be viewed as a process in which a number of atoms and electrons are exchanged between the host material and the reservoirs. The formation energy of an atomic kind i with a defect type of d in charge state q is defined as [202–204]:

$$\Delta E_i^{d,q} = E_{\mathrm{tot}}^{d,q} - E_{\mathrm{tot}}^{\mathrm{bulk}} + \sum_i n_i \mu_i + q(\varepsilon_{\mathrm{F}} + \varepsilon_{\mathrm{VBM}}) + \Delta E_{\mathrm{corr}}. \tag{4.2.1}$$

$E_{\mathrm{tot}}^{d,q}$ is the total energy calculated for a supercell including the defect d, and $E_{\mathrm{tot}}^{\mathrm{bulk}}$ is the total energy for the pristine crystal using the same supercell. The n_i and μ_i are the number and chemical potential of atoms type i, respectively. In fact, the atom i can be introduced into (positive n_i) or removed from (negative n_i) the supercell to form the defect. The $\sum_i n_i \mu_i$ term represents the energy change due to exchange of atoms with the chemical reservoirs. $\varepsilon_{\mathrm{VBM}}$ indicates the energy at the valence band maximum (VBM), and it is the energy of removing an electron from the valence band. ε_{F} is the Fermi level referenced to the VBM of bulk structure. Lastly, ΔE_{corr} is a correction term that accounts for finite size effect and for electrostatic potential alignment of defective and pristine supercells [205]. ΔE_{corr} can be obtained through $\Delta E_{\mathrm{corr}} = -\alpha q^2/(2\epsilon L)$ [205, 206], where q is the defect charge, α and ϵ respectively represent the Madelung constant and the dielectric constant, and L is the supercell lattice size.

The energy of Fermi level for a defective system can be derived by considering charge neutrality [203, 207]. Therefore, the sum of charge density of defects d with charge q should be equal to the sum of hole and electron concentrations:

$$\sum_{d,q} q n^{d,q} = n_{\mathrm{h}} - n_{\mathrm{e}}. \tag{4.2.2}$$

$n^{d,q}$ is the concentration of defects d and is calculated using:

$$n^{d,q} = N_d \exp\left(-\frac{\Delta E_i^{d,q}}{k_B T}\right), \tag{4.2.3}$$

in which N_d is the number of maximum possible sites where defects d can be located. k_B and T are Boltzmann constant and temperature, respectively. The concentration of holes and electrons are obtained by integrating the electronic density of states in the pristine bulk $(g(\varepsilon))$ up to the VBM and from the conduction band minimum (CBM) considering the Fermi-Dirac distribution, $f(\varepsilon, \varepsilon_\mathrm{F})$:

$$\begin{aligned} n_\mathrm{h} - n_\mathrm{e} &= \int_{-\infty}^{\mathrm{VBM}} [1 - f(\varepsilon, \varepsilon_\mathrm{F})] g(\varepsilon) d\varepsilon - \int_{\mathrm{CBM}}^{\infty} f(\varepsilon, \varepsilon_\mathrm{F}) g(\varepsilon) d\varepsilon \\ &= \sum_{d,q} q N_d \exp\left(-\frac{\Delta E_i^{d,q}}{k_B T}\right). \end{aligned} \tag{4.2.4}$$

Equations 4.2.1 and 4.2.4 are solved self-consistently for a set of fixed temperature and chemical potential of each element. By knowing the Fermi energy, $\Delta E_i^{d,q}$ and defect concentrations are determined. Then, using Eq. 4.2.1, the Fermi energy is calculated from $\Delta E_i^{d,q}$, and it is accepted if its difference with the previously-calculated Fermi energy is less than a certain criterion.

4.3 Method of Calculations

First-principles calculations are performed using the Vienna *ab initio* simulation package (VASP) [122–125] at the DFT level of theory with the plane-wave basis set approach. The electron-electron exchange-correlation energy is described by the Perdew-Burke-Ernzerhof (PBE) functional [95]. Also, the projector augmented wave method (PAW) [208] is employed. We use a 2×2×2 supercell to model the bulk Li_2S. The Monkhorst-Pack technique [109] is applied to generate a 4×4×4 k-point mesh for Brillouin zone sampling. The atomic and electronic structures as well as defect formation energies of lithium sulfide are calculated with the energy cutoff of 360 eV for the plane-wave basis set.

To study Li diffusion mechansims, AIMD simulations (implemented in VASP) are carried out for pristine Li_2S and Li_2S with a single vacancy. Simulations are performed in the canonical NVT ensemble with time steps of 1 fs. We use the Nosé-Hoover thermostat to fix the temperature during the calculations. For the AIMD simulations, the bulk Li_2S is again modelled by $2\times2\times2$ supercell with $4\times4\times4$ Monkhorst-Pack k-point grid with an energy cutoff of 360 eV. In our current research, the AIMD simulations run up to 50 ps for Li_2S structure. To investigate all possible channels of Li-ion migration, the simulations are carried out at different temperatures of $T = 300, 600, 750, 830, 900, 1050, 1170,$ and 1300 K. The thermalization is achieved within 10 ps and the following 40 ps are used for structure sampling to calculate the diffusion coefficient.

Using AIMD trajectories, the mean square displacement (MSD) is calculated by

$$\mathrm{MSD}(\tau) = \frac{1}{N_{ion}}\frac{1}{N_{step}-\tau} \times \sum_{j=1}^{N_{ion}} \sum_{i=1}^{N_{step}-\tau} |\vec{r}_j(t_i+\tau) - \vec{r}_j(t_i)|^2, \tag{4.3.1}$$

where τ represents lag time, N_{ion} is the number of diffusing Li ions, and N_{step} is the number of AIMD time steps which is 40000 (for 40 ps) in the current study. Afterwards, diffusion coefficient D is evaluated using the Einstein relation:

$$D = \lim_{\tau\to\infty} \frac{\mathrm{MSD}(\tau)}{6\tau}. \tag{4.3.2}$$

Then, the ionic conductivity σ as a function of temperature is derived via the Nernst-Einstein relation:

$$\sigma = \frac{nq^2F^2}{\mathrm{RT}}D \tag{4.3.3}$$

in which n, q, F, R, and T are the number of carriers per unit volume, the carrier charge, Faraday constant, gas constant, and temperature, respectively.

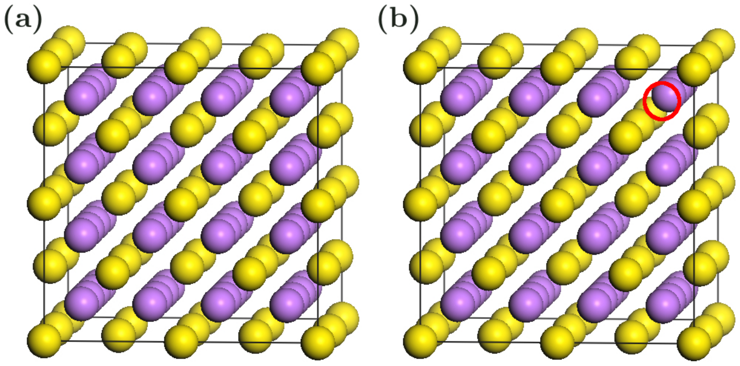

Figure 4.1: Atomic structures of 2×2×2 supercell of (a) pristine Li_2S, and (b) Li_2S with a single vacancy. Purple and yellow circles respectively indicate Li and S ions.

4.4 Results and Discussion

To understand the topology of Li sites in lithium sulfide, we first focus on the crystal structure of Li_2S with space group $Fm3m$. Figure 4.1.a shows the stable atomic configuration of the bulk Li_2S (2×2×2 supercell) after geometry optimization using DFT-PBE. In this compound, the sulfur (anion) sublattice has an fcc structure, and the Li atoms (cations) can be viewed as a simple cubic structure with the lattice size of $\frac{1}{2}a$ (a is the lattice constant of the Li_2S unit cell), while the cube center is occupied by anions.

In the previous study of our group [209], the diffusion pathways in Li_2S were calculated with the Nudge Elastic Band (NEB) method. Considering Li hopping to nearby single Li vacancy and Li hopping between regular lattice sites and interstitial sites, it has been reported that the diffusion barrier in the former case is lower [209]. In addition, the activation energy for formation and diffusion ($\Delta E_{\text{activation}} = \Delta E_{\text{formation}} + \Delta E_{\text{diffusion}}$) of Li vacancy was found to be lower than that of the interstitial Li. Thus, it can be concluded that Li vacancy possesses a more dominant role in Li-ion conductivity of Li_2S.

By performing AIMD simulations for Li_2S with a single vacancy (Fig. 4.1.b), the total mean square displacements of all diffused Li ions (MSD(τ)) are calculated as a function of lag time at different temperatures. Figure 4.2.a. presents the MSD curve versus τ. As only few number of

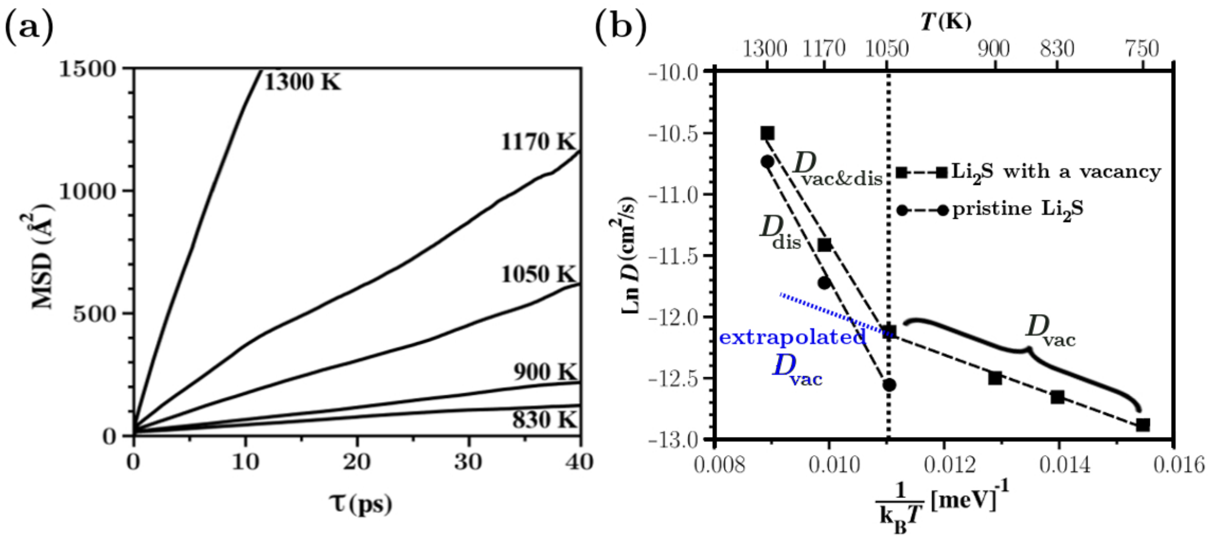

Figure 4.2: (a) Total mean square displacements (MSD) versus lag time (τ) calculated for 40 ps AIMD simulations for all mobile Li ions in $\mathrm{Li_2S}$ with a single vacancy. (b) Arrhenius plot of diffusion coefficients (D) for $\mathrm{Li_2S}$.

Li vacancy jumps can be detected at temperatures less than 750 K, they are not included in the MSD plot (Fig. 4.2.a). At higher temperatures, more than 32 Li hoppings are observed during 40 ps of the AIMD simulations.

Li diffusion coefficient (D) is derived from the Einstein relation 4.3.2. In Fig. 4.2.b, black squares represent the calculated $\log D$ for $\mathrm{Li_2S}$ with one Li vacancy at various temperatures. As it is shown in Fig. 4.2.b, there is a change in the slope of the Arrhenius plot which indicates two different mechanisms for Li diffusion. At low temperatures ($T <\sim 1050$ K), simple Li vacancy hopping occurs while the different behavior at higher temperatures is related to the superionic phase transition in $\mathrm{Li_2S}$.

In order to visualize the Li migration pathways, the probability densities of ions are plotted within the $\{110\}$ planes of $\mathrm{Li_2S}$ with a single vacancy at different temperatures (Fig. 4.3). This plot which is obtained from the sum over all ion trajectories over the simulated time helps us detect the lattice regions which are most frequently visited by the mobile Li ions. It can be seen in Fig. 4.3 that at low temperatures such as $T = 830$ K, the Li diffusion happens predominantly due to the vacancy hopping through the channels between the regular Li sites (so called 8c sites) along the $< 100 >$ axes. At higher temperatures, the trajectories of Li ions extend along

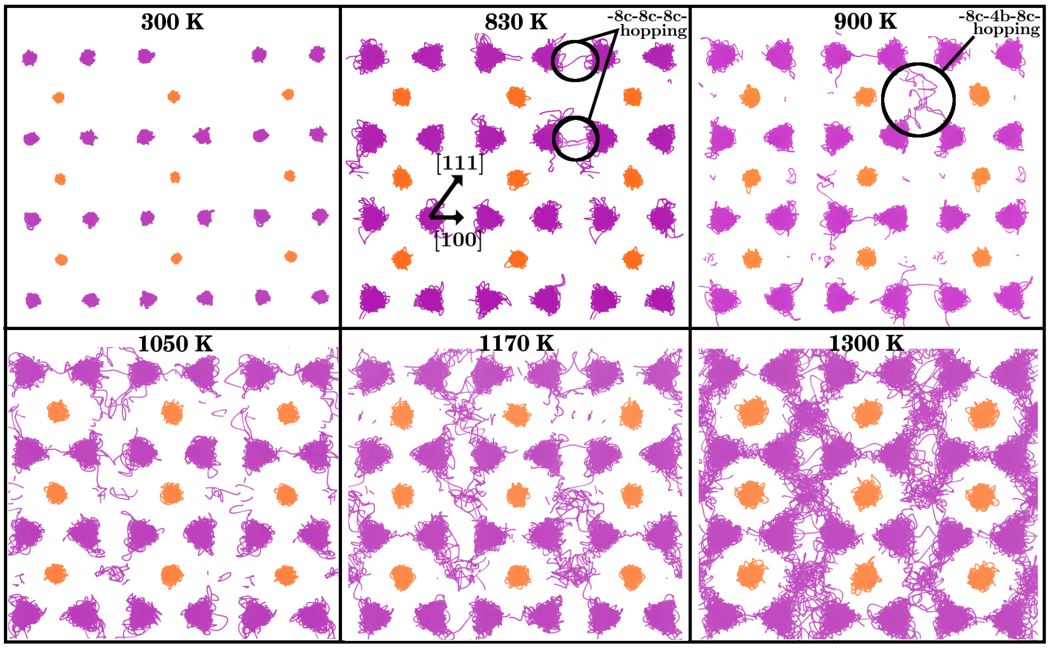

Figure 4.3: Accumulated all ion trajectories over the AIMD simulation time (40 ps) on the $\{110\}$ planes of Li_2S at 300 K, 830 K, 900 K ,1050 K, 1170 K and 1300 K. The visited positions by Li and S ions are in purple and gold, respectively. Included with permission from Jand *et al.* [181] (© 2017 Macmillan Publishers Limited, part of Springer Nature.)

the $< 111 >$ directions (see Fig. 4.3). For example, at $T = 900\,\mathrm{K}$, few Li hoppings from the regular 8c sites to the interstitial sites (so called 4b sites) are observed while Li migration mainly occurs via the simple Li vacancy hopping (–8c–8c–8c–). At $T = 1050\,\mathrm{K}$, both mechanisms have considerable contributions in Li diffusion. However, Li migration at $1170\,\mathrm{K}$ and $1300\,\mathrm{K}$ is mainly along the –8c–4b–8c– pathway, i.e. from the regular sites to the interstitial sites and vice versa. This finding confirms Li diffusion models suggested in the experimental study by Altorfer *et al.* [40] for the superionic phase of Li_2S.

In Fig. 4.2.b, Arrhenius plot at low temperatures is a result of the only possible mechanism for Li migration, namely the vacancy hopping (D_{vac}). For temperatures higher than $1050\,\mathrm{K}$, $\log D_{\mathrm{vac}}$ is obtained by extrapolating the low temperature values of $\log D_{\mathrm{vac}}$ to the higher temperatures. To study Li diffusion through –8c–4b–8c– channel, AIMD simulations are performed for pristine Li_2S (modelled using $2{\times}2{\times}2$ supercell) at $T = 1050, 1170,$ and $1300\,\mathrm{K}$. In this structure, Li migration is due to the occupation of the interstitial sites (4b) by Li ions. The calculated $\log D_{\mathrm{dis}}$ values (black circles in Fig. 4.2.b) at 1170 and 1300 K are close to that in Li_2S with a single vacancy ($\log D_{\mathrm{vac\&dis}}$) which shows that at these temperatures, the Li diffusion is more probable via interstitial sites in Li_2S with a vacancy.

The diffusion coefficient at 1170 K is calculated to be $D_{\mathrm{vac\&dis}} = 1.03 \times 10^{-5}$ cm^2/s, including the Li diffusion along both –8c–8c–8c– and –8c–4b–8c– pathways (superionic phase). This calculated value is in good agreement with the experimental values of $1.39{\times}10^{-5}$ cm^2/s [40] and $1.17{\times}10^{-5}$ cm^2/s [210] at 1170 K.

In order to identify the most favorable defect types in poor-ionic conductor phase, the defect formation energy ($\Delta E_i^{d,q}$) is calculated using Eq.4.2.1. As it was mentioned in section 4.2, ΔE_{corr} in Eq.4.2.1 depends on the unit cell size and the dielectric constant (ϵ). Here, we use the experimental value of the dielectric constant which has been reported by Yang $et\ al.$ to be $\epsilon \sim 10$ in Li_2S at room temperature [211]. In addition, μ_{Li} is considered to be in the range of thermodynamical stability of Li_2S with respect to bulk Li and S. That is, μ_{Li} may not exceed the chemical potential of bulk Li. If μ_{Li} highly increases (i.e. Li-rich limit), the bulk Li would start to form at the surface of Li_2S. Therefore, we set the zero value of μ_{Li} to the chemical potential of the Li-rich limit, which is defined as the total energy per atom of the Li crystal. Similarly, the lowest limit is a μ_{Li} value at which Li_2S starts to decompose to the bulk S (i.e. in the Li-poor limit). Hence, the allowed values for μ_{Li} lie between zero and half of the Gibbs free energy of Li_2S formation.

$\Delta E_i^{d,q}$ and ε_F are iteratively calculated from the Eqs. 4.2.1 and 4.2.4. We employ the experimental Gibbs free energy of formation of Li_2S which is ~ -4.58 eV [212], and the defect formation energy is calculated for different μ_{Li} in the range of $-2.3\,\mathrm{eV} \leq \Delta\mu_{\mathrm{Li}} \leq 0.0\,\mathrm{eV}$. The evaluated $\Delta E_i^{d,q}$ values are presented for different defect types in Fig. 4.4. According to these values, interstitial Li (Li^+) and Li vacancy ($\mathrm{V}_{\mathrm{Li}}^-$) are found to be the most favorable charge carriers in Li_2S. Considering Fig. 4.4, we study the defect formation energies in two ranges of $\Delta\mu_{\mathrm{Li}}$:

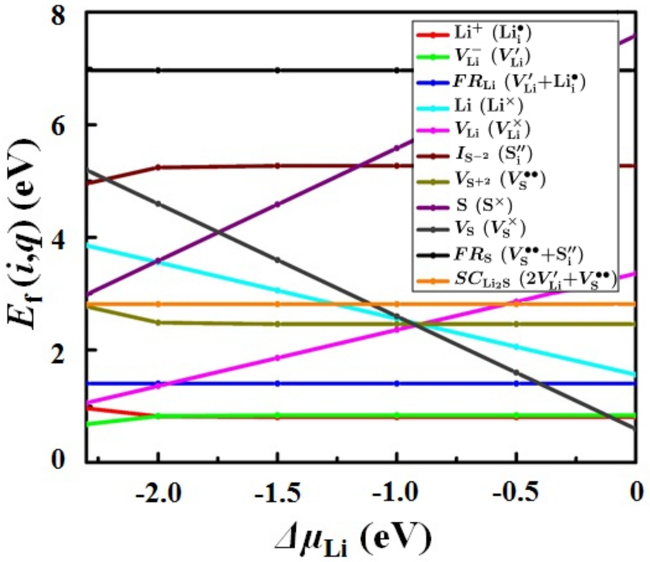

Figure 4.4: Formation energies of different defect types in bulk Li_2S as a function of $\Delta\mu_{\mathrm{Li}}$. Kroger-Vink representations are given in parentheses. Included with permission from Jand *et al.* [181] (© 2017 Macmillan Publishers Limited, part of Springer Nature.)

–2.0 eV $<$ $\boldsymbol{\Delta\mu_{\mathrm{Li}}}$ $\leq$ 0.0 eV: The formation energy of the Li vacancy ($\Delta E^{V_{\mathrm{Li}}^-}$) in this range is 0.80 eV, which is similar to the formation energy of the Li^+ interstitial ($\Delta E^{Li^+} = 0.81$ eV). Consequently, there is a high possibility of formation of Frenkel (V_{Li}^- + Li^+) pairs in Li_2S for –2.0 eV $<$ $\Delta\mu_{\mathrm{Li}}$ $\leq$ 0.0 eV. Therefore, the ionic migration happens via the Frenkel pair diffusion. Moreover, the formation energies of Li^+, V_{Li}^-, and Frenkel defect do not change with $\Delta\mu_{\mathrm{Li}}$ at this range, arising from the fact that the Fermi energy and the chemical potential of Li equally increase within –2.0 eV $<$ $\Delta\mu_{\mathrm{Li}}$ $\leq$ 0.0 eV and they cancel out each other.

–2.3 eV $\leq$ $\boldsymbol{\Delta\mu_{\mathrm{Li}}}$ $\leq$ –2.0 eV: In this range, $\Delta E^{V_{\mathrm{Li}}^-}$ gets lower and it reaches the value of 0.68 eV for $\Delta\mu_{\mathrm{Li}}$ = –2.3 eV, while ΔE^{Li^+} increases in this range. Therefore, the minimum activation energy is calculated for the formation and diffusion of the Li vacancy at $\Delta\mu_{\mathrm{Li}}$ = –2.3 eV, $\Delta E^{V_{\mathrm{Li}}^-}_{\mathrm{formation}} + \Delta E^{V_{\mathrm{Li}}^-}_{\mathrm{diffusion}} = 0.95$ eV (the diffusion barrier was obtained to be 0.27 eV [209]). The Fermi energy lowers and gets closer to the VBM, which in turn, results in a higher concentration of the holes. Therefore, the ionic conductivity within –2.3 eV $\leq$ $\Delta\mu_{\mathrm{Li}}$ $\leq$ –2.0 eV (i.e. in the Li-poor limit) occurs through the mechanism of the formation and diffusion of the Li

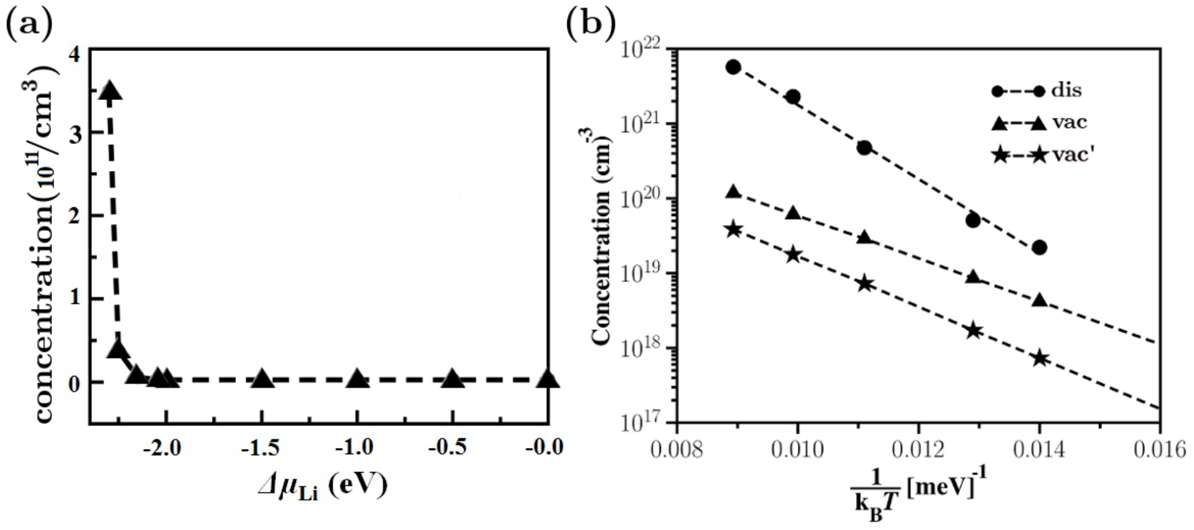

Figure 4.5: (a) Concentration of Li vacancy as a function of $\Delta\mu_{\mathrm{Li}}$. (b) Li vacancy concentration which is derived using Eqs. 4.2.1 and 4.2.4 for –2.3 eV $\leq$ $\Delta\mu_{\mathrm{Li}}$ $\leq$–2.0 eV (n_{vac}) and –2.0 eV $<$ $\Delta\mu_{\mathrm{Li}}$ $\leq$0.0 eV ($n_{\mathrm{vac}'}$) as well as the concentration of the interstitial Li calculated by Eq. 4.4.1 (n_{dis}). Included with permission from Jand *et al.* [181] (© 2017 Macmillan Publishers Limited, part of Springer Nature.)

vacancy.

The concentration of the Li vacancy in the poor-ionic conductor phase ($n_{V^-_{\mathrm{Li}}}$) is calculated for the allowed range of chemical potentials μ_{Li} and is depicted in Fig.4.5.a. It is found that within $-2.0\,\mathrm{eV} <$ $\Delta\mu_{\mathrm{Li}}$ $\leq$ $0.0\,\mathrm{eV}$ range, the Li vacancy concentration does not change with $\Delta\mu_{\mathrm{Li}}$ and it is calculated to be $n_{\mathrm{vac}'}$=2.8$\times$10^9 cm^{-3}, while in the Li-poor limit with minimum $\Delta\mu_{\mathrm{Li}}$, the vacancy concentration increases and it reaches its highest value of n_{vac}=3.5$\times$10^{11} cm^{-3} at $\Delta\mu_{\mathrm{Li}} = -2.3\,\mathrm{eV}$.

In the superionic phase, two mechanisms of the Li diffusion in Li$_2$S allow for two different hopping rates ($1/t$), namely the hopping rate in the regular sites $1/(t_{8\mathrm{c}})$, and the hopping rate between the regular and the interstitial sites $1/(t_{4\mathrm{b}})$. These hopping rates can be related via the detailed balance condition:

$$\frac{n_{8\mathrm{c}}}{t_{8\mathrm{c}}} = \frac{n_{4\mathrm{b}}}{t_{4\mathrm{b}}}, \tag{4.4.1}$$

where $n_{8\mathrm{c}}$ and $n_{4\mathrm{b}}$ are respectively the concentrations of Li on the regular and the interstitial sites, such that $n_{8\mathrm{c}} + n_{4\mathrm{b}} = n_{\mathrm{Li}}$ (n_{Li} is the total concentration of Li in the system and is 4.27$\times$10^{22} cm^{-3} for the lattice constant of 5.72 Å). Moreover, $t_{8\mathrm{c}}$ and $t_{4\mathrm{b}}$ are respectively the

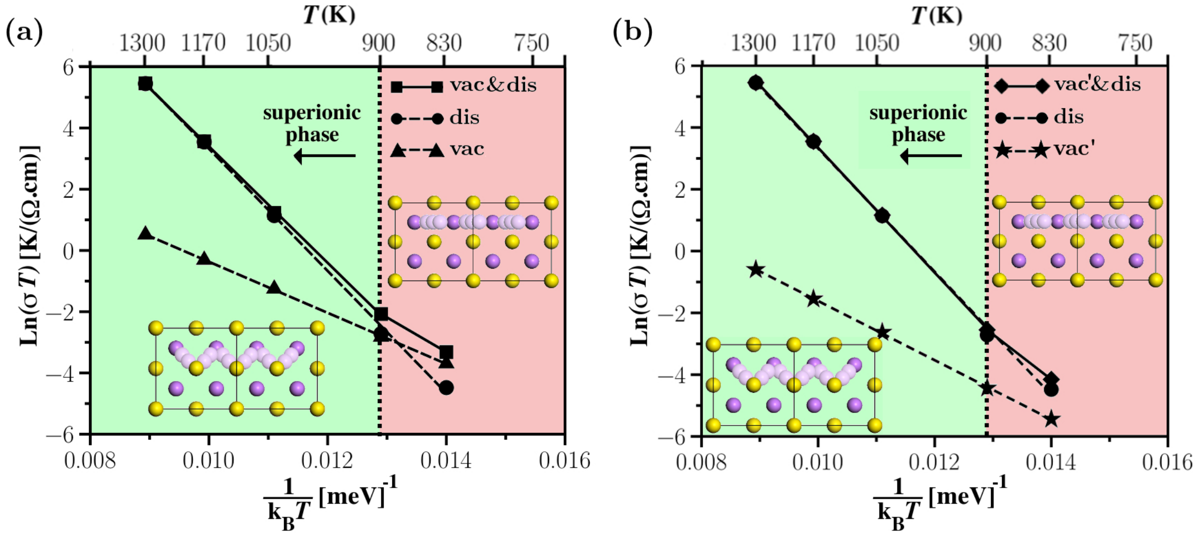

Figure 4.6: Li-ion conductivities as functions of temperature for (a) high Li vacancy concentration, $\sigma_{\text{vac\&dis}}$, and (b) low concentration, $\sigma_{\text{vac}'\&\text{dis}}$. Included with permission from Jand *et al.* [181] (© 2017 Macmillan Publishers Limited, part of Springer Nature.)

residence times for Li at the 8c and the 4b sites during the AIMD simulations. Figure 4.5.b shows the calculated values of $n_{4\text{b}}$ (which is same as n_{dis}) at $T = 830, 900, 1050, 1170$ and $1300\,\text{K}$. It is found that at $1300\,\text{K}$, the concentration of 4b defects in the superionic phase is 48.6 times larger than the maximum possible concentration of V_{Li}^{-} (n_{vac}) in poor-ionic conductor phase of Li_2S. Finally, Li-ion conductivity in Li_2S is calculated using the Nernst-Einstein Eq. 4.3.3:

$$\sigma_{\text{tot}} = \sigma_{\text{vac}} + \sigma_{\text{dis}} = \frac{q^2 F^2}{\text{RT}} \left[n_{\text{vac}} D_{\text{vac}} + n_{\text{dis}} D_{\text{dis}} \right], \tag{4.4.2}$$

in which n_{vac} and n_{dis} are the concentrations of vacancy hopping ($n_{V_{\text{Li}}^{-}}$) in the poor-ionic conductor phase and disordered hopping ($n_{4\text{b}}$) in the superionic phase, respectively. The Li-ion conductivity (σ) in Li_2S is determined for various temperatures considering two different concentration regimes based on $\Delta\mu_{\text{Li}}$, i.e. n_{vac} and $n_{\text{vac}'}$. In Fig. 4.6.a, σ is illustrated as a function of temperature for –2.3 eV $\leq \Delta\mu_{\text{Li}} \leq$ –2.0 eV (with high Li vacancy concentration). As can be seen in this figure, the superionic phase trasition is estimated to occur at $900\,\text{K}$. This finding is in agreement with the temperatures of the superionic phase transition in Li_2S observed by Buehrer *et al.* [39] and Altorfer *et al.* [40] through neutron scattering, which are $\sim 900\,\text{K}$ and

$\sim$ 800 K, respectively. Fig. 4.6.b shows the Li-ion conductivity for low concentration regime. Here, the superionic phase trasition is not completely clear and it is not discussable at this stage.

At 1170 K, we calculate the Li-ion conductivity to be $\sigma = 3.02 \times 10^{-2}$ S/cm, which is about four times smaller than the experimental value of $\sim$1.27 $\times 10^{-1}$ S/cm estimated from the curve of σ versus T in ref. [40]. This inconsistency may rise from the errors in the computational and experimental evaluations. Additionally, the computational limit for the AIMD simulations can result in the underestimation of $n_{\rm dis}$ which is used to calculate σ from Eq. 4.4.2.

The fraction of $\sigma_{\rm dis}/\sigma_{\rm vac}$ at 900 K, 1170 K and 1300 K are evaluated to be 1.1, 47.1, and 138.9, respectively. These values show that the ionic conductivity in the superionic phase increases with respect to σ in the poor-ionic regime by one to two orders of magnitude depending on temperature. Furthermore, the calculated σ at 300 K has a very small value of 9.43 $\times 10^{-17}$ S/cm, which is consistent with the reports expressing that Li_2S at room temperature has a very low ionic conductivity [40, 198, 213, 214].

4.5 Conclusions

Here, DFT calculations and AIMD simulations have been applied to determine the diffusion coefficient of Li in the pristine and defective bulk Li_2S, which has attracted lots of interest as a cathode material for the Li-S batteries. By studying the thermodynamic and kinetic properties of the system, we have evaluated the defect concentration and ionic conductivity as a function of temperature. According to the AIMD simulation, it is found that Li-ion migration takes place through the vacancy hopping in the Li regular sites at low temperatures. Moreover, the mechanism of Li hopping to the interstitial sites is observed at and above the temperature of superionic phase transition, which has been previously reported by experimental researchers to be between 800 K and 900 K [39, 40]. At higher temperatures (such as 1170 K), Li diffusion via hopping from the regular sites to the interstitial sites is more substantial.

By calculating the defect formation energy in Li_2S, we have found that the Li vacancy (V_{Li}^{-}) and interstitial Li^{+} have similar formation energies within –2.0 eV $< \Delta\mu_{\mathrm{Li}} \leq$ 0.0 eV, while the former defect type is more favorable in the Li-poor limit. Furthermore, the activation energies of these two defect types have been calculated. Although the activation energy for the Li vacancy hopping is lower than the Li interstitial diffusion, it is high enough to justify the low ionic conductivity of Li_2S at room temperature.

In addition, by plotting ionic conductivity σ versus T, it can be pointed out that the phase-transition temperature is $\sim 900\,\mathrm{K}$, which is in agreement with aforementioned experimental data. However, the diffusion coefficient plot indicates a considerable change in its slope at $T = 1050\,\mathrm{K}$, showing that above this temperature the Li interstitial hopping plays the dominant role in the superionic behavior of Li_2S.

Therefore, it can be concluded that the temperature-induced disorder in Li_2S results in a superionic phase for the Li conductivity. This finding is interesting from the point of view that knowing the mechanism of superionic diffusion can inspire the researchers to predict and synthesize novel structures which allow for the superionic diffusion of Li ions via the interstitial sites even at low temperatures.

Chapter 5

THEORETICAL STUDY OF c-$Li_7La_3Zr_2O_{12}$/$LiCoO_2$ INTERFACE [1]

5.1 Introduction

It was discussed in section 1.3 that the safety of the Li-ion batteries mainly depends on the electrolyte material. Replacing the conventional liquid electrolyte with a fast ion-conducting solid is a promising way to provide a non-flammable and chemically stable electrolyte in the Li-based batteries. Indeed, by using solid electrolyte, the dendrite fomation is suppressed, and therefore, the metallic Li with high specific capacity can be employed as anode [43, 44, 217]. Moreover, solid electrolytes in Li-S batteries can hinder the migration of the soluble Li-polysulfide from the cathode to the anode and improves the cyclic performance [41, 42].

Lithium garnet oxides as a new class of Li-ion conductors were synthesized by Thangadurai *et al.* in 2003 [49]. These garnet structures with high ionic conductivity and high stability have drawn a lot of attentions in the field of solid electrolytes [51, 52]. As mentioned in section 1.3, one of the promising candidates for solid electrolytes is lithium garnet $Li_7La_3Zr_2O_{12}$ (LLZO), which has Li-ion conductivity of about 10^{-4} S cm^{-1} in its cubic phase at room temperature [62–65]. In addition, metal-doped cubic-LLZO (c-LLZO) has been reported to be stable against Li anode because of its low reduction rate in contact with lithium [60, 66, 218]. These features should give rise to acceptable performance in the LLZO-based batteries. Nevertheless,

---

[1] This chapter is based on the results presented in Ref. [215, 216]

such systems do not possess a high energy density compared to the conventional cells due to a high interfacial resistance at electrolyte/electrode interface [68, 69, 219, 220]. Different experimental studies have investigated this problem specially at the interface between LLZO and a common cathode material, namely $LiCoO_2$ (LCO). LCO is an oxide-based lithium intercalation compound with a layered structure in which Li and Co ions are located on different layers separated by close-packed oxygen planes [221]. The theoretical capacity of LCO has been estimated to be $274\,\mathrm{mA\,h\,g^{-1}}$ [6, 222–224]. The high energy density as well as excellent cyclic performance make LCO a good candidate to be used as cathode [222,225]. Therefore, Li-based batteries with LLZO as the solid electrolyte, LCO as the cathode, and Li as the anode material have attracted lots of interests.

Ohta *et al.* [226] have experimentally observed an increase in interfacial resistance of Nb-doped-LLZO/LCO and Nb-doped-LLZO/Li interfaces compared to $Li_{6.75}La_3Zr_{1.75}Nb_{0.25}O_{12}$ bulk structure. Moreover, Ogumi and co-workers [71] have proposed that low Li transport rate at the interface of LLZO/LCO is not because of a poor contact between LLZO and LCO, but due to a strong interaction between them, leading to the formation of a passivating layer. Using transmission electron microscopy (TEM) and energy-dispersive X-ray diffraction pattern, they have observed a gradual change in the concentrations of Co, La, and Zr across the interface layer during the high-temperature process of LCO coating on LLZO. [71]. In another experimental investigation on the interface of LLZO/LCO, Goodenough *et al.* [72] have confirmed the cation interchange and formation of a diffusion layer during the cathode annealing at high temperatures. They have also proposed a surface modification of LLZO to improve the electrochemical performance at the interface [72].

Few theoretical simulations have been focused on the solid electrolyte/electrode interface. For example, Ohno *et al.* [227] have performed AIMD simulations to investigate Li_3PO_4/$LiFePO_4$ interface. They have reported on Li diffusion from the topmost layer of $LiFePO_4$ to the oxide electrolyte (Li_3PO_4) [227]. According to another theoretical study, high interfacial resistance has been confirmed at sulfide electrolyte and cathode interface [228]. The researchers have observed, via AIMD simulations, that the Li depletion and oxidation occur on the electrolyte side (sulfide side) close to the Li_3PS_4/$LiFePO_4$ interface [228]. In addition using DFT, β-Li_3PS_4/LCO interface has been investigated by Haruyama $et\ al.$ [229]. It has been shown that the Li adsorption at the oxygen sites of LCO results in the formation of space-charge-layer at this interface. Therefore, the $LiNbO_3$ buffer layer has been interposed to suppress this formation [229]. Furthermore, Zhu $et\ al.$ [219] have used *first-principles* calculations to study the thermodynamics of the interface between common solid electrolytes and LCO as cathode. They have proposed the formation of thermodynamically favorable interphase layers with different stabilities at the interface between solid electrolye and electrode [219].

In spite of several experimental investigations on the interface of LLZO/LCO, the atomic and electronic structure of this interface have not been theoretically studied. In this chapter, an ideal interface between LLZO and LCO, namely LLZO(001)/LCO($10\bar{1}4$), is investigated. We apply DFT calculations to study the atomic and electronic structures as well as charge distribution of LLZO surface in vacuum and in contact with the surface of LCO cathode at 0 K. Moreover, the possibility of cation interchange at the LLZO/LCO interface are studied. In addition, we investigate the effect of strain on the ion interchange in bulk models of LLZO and LCO.

5.2 Method of Calculation

To obtain the total energies and the atomic structures at the interface, we perform DFT calculations using mixed Gaussian and plane-wave scheme in CP2K Quickstep [126–129]. In this code, the Kohn-Sham orbitals are expanded in the Gaussian-type basis set, and the auxiliary plane-wave basis set is defined by an energy cutoff, which is 340 Ry in our current calculations. We represent the core electrons by Goedecker-Teter-Hutter pseudopotentials [137] and perform unconstrained diagonalization of the Kohn-Sham (KS) Hamiltonian to consider the spin polarization. Total energies are calculated at the Γ point in a super cell approach. The generalized gradient approximation (GGA) of Perdew, Burke, and Ernzerhof (PBE) [95] is employed, and for Co cations, the Hubbard U parameter is added (DFT+U). As it has been explained in section 2.5.4, within the DFT+U framework, the on-site Coulomb interactions of the localized d or f orbitals are addressed by an added U term. Here, we use the formulation of Dudarev [230] for the on-site Hubbard U. In this method, the on-site coulombic U and exchange term J are combined into an effective potential, $U_{\text{eff}} = U - J$. The DFT+U model is parametrized by comparing the calculated band gap of LCO with the experimental one, and U_{eff} is found to be 5.8 eV giving a band gap of 2.3 eV for LCO. This value lies in the range of experimental band gaps of LCO between 1.7 eV and 2.7 eV [231–234]. In the case of Zr and La, which have only a few electrons in the d orbital ($4d^2$ and $5d^1$ for Zr and La, respectively), the effect of electron correlation is rather small. Therefore, U is not considered in the DFT calculations for Zr and La in LLZO [235–239].

As LLZO has a large unit cell, the constructed slab of LLZO/LCO interface is huge and possesses a lot of electrons leading to demanding DFT calculations. The number of valence electrons considered for Li, O, La, Zr, and Co are respectively 3, 6, 11, 12, and 17. Thus, for our interface model with 544 atoms including 3 types of transition metals (Co, Zr, and La) and totally 3680 electrons, we employ single-zeta (SZV) basis set to make the structural and energy calculations feasible. Later in this chapter, to estimate the effect of strain on cation interchange, we evaluate the energies for bulk structures of LLZO and LCO with and without cation interchange. These calculations for bulk with smaller number of atoms give us the opportunity to use double-zeta basis set with polarization (DZVP).

Furthermore, to study the result of choosing different XC functionals, the hybrid functional of Heyd, Scuseria, and Ernzerhof (HSE06) [103, 104] is employed for the computations on bulk LLZO and bulk LCO. These calculations are carried out using the Vienna Ab initio Simulation Package (VASP) [122–125] and they are compared with the results calculated by PBE+U method implemented in VASP. Projector augmented wave (PAW) are used to treat the core-valence electron interactions, while wave functions are expanded in a plane-wave basis set. For a $1 \times 1 \times 1$ unit cell of bulk LLZO with 192 atoms, Γ-centered $2 \times 2 \times 2$ k-grids and $1 \times 1 \times 1$ k-grids are respectively considered for the PBE+U and HSE06 levels of theory. Similarly, for bulk LCO with $4 \times 4 \times 1$ unit cell (192 atoms), we use Γ-centered $2 \times 2 \times 2$ k-point mesh for the PBE+U method and $1 \times 1 \times 1$ k-point mesh for the HSE06 calculations. The screening and the mixing parameters are respectively $\mu = 0.2$ and $\alpha = 0.25$ in HSE06 method. The convergence criterion for electronic self-consistency is set to 10^{-4} eV, and an energy cutoff of 460 eV is used for the plane-wave basis. Spin polarization is considered in all calcultions.

5.2.1 Initial Structure Optimization

In the crystal structure of LLZO, the Li cations can be coordinated to oxygen tetrahedrally or octahedrally. The difference in the tetragonal and cubic polymorphs of LLZO is the arrangement of Li ions in the tetrahedral and octahedral sites [61, 62]. Using X-ray structure analysis, the three-dimensional pathways for the Li migration in c-LLZO has been proposed by Awaka $et\ al.$ [62]. In this structure, the Li ions are not located on the adjacent Li-allowed sites because of the strong Coulomb repulsion (Fig. 5.1.a) [59, 240]. Such reduced site occupancy is an important factor in high Li-ion conductivity. Considering the mentioned site occupancy, we perform the geometry optimization for the bulk c-LLZO configuration. The model structure consists of 192 atoms and has the stoichiometric formula $Li_{56}La_{24}Zr_{16}O_{96}$. Our calculated unit cell for c-LLZO has a lattice parameter of $a = 12.998$ Å, consistent with the experimental value of 12.968 Å [54] and the previously-reported theoretical value of 12.983 Å [239]. The (001)-oriented surface with a rectangular unit cell is chosen to match with the rectangular LCO($10\bar{1}4$) unit cell which will be introduced later. The LLZO(001) surface is constructed with a two bulk

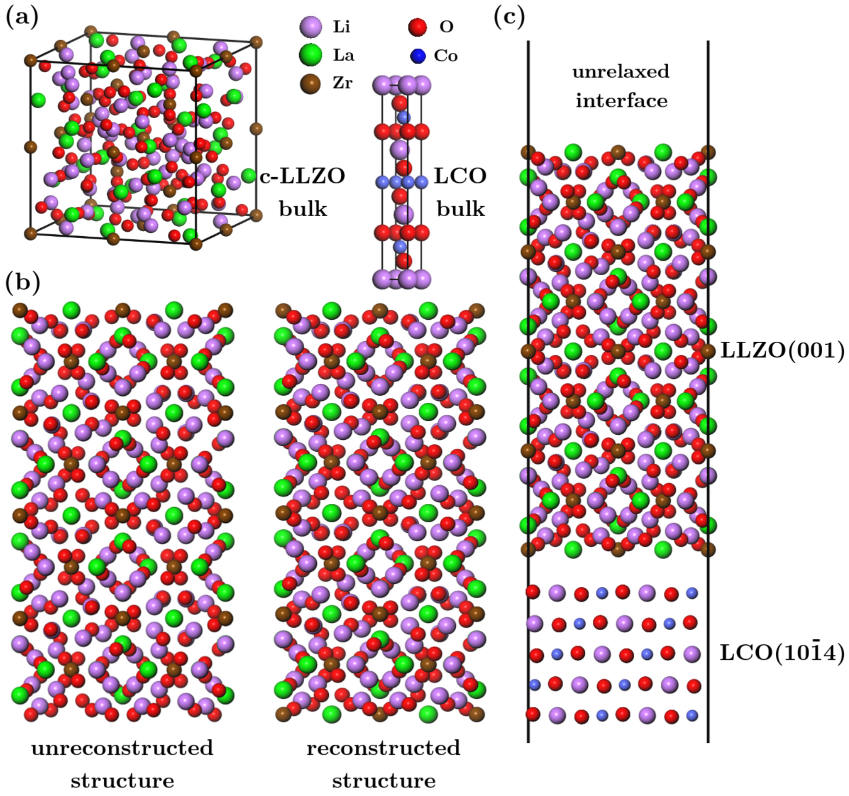

Figure 5.1: (a) Atomic configuration of bulk c-LLZO and LCO in their respective unit cells. (b) Unreconstructed and reconstructed LLZO(001) surface. (c) Interface structure of LLZO(001)/LCO(10$\bar{1}$4).

unit cell thickness containing 384 atoms. The pristine stoichiometric LLZO(001) surface is energetically unfavorable. It has a high dipole moment of 8.3 eÅ which is due to its asymmetric arrangement of the surface atoms. The structure is terminated with different ions at each side (As it is shown in Fig. 5.1.b, four Zr and four La ions are on the topmost layer at one side, while the terminal layer at the other side does not have any Zr or La). The different surface charges or dipoles associate with energy increase and unstability of the surface. Therefore, to stabilize the structure of LLZO(001), we reconstruct a stoicheometric surface by moving two Zr and two La cations from one side to the other side of the slab (see Fig. 5.1.b). This reconstruction is similar to the conventional mechanism in rock salt structures to reduce the surface-dipole problem [241, 242]. The reconstruction decreases the dipole moment to 5.3 eÅ, and the new structure is more stable than the unreconstructed configuration. We find that reducing the polarization play an important role in stability of these structures, and thus, we use the reconstructed LLZO(001) surface to assemble the interface.

In the case of bulk LCO with a rhombohedral structure (Fig. 5.1.a), the lattice parameters are calculated through the geometry optimization as $a = b = 2.862$ Å and $c = 14.045$ Å, which are close to the experimental values of $a = b = 2.819$ Å and $c = 14.09$ Å [243], and the theoretical values of $a = b = 2.829$ Å and $c = 14.119$ Å [244]. Among the low-index facets of LCO, $(10\bar{1}4)$ and (0001) are the most favorable surfaces with the highest stability under a wide range of lithium and oxygen chemical potentials [245, 246]. LCO(0001) surface is polar, while LCO$(10\bar{1}4)$ is a nonpolar surface in which Li layers are distributed from the surface to the bulk region (see Fig. 5.1.c). Thus, in the present study, we use LLZO(001)/LCO$(10\bar{1}4)$ to construct the interface slab. The unrelaxed structure of this interface is shown in Fig. 5.1.c.

To investigate the effect of lattice mismatch between LLZO(001) and LCO$(10\bar{1}4)$, three interface models with different lattice parameters are considered:

(I) $a = b = 12.99$ Å (the theoretical unit cell of LLZO(001))

(II) $a = 12.23$ Å and $b = 12.22$ Å (the averaged unit cell of LLZO(001) and LCO$(10\bar{1}4)$)

(III) $a = 11.46$ Å and $b = 11.45$ Å (the theoretical unit cell of LCO$(10\bar{1}4)$).

The atoms at two bottom layers of LCO$(10\bar{1}4)$ as well as 6.35 Å from the top of LLZO(001) slabs are fixed at their bulk-truncated coordinates. For all the studied interface models, we have first optimized the geometry of LLZO(001) and LCO$(10\bar{1}4)$ surfaces before bringing them in contact with each other. To find a minimum energy interface structure for each model, the following test calculations are performed:

1. The geometry optimization has been carried out for models I–III with a separation of 10 Å between slabs.

2. Afterwards, the relaxed slabs are brought in contact with each other and the geometry relaxation has been performed for fifteen interface structures with separations (along the z direction) of 1.0 Å $\leq z \leq$ 2.4 Å between LLZO(001) and LCO$(10\bar{1}4)$ slabs with the step size of 0.1 Å. An optimal separation of 1.5 Å is then found.

3. Finally, we search for the optimal relative x and y position of the slabs by performing geometry optimization of sixteen structures with different relative x and y coordinates of LLZO(001) slab with respect to LCO($10\bar{1}4$) slab using the optimal separation of 1.5 Å. The vacuum of 15 Å is considered between periodic images along the direction perpendicular to the interface (namely, z direction) for all the structures.

The interaction energy for each structure is evaluated by subtracting the total energy of separated slabs from that of the interface.

In addition, the ionic charges $q(z)$ are calculated by Mulliken population analysis and it is presented along with the charges based on the formal oxidation states. Moreover, the number of electrons and the density of states (DOS) are illustrated for LLZO(001)/LCO($10\bar{1}4$) to have a clear picture of the electronic structure at the interface.

5.3 Results and Discussion

The lowest-energy structures of LLZO(001)/LCO($10\bar{1}4$) interface for each model (I–III) are shown in Fig. 5.2.a. By optimizing the whole interface, it is observed that the atomic structures of the bulk region of LLZO(001) and LCO($10\bar{1}4$) remain bulk-like in models I and II, but not in model III where the unit cell of LCO($10\bar{1}4$) is used. In models I and II, the atoms close to the interface undergo a positional change. Indeed, a Li ion moves from the surface of LCO($10\bar{1}4$) to the surface of LLZO(001) in models I and II while there is no ion segregation from the bulk to the surface. In model III, in which the atomic structure of LLZO(001) becomes disordered, no Li transfer is observed. Moreover, the strongest interaction energy is calculated for model I (-15.19 eV), whereas it is -6.76 eV and -5.74 eV for models II and III, respectively. In order to investigate the interfacial effect, we compare the isolated LLZO(001) and LCO($10\bar{1}4$) features with their characteristics at interface.

Ionic Charge Diagrams: The ionic charge distribution $q(z)$ as a function of z (along the normal to the interface) is calculated using formal oxidation states and Mulliken charge analysis [173] with a mapped column width of ~ 1 Å as a typical size of ions. That is, the charge of each atomic layer with 1 Å width is drawn for each element separately (vertical lines in Fig. 5.2.b and c). Then the sum of these values in each layer ($q(z)$) is plotted along z with black curves. In both analyses of separated surfaces (Fig. 5.2.b and c, left hand side), a sequential chain of dipoles along z direction for LLZO(001) surface has been observed, while for LCO(10$\bar{1}$4), this wave-like pattern is very small in Mulliken analysis and zero in oxidation state plot. By placing the surfaces in contact with each other, the dipole moments at the interfacial layers of the LLZO(001) reduce, whereas they become larger at topmost layers of LCO(10$\bar{1}$4) surface in models I and II. For model III (Fig. 5.2.b and c, right hand side), the change in the charge distribution (i.e. dipole moments) at LLZO(001) part is more substantial than that for the other models. Comparing with the isolated surfaces before the interface constrcution, the change in the charge distribution at LLZO calculated via Mulliken analysis extends to a distance of $\sim$8 Å

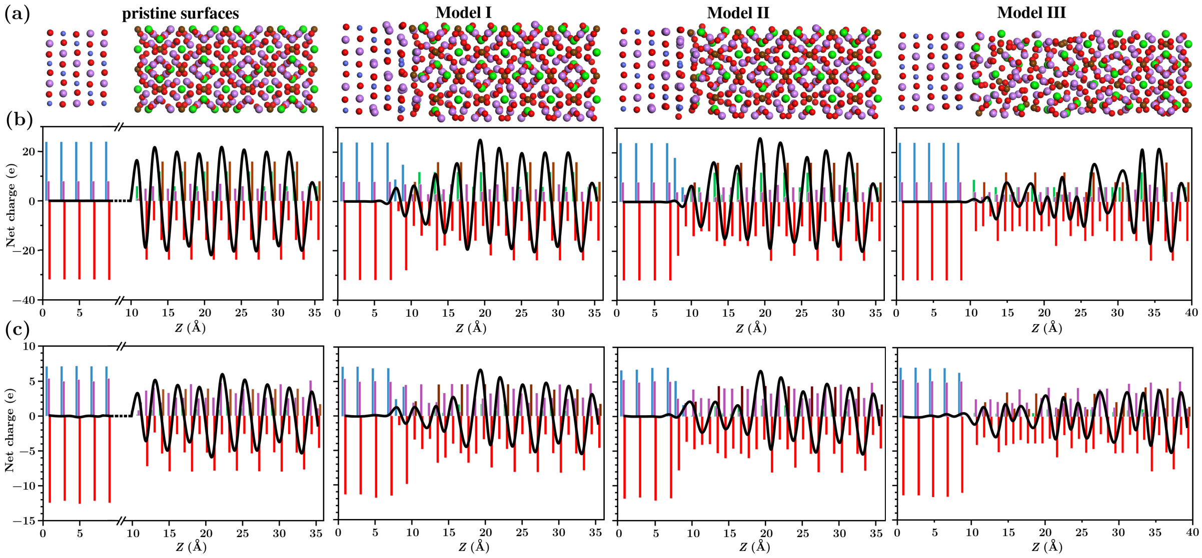

Figure 5.2: (a) Atomic structures for separated surfaces as well as different interface models. Ionic charge diagrams calculated by (b) oxidation state and (c) Mulliken population analysis. In (b) and (c) parts, blue, purple, red, brown, and green lines respectively represent the sum over Co, Li, O, Zr, and La charges in a columnwidth of 1 Å of the slab, and black lines are total sum over all charges in each column ($q(z)$). Included with permission from Jand *et al.* [215] (© Materials Research Society 2018)

from the interface for model I and II, and to $\sim$20 Å above the interface for model III (Fig. 5.2.c). This change for the LCO part is up to $\sim$3 Å in model I and II, and up to $\sim$5 Å in model III. In addition, based on Mulliken analysis, a small electron transfer of 0.48 e and 0.28 e is observed from LCO to LLZO at the interface models I and II, respectively. However, this value is 0.80 e in model III where no ionic transfer between LCO and LLZO occurs.

Number of Electrons: In order to study the electron distribution at the LLZO(001)/LCO(10$\bar{1}$4) interface, we calculate the number of electrons n for each interface model along z. Figure 5.3 shows n as well as the difference in the number of electrons (Δn) between interface and isolated surfaces. It is clear that for LCO(10$\bar{1}$4), there is a considerable change in Δn in all the interface models. Therefore, the induced dipole moments in LCO(10$\bar{1}$4) which is presented in Fig. 5.2 is mainly due to the electronic redistribution, and the ionic displacement has a smaller effect. On the other hand, a small and short range Δn in LLZO(001) illustrates that electron redistribution is not the main factor in weakening of dipoles in LLZO(001) at the interface. This means that the dipole weakening at the topmost layer of LLZO(001) in Fig. 5.2 arises from the ionic displacement.

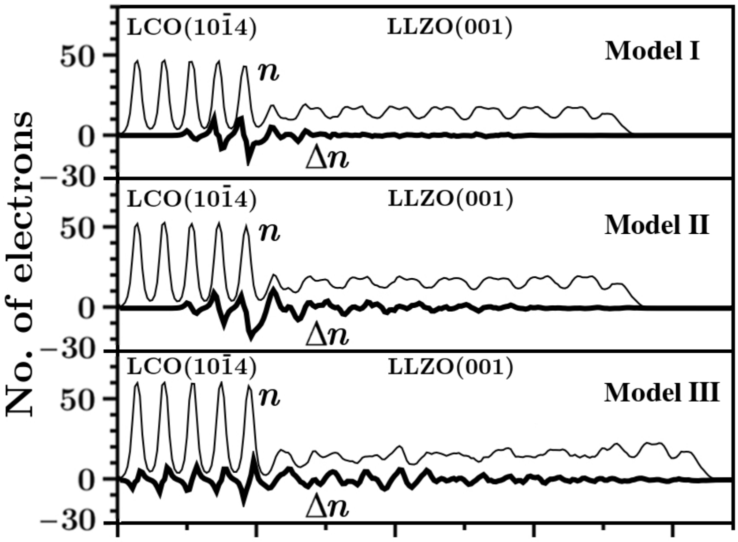

Figure 5.3: Number of electrons (n) for LLZO(001)/LCO(10$\bar{1}$4) interfaces in model I–III, and its difference (Δn) with respect to the separated surfaces.

Electron Density of States: To study the role of each ion in electron transfer at the interface, the electron density of states (DOS) is calculated for LLZO(001)/LCO(10$\bar{1}$4) interface. Figure 5.4 shows the contour map of DOS for the bulk LCO, the bulk LLZO as well as the interface models I–III along the interface normal direction, z. For all the models, the Fermi energy of the whole system is set to zero. From the energy differences between the valence band maximum (VBM) and the conduction band minimum (CBM), the band gaps of the bulk LCO and the bulk LLZO are estimated to be 2.3 eV and 4.1 eV, respectively. At the interface, the formation of gap states is observed in all models. The projected density of states (PDOS) per atom and angular momentum helps us assign these gap states to the certain atomic orbitals.

As illustrated in Fig. 5.4 for model I, the gap states between -0.3 eV and 0.3 eV in LCO(10$\bar{1}$4) are due to the Co$_{3d}$ and O$_{2p}$ orbitals (with more significant role of O$_{2p}$), and those between -1 eV and 0.3 eV in LLZO(001) arise from O$_{2p}$ orbitals. In the interface model I, with the largest biaxial tensile strain for LCO(10$\bar{1}$4) (a =13.4% and b =13.5%), Co cations and O anions accept and also donate electron, depending on their nearby ions at the surface of LLZO(001), and therefore, the Fermi level cuts through the gap states in LCO. On the other hand in LLZO(001), O anions accept and Zr cations donate electron. In addition, the electron/hole transfer is up to 2Å from the interface in LLZO(001) while it is extended to the top three layers of LCO(10$\bar{1}$4), which is around 3Å from the interface.

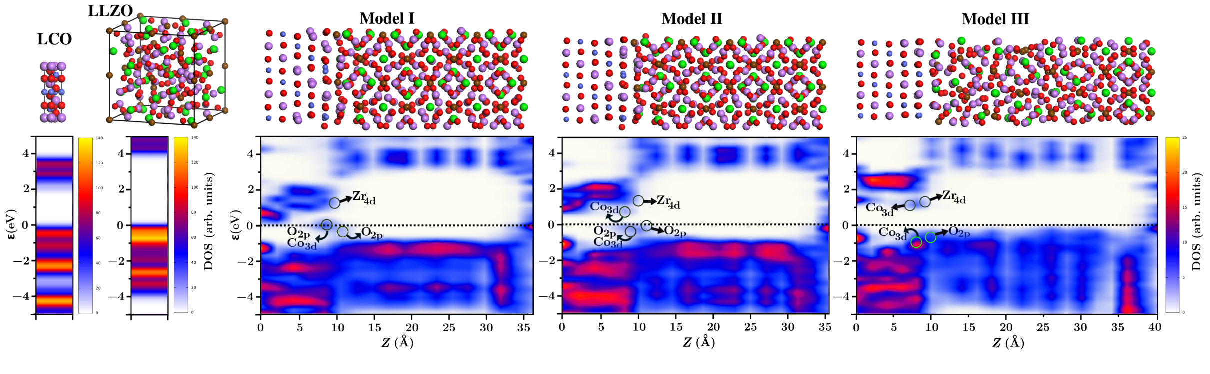

Figure 5.4: Atomic structures and density of states for bulk LCO and bulk LLZO as well as different interface models. Fermi level is set to 0 eV. Included with permission from Jand *et al.* [215] (© Materials Research Society 2018)

Comparing interface models I and II, although structure ordering of LCO($10\bar{1}4$) does not change much with increase in its surface unit cell dimensions, the band gap of LCO($10\bar{1}4$) in model I becomes smaller than that in model II. This is due to the stronger tensile strain in the former one. The smaller band gap in model I results in the larger electron transfer from LCO to LLZO in this case (0.48 e in the model I and 0.28 e in the model II). At the interface model II, the applied tensile strain on LCO($10\bar{1}4$) is a =6.7% and b =6.8%, and the compressive strain on LLZO(001) is a =5.9% and b =6.0%. It is shown that in this model, the empty and occupied states in LCO and LLZO are similar to those in the model I. However, the unoccupied states close to the CBM of LCO($10\bar{1}4$) correspond to Co_{3d} orbitals.

In the model III, where the atoms at LLZO(001) surface undergo a configurational displacement, the largest compressive strain is applied on LLZO while there is no strain on LCO. Similar to the model II, the created empty states close to the CBM of LCO and LLZO are respectively due to Co_{3d} and Zr_{4d}. The created occupied states of Co_{3d} and O_{2p} are merged to the VBM in both surfaces.

5.3.1 Possibility of Li accumulation at the Interface

The concentration of Li at the interface is a key factor in Li-ion conductivity of the system as Li is the major charge carrier. Li depletion at a region near the interface can lead to a lower ionic conductivity and as a result, a lower energy density in Li-based batteries. To study the possibilty of Li accumulation in our system, we move two Li ions from $z = 26.8$ Å (middle) to $z = 14.7$ Å (topmost layers) within the LLZO(001) slab. Focusing on the interface model II in which a moderate strain is imposed on both LLZO and LCO surfaces, eight different configurations are constructed by removing/locating Li ions from/at different sites. Four of these structures are energetically more favorable than the pristine interface with the energy difference between 0.33 eV and 1.38 eV. Note that during the geometry optimization for pristine interface in model II, a Li ion goes from the surface of LCO($10\bar{1}4$) to LLZO(001). By moving two Li ions from bulk-like region of LLZO to the interface region and performing the geometry relaxation, one Li occupies the Li-vacancy site at the surface of LCO($10\bar{1}4$), and another Li ion goes to an interstitial site at LLZO(001) close to an oxygen anion of the LCO($10\bar{1}4$) surface.

Similarly, we move two Li ions from the top of LCO to the top of LLZO(001) slab at the interface in model II. Among four different possible configurations, the most stable structure is found to be $0.3\,\mathrm{eV}$ more favorable than the pristine interface while the others are unstable compared to the pristine structure. It is observed that in this stable configuration, the Li vacancy site at LCO($10\bar{1}4$) is spontaneously occupied by one of the moved Li ions to the top of LLZO(001). Indeed, this Li ion comes back to the LCO surface during the geometry optimization. However, the other Li does not significantly move and forms a ionic bond with oxygen anion of LCO($10\bar{1}4$). Therefore, it is concluded that the accumulation of Li ions at the interface is energetically favorable.

Moreover, the similar investigation is carried out for O ions at LLZO(001) and LCO($10\bar{1}4$) to study O accumulation at the interface. Six different configurations are tested by moving O from the bulk region of LLZO to the interface as well as from the inner layers of LCO to its topmost layer. None of these structures are more stable than the pristine interface.

5.3.2 Possibility of Cation Interchange

As mentioned earlier in the current chapter, two experimental research groups have reported on cross diffusions of Co from LCO to LLZO and, concurrently La and Zr from LLZO to LCO during the high-temperature coating of LCO on LLZO [71, 72]. Therefore, we theoretically study the possibility of cation interchange at LLZO(001)/LCO($10\bar{1}4$) interface. We start with considering interchange of a Co cation from the topmost layer of LCO($10\bar{1}4$) with a Zr or a La cation in LLZO(001) at different distances from the contact plane. The interaction energy versus the z coordinate of replaced cation site in LLZO(001) is plotted in Fig. 5.5. Because of a similarity between the interface models I and II in terms of electronic and atomic structure, we first investigate the models I and III. In all plots, the first point at the left side indicates the energy of the pristine structure without any cation interchange. In both models I and III, the required energy to interchange the cations at the structure (hereafter called interchange energy) is positive for most of the z values, which shows that the structures with cation interchange are more unfavorable than the pristine interface. However, energy variation in the case of Co↔Zr is smaller than that of Co↔La. This is because of the large size of La ion (with ionic radius of 117.2 pm) compared to Co (ionic radius of 68.5 pm) and Zr cation (ionic radius of 86.0 pm). Then, the history dependence of cation transport along the interface normal direction is checked by considering the geometrically-optimized structure with cation interchange at $z - \Delta z$ as an initial structure for interchange at z. The results do not indicate any significant change in the interchange energies.

Furthermore, to check the possibility of the cation diffusion in model II, we calculate the interchange energies of the structure with Co↔Zr or Co↔La at $z = 27.5\,\text{Å}$, which are also obtained to be positive (1.68 eV for Co↔Zr and 2.03 eV for Co↔La). Afterwards, the dependence of interchange energy on the z coordinate of the Co cation at LCO(10$\bar{1}$4) is studied in this

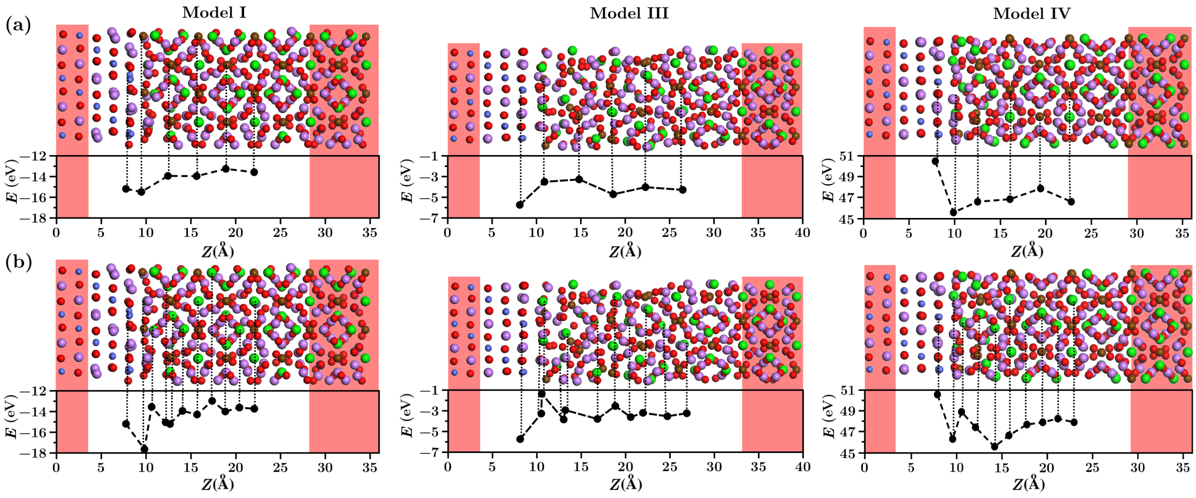

Figure 5.5: Atomic structure as well as interaction energy diagram versus z for cation interchange process for interface models I and III and new-labelled IV. Co is interchanged with (a) Zr and (b) La at the interface.

model. Thus, we evaluate the energies of interfaces with interchange of a Zr or a La cation at $z = 27.5\,\text{Å}$ with Co from the second and third topmost layers of LCO(10$\bar{1}$4). The energy values show that the pristine structure is still more favorable. The interchange energies for Co$\leftrightarrow$Zr considering Co from the second and third layer of LCO are $1.53\,$eV and $2.14\,$eV, respectively. The corresponding energies for Co$\leftrightarrow$La are $2.27\,$eV and $1.86\,$eV, respectively.

Note that in our study, we optimize the geometry of both surfaces before bringing them in contact with each other to construct the interface models. After constructing the interface, the relaxation is again performed for the whole structure. The other common approach is to construct the interface by placing the bulk-truncated surfaces close to each other without pre-optimization. However, as will be shown in the following, this approach for complex surfaces such as LLZO(001) with large lattice mismatches can lead to a very different result compared to that of models I-III. Figure 5.5 illustrates the interchange energies for an interface model (labeled as model IV) with the size of the theoretical unit cell of LCO(10$\bar{1}$4), similar to that of model III. The difference between model III and model IV is that in the latter case we do not optimize the geometry of surfaces before bringing them in contact with each other. After the geometry optimization of the interface model IV, the resulting configuration is not similar to the minimum energy structure found for model III in which LLZO(001) slab is disordered. At the interface model IV, there is a large stress along the normal to the interface plane. In this case, interaction energy is highly positive since total energies of the separated LLZO(001) and LCO(10$\bar{1}$4) surfaces are much lower than that of the interface which is frozen in a metastable structure. Nevertheless, the calculated interchange energies in this model have negative values, indicating the possibility of the cation interchange under large stress along the interface normal direction z. Therefore, cation diffusion at LLZO/LCO interface can occur under special conditions. This is in agreement with previous experimental findings which report on the cation interchange at LLZO/LCO interface during annealing process at a high temperature [71, 72].

In the models I and III where the unit cell size is kept fixed before and after interchange, cation diffusion can cause a strain in the slabs. As strain has a fundamental influence on the possibility of cation interchange, in the following we study the effect of interchange-induced strain.

5.3.3 Effects of Interchange-Induced Strain and Computational Parameters on Cation Interchange

In order to minimize the strain resulting from the cation interchange between LLZO and LCO, we consider the bulk models of LLZO and LCO and perform a full (geometry and unit cell) optimization for bulk structures with an interchanged cation. For the bulk structures, to be consistent with the concentration of interchanged cations in the interface models, we interchange a Co with a Zr or a La per $1 \times 1 \times 1$ unit cell of LLZO and a Zr or a La with a Co cation per $4 \times 4 \times 1$ unit cell of LCO. The volume of each optimized supercell is calculated, and the percentage of the volume change with respect to the corresponding pristine structure is evaluated to determine the effect of cation interchange on the unit cell size. The calculated volume change is rather small (less than 2% in LLZO or LCO). However, the results indicate that the Co↔Zr or Co↔La interchange in LLZO shrinks its unit cell dimensions, while both interchanges in LCO expand its unit cell. This arises from the fact that Co cation is smaller than Zr and La ions. The interchange energy (E_{intc}) for this system is obtained by

$$E_{\mathrm{intc}} = E^{\mathrm{LLZO}}_{\mathrm{A}\leftrightarrow\mathrm{B}} + E^{\mathrm{LCO}}_{\mathrm{A}\leftrightarrow\mathrm{B}} - E^{\mathrm{LLZO}}_{\mathrm{pris}} - E^{\mathrm{LCO}}_{\mathrm{pris}}, \tag{5.3.1}$$

where $E_{\mathrm{A}\leftrightarrow\mathrm{B}}$ and E_{pris} are respectively the energies of the structure with $\mathrm{A} \leftrightarrow \mathrm{B}$ interchange and pristine structure. We obtain the interchange energies of $+1.30\,\mathrm{eV}$ and $+2.59\,\mathrm{eV}$ for Co↔Zr and Co↔La interchanges, respectively. Thus, the cation interchange is energetically unfavorable in both cases.

As mentioned before, because of the large size of the interface structure ($152\,\mathrm{Li}$, $272\,\mathrm{O}$, $40\,\mathrm{Co}$, $48\,\mathrm{La}$, and $32\,\mathrm{Zr}$), using a double-zeta basis set is computationally prohibitive. Therefore, we employ single-zeta (SZV) basis set to evaluate the atomic and electronic structures of the interface models. Here, for the bulk structures with smaller number of atoms, we have the possibilty to use a double-zeta basis set. Therefore, to study the effect of basis set on the results, we recalculate the energies of bulk LLZO and bulk LCO with and without ion interchange using double-zeta basis set with polarization (DZVP). By using DZVP, the volume changes based on cation interchange are again less than 2% in LLZO or LCO and completely consistent with the previous results, i.e. both interchanges make the unit cell of LLZO smaller, while they increase the size of LCO unit cell. In addition, the interchange energies are evaluated to be $+4.09$ eV and $+5.73$ eV for Co↔Zr and Co↔La interchanges respectively. Therefore, both SZV and DZVP basis sets predict unfavorable structures after the ion interchange.

Furthermore, the effect of different XC functionals on our calculations is studied by employing two different levels of theory: DFT+U method by using PBE XC functional and the hybrid functional of Heyd, Scuseria, and Ernzerhof (HSE06). Hereafter, we use the plane-wave basis set implemented in VASP. The calculated band gaps of the bulk LLZO and LCO as well as their experimental band gaps are presented in Tab. 5.1. The on-site Hubbard U model is parametrized in VASP with $U_{\text{eff}} = 4.9$ eV for Co atom, obtained by a fit to the experimental band gap of LCO. As it was discussed before, because of the relatively small electron correlation effects in Zr and La atoms, Hubbard U is not considered in LLZO. The results show that in case of LLZO, the calculated band gap using HSE06 is larger than the one obtained by PBE and it is in good agreement with experimental measurements. However, in LCO the calculations based on HSE06 do not yield different results from the PBE+U method, and both are consistent with the experimental values.

Table 5.1: Calculated and experimental band gaps of LLZO and LCO.

	PBE+U	HSE06	experiment
LLZO	4.1*	5.4	5.0 – 5.5 [54, 247]
LCO	2.3	2.3	1.7 – 2.7 [231–234]

* In case of LLZO, U is not considered for La and Zr atoms due to their small electron correlation.

By allowing the unit cell and atomic positions to change during the full system relaxation, we try to obtain the strain-free configurations for LLZO and LCO with and without cation interchange. Then, the interchange energies for Co$\leftrightarrow$Zr and Co$\leftrightarrow$La are evaluated through Eq. 5.3.1 to be respectively $+1.37\,$eV and $+2.89\,$eV using PBE+U functional, while they are $+5.23\,$eV and $+6.48\,$eV in the HSE06 framework. Therefore, similar to PBE results, the calculations at the HSE06 level of theory also indicate that at the strain-free systems, the cation diffusion between LLZO and LCO is infeasible.

5.4 Conclusions

In this chapter, *first-principles* calculations have been performed to study the interface between two promising materials in ASSLBs, namely LLZO as an electrolyte and LCO as a cathode. These materials have been rarely investigated theoretically because of their complicated structures.

We have modelled the LLZO(001)/LCO(10$\bar{1}$4) interface by considering different unit cell sizes and thereby, various biaxial compressive and tensile strains. It has been found that under a high biaxial tensile strain, LCO(10$\bar{1}$4) surface keeps its crystalline structure, while a large biaxial compressive strain on LLZO(001) leads to large displacement of atoms in this surface. On the other hand, most of the ions in both LLZO(001) and LCO(10$\bar{1}$4) surfaces remain at their bulk atomic positions under moderate strains. During ionic relaxation for the interface models where LLZO(001) stays crystalline, we have observed the Li migration and the electron transfer from LCO to LLZO at the interface. Although the effect of the ion transfer is neutralized by the electron redistribution to some degree, it is not completely compensated and results in a dipole formation at the interface.

We have also studied the accumulation possibility of more Li ions at the interface by transferring Li ions from deep layers of LLZO(001) to its topmost layers. The calculated energies for this process indicate its feasibility. During geometry optimization, the transferred Li ions at the interface move slightly and bind to oxygen anion of LCO($10\bar{1}4$) which shows the effect of an electrostatic driving force.

In the next step, we have investigated the possibility of cation interchange at LLZO/LCO interfaces. It has been found that the ion interchange can only occur if there is a huge stress along the interface normal direction. In other cases, where this stress is released by optimizing the surfaces before bringing them in contact with each other, we have calculated the positive energies for Co↔Zr and Co↔La interchanges indicating that the cation diffusion is unfavorable. In such systems, the interchange energies are generally lower close to the interface.

Afterwards, the bulk models of LLZO and LCO have been considered, and in order to minimize the strain, full cell geometry optimizations have been performed on these systems with and without interchange. We have also studied the difference between employing SZV and DZVP basis sets. Also in separate calculations, the correlation effects have been investigated by using PBE+U and HSE functionals. All these calculations show that ion interchange at the interface is unlikely. Our study indicates that the low ionic conductivity, which impacts the performance of ASSLBs, can be the result of a new phase forming at the interface. This interfacial phase have been observed previously [71,72], but the composition and the structure of this new phase is still heavily under debate.

A natural extension of the current study would be to investigate possible stable phases produced due to the interaction between LLZO and LCO. Moreover, the effect of the types of interchanged species could be studied. The approach presented in this chapter can be used to model the solid/solid interfaces in various applications. In addition, the charge distribution and the density of states analyses give valuable information on atomic scale processes at the interface. Our calculations on cation diffusion clarify the conditions under which the cation interchange is possible. These findings can help experimentalists to control the cation diffusion at the interface. In general, our computational results suggest a useful perspective for the further improvement of next-generation batteries.

Chapter 6

SUMMARY

Recently, lithium(Li)-based batteries have attracted significant attention due to their applications in electric vehicles and many new kinds of portable electronic devices such as cell phones. However, such batteries still need more research and improvement in order to meet the market demands for low cost and high-rate performance. Lithium-sulfur (Li-S) batteries with their high theoretical energy density, and all-solid-state Li-ion batteries (ASSLB) with their increased safety and design flexibility are among the most promising energy-storage systems. The focus of current dissertation is set on the important materials in these two kinds of batteries.

The common cathode materials for Li-S batteries are S_8 or Li_2S. Intermediate Li-polysulfides are also formed at the cathode during the charge/discharge process. Moreover, carbon-based materials are added to sulfur cathodes in order to increase their electronic conductivity. In Li-S batteries, the Li-polysulfides migrate through the electrolyte, and their reductions and oxidations on both electrodes result in excessive utilization of the active material and self discharging. To inhibit this process, traping of Li-polysulfides in the cathode has been proposed. Here, we have investigated the ability of graphene (pristine and defective) as part of sulfur cathode to trap the Li-polysulfides. To this end, binding energies and Gibbs free energies for adsorption process of Li_2S_x onto the graphene are calculated using Density Functional Theory (DFT) with PBE-D2 method. To calculate the Gibbs free energies, vibrational and configurational entropies are evaluated. It is found that the interaction of the Li-polysulfides and graphene is mostly dominated by the dispersion interactions, and pristine as well as defective graphene cannot immobilize the Li-polysulfides. Although during the adsorption of Li_2S_x on monovacant graphene, one S atom is chemically attached to the defect site, the resulting S-doped graphene cannot hinder the Li-polysulfide migration either. In the next step, Li_2S, which is one of the promising cathode materials in Li-S batteries, has been investigated. Similar to S_8, Li_2S has a low electronic conductivity. Moreover, Li-ion conductivity of Li_2S at room temperature is low, but this crystal possesses a high ionic conductivity at high temperatures. Although many experiments have been performed to study the ionic conductivity of Li_2S, it has not been studied theoretically so far. In this thesis, we have studied ionic conductivity of Li_2S as well as the origin of its superionic phase transition which has been reported by experimentalists. To achieve this aim, we have applied DFT and *ab initio* molecular dynamics (AIMD). Through AIMD simulations at different temperatures, diffusion coefficients are evaluated. Additionally, concentration of the Li ions is calculated from thermodynamics of defects as well as using the detailed balance condition. Finally, the Li-ion conductivity is obtained for various temperatures which shows the superionic phase transition for temperatures above $T = 900K$, in good agreement with the experimental reports.

In the case of ASSLBs, although the solid electrolyte has a high ionic conductivity and a high stability, such systems do not possess a high energy density compared to the conventional cells, which is due to a large interfacial resistance at electrolyte/electrode interface. Therefore, it is of crucial importance to know the atomic and electronic structures of these interfaces. In this work, an important electrolyte/cathode interface for ASSLBs, namely $Li_7La_3Zr_2O_{12}/LiCoO_2$, has been investigated. Although several experimental researches have synthesized and studied this interface, its complex structure makes it difficult to investigate theoretically. Here, for the first time, we have modelled and studied this interface using DFT (PBE+U method) by focusing on $Li_7La_3Zr_2O_{12}(001)/LiCoO_2(10\bar{1}4)$. To consider the effect of lattice mismatch between the two surfaces, three models with different lattice parameters for the interface have been applied. Therefore, different magnitudes of biaxial compressive and tensile strains are applied on the interface. It is shown that during the interface optimization, a Li ion moves from the surface of $LiCoO_2$ to $Li_7La_3Zr_2O_{12}$. This ion migration is accompanied by electron transfer in the same direction attempting to neutralize the system. The electron transfer also results in the formation of certain gap states at the interface. In the next step, the possibility of cation interchange (Co↔Zr or Co↔La) has been studied at the $Li_7La_3Zr_2O_{12}(001)/LiCoO_2(10\bar{1}4)$ interface. By calculating the energy difference between interface with interchanged cations and pristine interface, it is found that this process is possible only under a large stress along the interface normal direction. In addition, to minimize the strain on such systems during the cation interchange, the bulk models of $Li_7La_3Zr_2O_{12}$ and $LiCoO_2$ have been considered, and the full optimization has been carried out for these bulk structures. Moreover, to increase the accuracy, HSE06 hybrid functional has been applied. Comparing with pristine $Li_7La_3Zr_2O_{12}$ and $LiCoO_2$ bulks, the structures with Co↔Zr or Co↔La cation interchange are unfavorable. As a result, these structures can only form under a large stress which is consistent with experimental observations, showing the cation interchange during the cathode annealing at high temperatures.

In the case of Li-S batteries, our findings show that pristine and even vacant graphene in sulfur cathode do not have the ability to catch the Li polysulfides. Therefore, another way to trap the Li-polysulfides should be proposed. According to the experimental results, doping of graphene by certain dopants such as nitrogen or phosphorus can immobilize the Li_2S_x molecules, and improve the performance of sulfur cathode. This process should be studied theoretically in detail, similar to what we have done for pristine and defective graphene. In order to study the Li-ion conductivity, the approach that has been used in Li_2S can be applied to model superionic phase transition in ionic crystals. In addition, at $Li_7La_3Zr_2O_{12}(001)/LiCoO_2(10\bar{1}4)$ interface, our calculations enable us to have a better understanding of processes at such interfaces which will eventually lead to fabricate the more efficient ASSLB.

Chapter 7

ZUSAMMENFASSUNG

In jüngster Zeit haben Lithium (Li)-basierte Batterien aufgrund ihrer Anwendungen in Elektrofahrzeugen und vielen neuen Arten von tragbaren elektronischen Geräten (z. B. Mobiltelefonen), beträchtliche Aufmerksamkeit auf sich gezogen. Solche Batterien müssen jedoch noch weiter verbessert werden, um den Marktanforderungen nach niedrigen Kosten und hoher Leistung gerecht zu werden. Deshalb werden Lithium-Schwefel (Li-S) Batterien infolge ihrer hohen theoretischen Energiedichte und Festkörper-Li-Ionen-Batterien (FLIB) aufgrund ihrer Sicherheit und Designflexibilität intensiv erforscht, und sie gelten als die vielversprechendsten Energiespeichersysteme. Der Schwerpunkt der vorliegenden Dissertation liegt auf den wichtigen Materialien dieser beiden Batterietypen.

Die üblichen Kathodenmaterialien in Li-S Batterien sind S_8 oder Li_2S. Während des Lade- / Entladeprozesses werden auch intermediäre Li-Polysulfide an der Kathode gebildet. Darüber hinaus werden kohlenstoffbasierte Materialien der Schwefelkathode hinzugefügt, um ihre elektronische Leitfähigkeit zu erhöhen. In Li-S Batterien führen Reduktionen und Oxidationen der Li-Polysulfide, die aufgrund ihrer Wanderung durch die Elektrolyten auftreten, zu einer übermäßigen Ausnutzung des aktiven Materials und zu einer Selbstentladung. Um diesen Prozess zu hemmen, wurde das Abfangen von Li-Polysulfiden in der Kathode vorgeschlagen. In dieser Arbeit wird die Fähigkeit des Graphen (makellos und defekt) untersucht, welches Teil der Schwefelkathode ist, die Li-Polysulfide einzufangen. Zu diesem Zweck werden Bindungsenergien und freie Gibbs-Energien für den Adsorptionsprozess von Li_2S_x auf Graphen mithilfe der Dichtefunktionaltheorie (DFT) mit der PBE-D2-Methode berechnet. Zur Berechnung der freien Gibbs-Energien werden Vibrations- und Konfigurationsentropien ausgewertet. Es zeigt sich, dass die Wechselwirkung von Li-Polysulfiden und Graphen hauptsächlich durch die Dispersionswechselwirkungen dominiert wird, und makelloses oder defektes Graphen kann die Li-Polysulfide nicht immobilisieren. Obwohl während der Adsorption von Li_2S_x an Monovacant-Graphen ein S-Atom vom Molekül chemisch an die Defektstelle gebunden wird, kann auch das resultierende S-dotierte Graphen die Li-Polysulfid-Wanderung nicht verhindern. Im nächsten Schritt wurde Li_2S, eines der vielversprechenden Kathodenmaterialien in Li-S Batterien, untersucht. Ähnlich verhält sich Li_2S zu S_8, die eine niedrige elektronische Leitfähigkeit haben. Darüber hinaus ist die Li-Ionen-Leitfähigkeit von Li_2S bei Raumtemperatur niedrig, aber dieser Kristall besitzt eine hohe Ionenleitfähigkeit bei hohen Temperaturen. Obwohl viele Experimente durchgeführt wurden, um die Ionenleitfähigkeit von Li_2S zu untersuchen, wurde sie bisher nicht theoretisch untersucht. In dieser Arbeit haben wir die Ionenleitfähigkeit von Li_2S sowie den Grund für dessen superionischen Phasenübergang untersucht, der von Experimentatoren berichtet wurde. Um dieses Ziel zu erreichen, haben wir DFT und *ab initio*- Molekulardynamik (AIMD) angewendet. Durch AIMD-Simulationen bei verschiedenen Temperaturen werden Diffusionskoeffizienten ausgewertet. Zusätzlich wird die Konzentration der Li-Ionen aus der Thermodynamik von Defekten sowie unter Verwendung der detaillierten Gleichgewichtsbedingung berechnet. Die Li-Ionen-Leitfähigkeit wird bei verschiedenen Temperaturen simuliert und zeigt folglich den superionischen Phasenübergang für Temperaturen über $T = 900K$. Dies steht in guter Übereinstimmung mit den experimentellen Ergebnissen.

Obwohl der Festelektrolyt in FLIBen eine hohe Ionenleitfähigkeit und eine hohe Stabilität aufweist, besitzen FLIBen keine hohe Energiedichte im Vergleich zu herkömmlichen Zellen. Dies liegt an einem großen Grenzflächenwiderstand an der Elektrolyt/Elektroden -Schnittstelle. Daher ist es von entscheidender Bedeutung, die atomaren und elektronischen Strukturen dieser Grenzflächen zu kennen. In dieser Arbeit wurde eine wichtige Elektrolyt/Katoden -Grenzfläche für FLIBen, $Li_7La_3Zr_2O_{12}$/$LiCoO_2$, untersucht. Obwohl mehrere experimentelle Forschungen diese Grenzfläche synthetisiert und untersucht haben, erschwert ihre komplexe Struktur die theoretische Untersuchung. Hier wurde das erste Mal diese Schnittstelle mit DFT (PBE+U Methode) modelliert und untersucht, indem wir uns auf $Li_7La_3Zr_2O_{12}(001)$/$LiCoO_2(10\bar{1}4)$ konzentriert haben. Um den Effekt der Gitterfehlanpassung zwischen den zwei Oberflächen zu berücksichtigen, werden drei Modelle mit unterschiedlichen Gitterparametern für die Grenzfläche verwendet. Daher werden unterschiedliche Größen biaxialer Druck- und Zugspannungen auf die Grenzfläche angewendet. Es wurde gezeigt, dass sich während der Grenzflächenoptimierung ein Li-Ion von der $LiCoO_2$ Oberfläche zu $Li_7La_3Zr_2O_{12}$ bewegt. Diese Ionenwanderung wird von einem Elektronentransfer in der gleichen Richtung begleitet, der versucht, das System zu neutralisieren. Daher werden bestimmte Bandlückenzustände an der Schnittstelle gebildet. Im nächsten Schritt wurde die Möglichkeit des Kationenaustauschs (Co↔Zr oder Co↔La) an der $Li_7La_3Zr_2O_{12}(001)$/$LiCoO_2(10\bar{1}4)$-Schnittstelle untersucht. Durch Berechnen der Energiedifferenz zwischen der Grenzfläche mit ausgetauschten Kationen und der ursprünglichen Grenzfläche wurde herausgefunden, dass dieser Prozess nur unter einer großen Spannung entlang der Grenzflächennormalrichtung möglich ist. Im nächsten Schritt wurden die Volumenmodelle von $Li_7La_3Zr_2O_{12}$ und $LiCoO_2$ betrachtet. Um die Belastung solcher Systeme während des Kationenaustauschs zu minimieren, wurde die vollständige Optimierung durchgeführt. Für die Erhöhung der Genauigkeit wurde HSE06-Hybridfunktional angewendet. Im Vergleich zu reinen $Li_7La_3Zr_2O_{12}$ und $LiCoO_2$ sind die Strukturen mit Co↔Zr oder Co↔La-Kationenaustausch ungünstig. Folglich können sich diese Strukturen mit dem Kationenaustausch nur unter großen Spannungen bilden, die bisher experimentell bei der Behandlung von Kathoden mit hohen Temperaturen, dem Kathodenglühen, nachgewiesen werden konnten.

Im Fall von Li-S-Batterien zeigen unsere Ergebnisse, dass ein reines oder sogar defektes Graphen in der Schwefelkathode nicht in der Lage ist, die Li-Polysulfide einzufangen. Daher sollte ein anderer Weg zum Einfangen der Li-Polysulfide gesucht werden. Gemäß den experimentellen

Ergebnissen kann die Dotierung von Graphen mit bestimmten Dotierstoffen wie Stickstoff oder Phosphor die $\mathrm{Li_2S}_x$-Moleküle immobilisieren und die Leistung der Schwefelkathode verbessern. Dieser Prozess sollte theoretisch genau untersucht werden, ähnlich wie wir es für ein reines oder defektes Graphen getan haben. Der Ansatz, der in $\mathrm{Li_2S}$ verwendet wurde, kann hier ebenfalls angewendet werden, um die Li-Ionen-Leitfähigkeit zu untersuchen sowie die temperaturinduzierten superionischen Phasenübergänge in ionischen Kristallen zu modellieren. Darüber hinaus ermöglichen unsere Berechnungen an der $\mathrm{Li_7La_3Zr_2O_{12}}(001)$/$\mathrm{LiCoO_2}(10\bar{1}4)$-Schnittstelle ein besseres Verständnis der Prozesse an solchen Grenzflächen, die letztendlich zu effizienteren Festkörperbatterien führen werden.

List of Publications

Main Publications

M1 - S. Panahian Jand, Y.X. Chen, P. Kaghazchi
"Comparative Theoretical Study of Adsorption of Lithium Polysulfides (Li_2S_x) on Pristine and Defective Graphene"
J. Power Sources, **308**, 166 (2016)
DOI: 10.1016/j.jpowsour.2016.01.062

M2 - S. Panahian Jand, Q. Zhang, P. Kaghazchi
"Theoretical Study of Superionic Phase Transition in Li_2S"
Sci. Rep., **7**, 5873 (2017)
DOI: 10.1038/s41598-017-05775-2

M3 - S. Panahian Jand, P. Kaghazchi
"Theoretical Study of cubic-$Li_7La_3Zr_2O_{12}$(001)/$LiCoO_2$($10\bar{1}4$) Interface"
MRS Commun., **8**, 591 (2018)
DOI: 10.1557/mrc.2018.33

Other Publications

O1 - S. Panahian Jand, P. Kaghazchi
"The Role of Electrostatic Effects in Determining the Structure of LiF-graphene Interfaces"
J. Phys.: Condens. Matter, **26**, 262001 (2014)
DOI: 10.1088/0953-8984/26/26/262001

O2 - C. Lentz, S. Panahian Jand, J. Melke, C. Roth, P. Kaghazchi
"DRIFTS Study of CO Adsorption on Pt Nanoparticles Supported by DFT Calculations"
J. Mol. Catal. A Chem., **426**, (2016)
DOI: 10.1016/j.molcata.2016.10.002

O3 - P. Partovi-Azar, S. Panahian Jand, P. Kaghazchi
"Electronic, Magnetic, and Transport Properties of Polyacrylonitrile-Based Carbon Nanofibers of Various Widths"
Phys. Rev. Appl., **9**, 014012 (2018)
DOI: 10.1103/PhysRevApplied.9.014012

Bibliography

[1] Yoshio, M., Brodd, R. J. & Kozawa, A. *Lithium-ion batteries*, vol. 1 (Springer, 2009).

[2] Atkins, P. *Shriver and Atkins' inorganic chemistry* (Oxford University Press, USA, 2010).

[3] Goodenough, J., Abruna, H. & Buchanan, M. Basic research needs for electrical energy storage. report of the basic energy sciences workshop on electrical energy storage, April 2–4, 2007. Tech. Rep., DOESC (USDOE Office of Science (SC)) (2007).

[4] Choi, N.-S. *et al.* Challenges facing lithium batteries and electrical double-layer capacitors. *Angewandte Chemie International Edition* **51**, 9994–10024 (2012).

[5] Ji, X., Lee, K. T. & Nazar, L. F. A highly ordered nanostructured carbon-sulphur cathode for lithium-sulphur batteries. *Nature Materials* **8**, 500 (2009).

[6] Mizushima, K., Jones, P., Wiseman, P. & Goodenough, J. B. Li_xCoO_2 (0<x<-1): A new cathode material for batteries of high energy density. *Materials Research Bulletin* **15**, 783–789 (1980).

[7] Linden, D. & Reddy, T. B. Handbook of batteries. 3rd (2002).

[8] Fong, R., Von Sacken, U. & Dahn, J. R. Studies of lithium intercalation into carbons using nonaqueous electrochemical cells. *Journal of The Electrochemical Society* **137**, 2009–2013 (1990).

[9] Peled, E. & Menkin, S. Sei: Past, present and future. *Journal of The Electrochemical Society* **164**, A1703–A1719 (2017).

[10] Abraham, K., Jiang, Z. & Carroll, B. Highly conductive PEO-like polymer electrolytes. *Chemistry of Materials* **9**, 1978–1988 (1997).

[11] Xu, K. Nonaqueous liquid electrolytes for lithium-based rechargeable batteries. *Chemical Reviews* **104**, 4303–4418 (2004).

[12] Shin, J. H. & Cairns, E. J. N-methyl-(n-butyl) pyrrolidinium bis (trifluoromethanesulfonyl) imide-LiTFSI–poly (ethylene glycol) dimethyl ether mixture as a Li/S cell electrolyte. *Journal of Power Sources* **177**, 537–545 (2008).

[13] Zhang, S. S. Liquid electrolyte lithium/sulfur battery: fundamental chemistry, problems, and solutions. *Journal of Power Sources* **231**, 153–162 (2013).

[14] Zheng, S. *et al.* High performance C/S composite cathodes with conventional carbonate-based electrolytes in Li–S battery. *Scientific Reports* **4** (2014).

[15] Xu, R., Lu, J. & Amine, K. Progress in mechanistic understanding and characterization techniques of Li–S batteries. *Advanced Energy Materials* **5** (2015).

[16] Younesi, R., Veith, G. M., Johansson, P., Edström, K. & Vegge, T. Lithium salts for advanced lithium batteries: Li–metal, Li–O_2, and Li–S. *Energy & Environmental Science* **8**, 1905–1922 (2015).

[17] Umebayashi, Y. *et al.* Lithium ion solvation in room-temperature ionic liquids involving bis(trifluoromethanesulfonyl)imide anion studied by raman spectroscopy and DFT calculations. *Journal of Physical Chemistry B* **111**, 13028–13032 (2007).

[18] Wang, L. *et al.* A quantum–chemical study on the discharge reaction mechanism of lithium–sulfur batteries. *Journal of Energy Chemistry* **22**, 72–77 (2013).

[19] Wang, Z. *et al.* Enhancing lithium–sulphur battery performance by strongly binding the discharge products on amino-functionalized reduced graphene oxide. *Nature Communications* **5**, 5002 (2014).

[20] Das, S. *et al.* All-solid-state lithium-sulfur battery based on a nanoconfined libh4 electrolyte. *Journal of The Electrochemical Society* **163**, A2029–A2034 (2016).

[21] Marmorstein, D. *et al.* Electrochemical performance of lithium/sulfur cells with three different polymer electrolytes. *Journal of Power Sources* **89**, 219–226 (2000).

[22] Jeddi, K., Ghaznavi, M. & Chen, P. A novel polymer electrolyte to improve the cycle life of high performance lithium–sulfur batteries. *Journal of Materials Chemistry A* **1**, 2769–2772 (2013).

[23] Nagao, M., Hayashi, A. & Tatsumisago, M. Sulfur–carbon composite electrode for all-solid-state Li/S battery with Li_2S–P_2S_5 solid electrolyte. *Electrochimica Acta* **56**, 6055–6059 (2011).

[24] Nagao, M., Hayashi, A. & Tatsumisago, M. Bulk-type lithium metal secondary battery with indium thin layer at interface between Li electrode and Li_2S-P_2S_5 solid electrolyte. *Electrochemistry* **80**, 734–736 (2012).

[25] Ogawa, M., Kanda, R., Yoshida, K., Uemura, T. & Harada, K. High-capacity thin film lithium batteries with sulfide solid electrolytes. *Journal of Power Sources* **205**, 487–490 (2012).

[26] Sakuda, A., Hayashi, A., Ohtomo, T., Hama, S. & Tatsumisago, M. Bulk-type all-solid-state lithium secondary battery with Li_2S-P_2S_5 thin-film separator. *Electrochemistry* **80**, 839–841 (2012).

[27] Peled, E., Gorenshtein, A., Segal, M. & Sternberg, Y. Rechargeable lithium sulfur battery. *Journal of Power Sources* **26**, 269–271 (1989).

[28] Choi, Y.-J. *et al.* Effects of carbon coating on the electrochemical properties of sulfur cathode for lithium/sulfur cell. *Journal of Power Sources* **184**, 548–552 (2008).

[29] Niu, J. J., Wang, J. N., Jiang, Y., Su, L. F. & Ma, J. An approach to carbon nanotubes with high surface area and large pore volume. *Microporous and Mesoporous Materials* **100**, 1–5 (2007).

[30] Ji, L. *et al.* Porous carbon nanofiber–sulfur composite electrodes for lithium/sulfur cells. *Energy & Environmental Science* **4**, 5053–5059 (2011).

[31] Zheng, G., Yang, Y., Cha, J. J., Hong, S. S. & Cui, Y. Hollow carbon nanofiber-encapsulated sulfur cathodes for high specific capacity rechargeable lithium batteries. *Nano Letters* **11**, 4462–4467 (2011).

[32] Hoffmann, C. *et al.* Nanocasting hierarchical carbide-derived carbons in nanostructured opal assemblies for high-performance cathodes in lithium–sulfur batteries. *ACS Nano* **8**, 12130–12140 (2014).

[33] Wang, B., Alhassan, S. M. & Pantelides, S. T. Formation of large polysulfide complexes during the lithium–sulfur battery discharge. *Physical Review Applied* **2**, 034004 (2014).

[34] Liu, Q. *et al.* Insight on lithium polysulfide intermediates in a Li–S battery by density functional theory. *RSC Advances* **7**, 33373–33377 (2017).

[35] Yang, Y. *et al.* New nanostructured Li_2S/silicon rechargeable battery with high specific energy. *Nano Letters* **10**, 1486–1491 (2010).

[36] Jha, H., Buchberger, I., Cui, X., Meini, S. & Gasteiger, H. A. Li–S batteries with Li_2S cathodes and Si/C anodes. *Journal of The Electrochemical Society* **162**, A1829–A1835 (2015).

[37] Suo, L. *et al.* Carbon cage encapsulating nano-cluster Li_2S by ionic liquid polymerization and pyrolysis for high performance Li–S batteries. *Nano Energy* **13**, 467–473 (2015).

[38] Zhang, S. *et al.* A high energy density Li_2S@C nanocomposite cathode with a nitrogen-doped carbon nanotube top current collector. *Journal of Materials Chemistry A* **3**, 18913–18919 (2015).

[39] Buehrer, W. *et al.* Lattice dynamics and the diffuse phase transition of lithium sulphide investigated by coherent neutron scattering. *Journal of Physics: Condensed Matter* **3**, 1055 (1991).

[40] Altorfer, F. *et al.* Lithium diffusion in the superionic conductor Li_2S. *Physica B: Condensed Matter* **180**, 795–797 (1992).

[41] Hassoun, J. & Scrosati, B. Moving to a solid–state configuration: A valid approach to making lithium–sulfur batteries viable for practical applications. *Advanced Materials* **22**, 5198–5201 (2010).

[42] Zhong, H., Wang, C., Xu, Z., Ding, F. & Liu, X. A novel quasi–solid state electrolyte with highly effective polysulfide diffusion inhibition for lithium–sulfur batteries. *Scientific Reports* **6**, 25484 (2016).

[43] Masquelier, C. Solid electrolytes: Lithium ions on the fast track. *Nature Materials* **10**, 649 (2011).

[44] Tarascon, J.-M. & Armand, M. Issues and challenges facing rechargeable lithium batteries. *Nature* **414**, 359–367 (2001).

[45] Yang, K.-Y., Fung, K.-Z. & Leu, C. Study on the structural change and lithium ion conductivity for the perovskite-type $LaAlO_3$–$La_{0.5}Li_{0.5}TiO_3$ solid solution. *Journal of Alloys and Compounds* **438**, 207–216 (2007).

[46] Bohnke, O. The fast lithium-ion conducting oxides $Li_3xLa_2/3 - xTiO_3$ from fundamentals to application. *Solid State Ionics* **179**, 9–15 (2008).

[47] Ribes, M., Barrau, B. & Souquet, J. Sulfide glasses: Glass forming region, structure and ionic conduction of glasses in Na_2S–SiS_2, Na_2S–P_2S_5 and Li_2S–GeS_2 systems. *Journal of Non-Crystalline Solids* **38**, 271–276 (1980).

[48] Minami, T., Hayashi, A. & Tatsumisago, M. Recent progress of glass and glass-ceramics as solid electrolytes for lithium secondary batteries. *Solid State Ionics* **177**, 2715–2720 (2006).

[49] Thangadurai, V., Kaack, H. & Weppner, W. J. Novel fast lithium ion conduction in garnet-type $Li_5La_3M_2O_{12}$ (M= Nb, Ta). *Journal of the American Ceramic Society* **86**, 437–440 (2003).

[50] Thangadurai, V., Schwenzel, J. & Weppner, W. Tailoring ceramics for specific applications: a case study of the development of all–solid–state lithium batteries. *Ionics* **11**, 11–23 (2005).

[51] Thangadurai, V. & Weppner, W. $Li_6ALa_2Ta_2O_{12}$ (A = Sr, Ba): Novel garnet-like oxides for fast lithium ion conduction. *Advanced Functional Materials* **15**, 107–112 (2005).

[52] Thangadurai, V. & Weppner, W. $Li_6ALa_2Nb_2O_{12}$ (A = Ca, Sr, Ba): A new class of fast lithium ion conductors with garnet-like structure. *Journal of the American Ceramic Society* **88**, 411–418 (2005).

[53] Percival, J. & Slater, P. Identification of the Li sites in the Li ion conductor, $Li_6SrLa_2Nb_2O_12$, through neutron powder diffraction studies. *Solid State Communications* **142**, 355–357 (2007).

[54] Murugan, R., Thangadurai, V. & Weppner, W. Fast lithium ion conduction in garnet-type $Li_7La_3Zr_2O_{12}$. *Angewandte Chemie International Edition* **46**, 7778–7781 (2007).

[55] Murugan, R., Thangadurai, V. & Weppner, W. Effect of lithium ion content on the lithium ion conductivity of the garnet-like structure $Li_{5+x}BaLa_2Ta_2O_{11.5+0.5x}$ (x = 0–2). *Applied Physics A: Materials Science & Processing* **91**, 615–620 (2008).

[56] Cussen, E. J. Structure and ionic conductivity in lithium garnets. *Journal of Materials Chemistry* **20**, 5167–5173 (2010).

[57] Han, J. *et al.* Experimental visualization of lithium conduction pathways in garnet-type $Li_7La_3Zr_2O_{12}$. *Chemical Communications* **48**, 9840–9842 (2012).

[58] Geiger, C. A. *et al.* Crystal chemistry and stability of $Li_7La_3Zr_2O_{12}$ garnet: a fast lithium-ion conductor. *Inorganic Chemistry* **50**, 1089–1097 (2010).

[59] Xie, H., Alonso, J. A., Li, Y., Fernandez-Diaz, M. T. & Goodenough, J. B. Lithium distribution in aluminum-free cubic $Li_7La_3Zr_2O_{12}$. *Chemistry of Materials* **23**, 3587–3589 (2011).

[60] Buschmann, H. *et al.* Structure and dynamics of the fast lithium ion conductor $Li_7La_3Zr_2O_{12}$. *Physical Chemistry Chemical Physics* **13**, 19378–19392 (2011).

[61] Awaka, J., Kijima, N., Hayakawa, H. & Akimoto, J. Synthesis and structure analysis of tetragonal $Li_7La_3Zr_2O_{12}$ with the garnet-related type structure. *Journal of Solid State Chemistry* **182**, 2046–2052 (2009).

[62] Awaka, J. *et al.* Crystal structure of fast lithium-ion-conducting cubic $Li_7La_3Zr_2O_{12}$. *Chemistry Letters* **40**, 60–62 (2010).

[63] Shimonishi, Y. *et al.* Synthesis of garnet-type $Li_{7-x}La_3Zr_2O_{12-1/2x}$ and its stability in aqueous solutions. *Solid State Ionics* **183**, 48–53 (2011).

[64] Murugan, R., Ramakumar, S. & Janani, N. High conductive yttrium doped $Li_7La_3Zr_2O_{12}$ cubic lithium garnet. *Electrochemistry Communications* **13**, 1373–1375 (2011).

[65] Wang, Y. & Lai, W. High ionic conductivity lithium garnet oxides of $Li_{7-x}La_3Zr_{2-x}Ta_xO_{12}$ compositions. *Electrochemical and Solid-State Letters* **15**, A68–A71 (2012).

[66] El Shinawi, H. & Janek, J. Stabilization of cubic lithium-stuffed garnets of the type $Li_7La_3Zr_2O_{12}$ by addition of gallium. *Journal of Power Sources* **225**, 13–19 (2013).

[67] Takada, K. Progress and prospective of solid-state lithium batteries. *Acta Materialia* **61**, 759–770 (2013).

[68] Ren, Y., Liu, T., Shen, Y., Lin, Y. & Nan, C.-W. Chemical compatibility between garnet-like solid state electrolyte $Li_{6.75}La_3Zr_{1.75}Ta_{0.25}O_{12}$ and major commercial lithium battery cathode materials. *Journal of Materiomics* **2**, 256–264 (2016).

[69] Takada, K. *et al.* Interfacial modification for high-power solid-state lithium batteries. *Solid State Ionics* **179**, 1333–1337 (2008).

[70] Sakuda, A., Hayashi, A. & Tatsumisago, M. Interfacial observation between $LiCoO_2$ electrode and Li_2S-Li_2S_5 solid electrolytes of all-solid-state lithium secondary batteries using transmission electron microscopy. *Chemistry of Materials* **22**, 949–956 (2009).

[71] Kim, K. H. *et al.* Characterization of the interface between Li_xCoO_2 and $Li_7La_3Zr_2O_{12}$ in an all-solid-state rechargeable lithium battery. *Journal of Power Sources* **196**, 764–767 (2011).

[72] Park, K. *et al.* Electrochemical nature of the cathode interface for a solid-state lithium-ion battery: Interface between $LiCoO_2$ and garnet-$Li_7La_3Zr_2O_{12}$. *Chemistry of Materials* **28**, 8051–8059 (2016).

[73] Ma, C. *et al.* Interfacial stability of Li metal–solid electrolyte elucidated via in situ electron microscopy. *Nano letters* **16**, 7030–7036 (2016).

[74] Sharafi, A. *et al.* Impact of air exposure and surface chemistry on Li–$Li_7La_3Zr_2O_{12}$ interfacial resistance. *Journal of Materials Chemistry A* (2017).

[75] Sharafi, A. *et al.* Surface chemistry mechanism of ultra–low interfacial resistance in the solid–state electrolyte $Li_7La_3Zr_2O_{12}$. *Chemistry of Materials* **29**, 7961–7968 (2017).

[76] Levine, I. *Quantum chemistry* (Allyn Bacon, New York, USA, 2000).

[77] Gasiorowicz, S. *Quantum physics* (John Wiley & Sons, 2007).

[78] Sakurai, J. J. & Commins, E. D. Modern quantum mechanics, revised edition (1995).

[79] Zettili, N. Quantum mechanics: concepts and applications (2003).

[80] Heisenberg, W. Über quantentheoretische umdeutung kinematischer und mechanischer beziehungen. *Zeitschrift für Physik* **33**, 879–893 (1925).

[81] Schrödinger, E. Quantisierung als eigenwertproblem. *Annalen der Physik* **385**, 437–490 (1926).

[82] Born, M. & Oppenheimer, R. Zur quantentheorie der molekeln. *Annalen der Physik* **389**, 457–484 (1927).

[83] Hartree, D. R. The wave mechanics of an atom with a non-coulomb central field. part I. theory and methods. In *Mathematical Proceedings of the Cambridge Philosophical Society*, vol. 24, 89–110 (Cambridge University Press, 1928).

[84] Fock, V. Näherungsmethode zur lösung des quantenmechanischen mehrkörperproblems. *Zeitschrift für Physik A Hadrons and Nuclei* **61**, 126–148 (1930).

[85] Hartree, D. & Hartree, W. Self-consistent field, with exchange, for beryllium. *Proceedings of the Royal Society of London. Series A, Mathematical and Physical Sciences* **150**, 9–33 (1935).

[86] Slater, J. C. The theory of complex spectra. *Physical Review* **34**, 1293 (1929).

[87] Szabo, A. & Ostlund, N. S. *Modern quantum chemistry: introduction to advanced electronic structure theory* (Courier Corporation, 2012).

[88] Thomas, L. H. The calculation of atomic fields. In *Mathematical Proceedings of the Cambridge Philosophical Society*, vol. 23, 542–548 (Cambridge University Press, 1927).

[89] Fermi, E. Eine statistische methode zur bestimmung einiger eigenschaften des atoms und ihre anwendung auf die theorie des periodischen systems der elemente. *Zeitschrift für Physik* **48**, 73–79 (1928).

[90] Dirac, P. A. Note on exchange phenomena in the thomas atom. In *Mathematical Proceedings of the Cambridge Philosophical Society*, vol. 26, 376–385 (Cambridge University Press, 1930).

[91] Hohenberg, P. & Kohn, W. Inhomogeneous electron gas. *Physical Review* **136**, B864 (1964).

[92] Kohn, W. & Sham, L. J. Self-consistent equations including exchange and correlation effects. *Physical Review* **140**, A1133 (1965).

[93] Ceperley, D. M. & Alder, B. Ground state of the electron gas by a stochastic method. *Physical Review Letters* **45**, 566 (1980).

[94] Perdew, J. P. *et al.* Atoms, molecules, solids, and surfaces: Applications of the generalized gradient approximation for exchange and correlation. *Physical Review B* **46**, 6671 (1992).

[95] Perdew, J. P., Burke, K. & Ernzerhof, M. Generalized gradient approximation made simple. *Physical Review Letters* **77**, 3865 (1996).

[96] Hammer, B., Hansen, L. B. & Nørskov, J. K. Improved adsorption energetics within density-functional theory using revised Perdew–Burke–Ernzerhof functionals. *Physical Review B* **59**, 7413 (1999).

[97] Adamo, C. & Barone, V. Physically motivated density functionals with improved performances: The modified Perdew–Burke–Ernzerhof model. *Journal of Chemical Physics* **116**, 5933–5940 (2002).

[98] Tao, J., Perdew, J. P., Staroverov, V. N. & Scuseria, G. E. Climbing the density functional ladder: Nonempirical meta–generalized gradient approximation designed for molecules and solids. *Physical Review Letters* **91**, 146401 (2003).

[99] Perdew, J. P. & Zunger, A. Self-interaction correction to density-functional approximations for many-electron systems. *Physical Review B* **23**, 5048 (1981).

[100] Hubbard, J. Electron correlations in narrow energy bands. In *Proceedings of the Royal Society of London A: Mathematical, Physical and Engineering Sciences*, vol. 276, 238–257 (The Royal Society, 1963).

[101] Hubbard, J. Electron correlations in narrow energy bands. II. the degenerate band case. In *Proceedings of the Royal Society of London A: Mathematical, Physical and Engineering Sciences*, vol. 277, 237–259 (The Royal Society, 1964).

[102] Hubbard, J. Electron correlations in narrow energy bands. III. an improved solution. In *Proceedings of the Royal Society of London A: Mathematical, Physical and Engineering Sciences*, vol. 281, 401–419 (The Royal Society, 1964).

[103] Heyd, J., Scuseria, G. E. & Ernzerhof, M. Hybrid functionals based on a screened coulomb potential. *Journal of Chemical Physics* **118**, 8207–8215 (2003).

[104] Krukau, A. V., Vydrov, O. A., Izmaylov, A. F. & Scuseria, G. E. Influence of the exchange screening parameter on the performance of screened hybrid functionals. *Journal of Chemical Physics* **125**, 224106 (2006).

[105] Grimme, S. Semiempirical GGA-type density functional constructed with a long-range dispersion correction. *Journal of Computational Chemistry* **27**, 1787–1799 (2006).

[106] Grimme, S., Antony, J., Ehrlich, S. & Krieg, H. A consistent and accurate ab initio parametrization of density functional dispersion correction (DFT-D) for the 94 elements H-Pu. *Journal of Chemical Physics* **132**, 154104 (2010).

[107] Grimme, S. Accurate description of van der Waals complexes by density functional theory including empirical corrections. *Journal of Computational Chemistry* **25**, 1463–1473 (2004).

[108] Ashcroft, N. W., Mermin, N. D. & Rodriguez, S. Solid state physics (1998).

[109] Monkhorst, H. J. & Pack, J. D. Special points for brillouin-zone integrations. *Physical Review B* **13**, 5188 (1976).

[110] Payne, M. C., Teter, M. P., Allan, D. C., Arias, T. & Joannopoulos, J. Iterative minimization techniques for ab initio total-energy calculations: molecular dynamics and conjugate gradients. *Reviews of modern physics* **64**, 1045 (1992).

[111] Frenking, G. *et al.* Pseudopotential calculations of transition metal compounds: Scope and limitations. *Reviews in Computational Chemistry. Edited by KB Lipkowitz and DB Boyd, VCH Publishers, Inc., Deerfield Beach, USA* **8**, 63–144 (1996).

[112] Cundari, T. R., Benson, M. T., Lutz, M. L. & Sommerer, S. O. Effective core potential approaches to the chemistry of the heavier elements. *Reviews in Computational Chemistry, Volume 8* 145–202 (1996).

[113] Marder, M. P. *Condensed Matter Physics* (John Wiley & Sons, 2010).

[114] Jensen, F. Introduction to computational chemistry. *Editorial Offices October* (1999).

[115] Kohn, W. Density functional and density matrix method scaling linearly with the number of atoms. *Physical Review Letters* **76**, 3168 (1996).

[116] Koch, W. & Holthausen, M. C. *A chemist's guide to density functional theory* (John Wiley & Sons, 2015).

[117] Preuss, H. Bemerkungen zum self-consistent-field-verfahren und zur methode der konfigurationenwechselwirkung in der quantenchemie. *Zeitschrift für Naturforschung A* **11**, 823–831 (1956).

[118] Van Duijneveldt, F. B., van Duijneveldt-van de Rijdt, J. G. & van Lenthe, J. H. State of the art in counterpoise theory. *Chemical Reviews* **94**, 1873–1885 (1994).

[119] Boys, S. F. & Bernardi, F. d. The calculation of small molecular interactions by the differences of separate total energies. some procedures with reduced errors. *Molecular Physics* **19**, 553–566 (1970).

[120] Schultz, P. A. Local electrostatic moments and periodic boundary conditions. *Physical Review B* **60**, 1551 (1999).

[121] Mattsson, A. E., Schultz, P. A., Desjarlais, M. P., Mattsson, T. R. & Leung, K. Designing meaningful density functional theory calculations in materials sciencea primer. *Modelling and Simulation in Materials Science and Engineering* **13**, R1 (2004).

[122] Kresse, G. & Hafner, J. Ab initio molecular dynamics for open-shell transition metals. *Physical Review B* **48**, 13115 (1993).

[123] Kresse, G. & Furthmüller, J. Efficiency of ab-initio total energy calculations for metals and semiconductors using a plane-wave basis set. *Computational Materials Science* **6**, 15–50 (1996).

[124] Kresse, G. & Furthmüller, J. Efficient iterative schemes for ab initio total-energy calculations using a plane-wave basis set. *Physical Review B* **54**, 11169 (1996).

[125] Kresse, G. & Joubert, D. From ultrasoft pseudopotentials to the projector augmented-wave method. *Physical Review B* **59**, 1758 (1999).

[126] Lippert, G., Hutter, J. & Parrinello, M. A hybrid gaussian and plane wave density functional scheme. *Molecular Physics* **92**, 477–488 (1997).

[127] Lippert, G., Hutter, J. & Parrinello, M. The gaussian and augmented-plane-wave density functional method for ab initio molecular dynamics simulations. *Theoretical Chemistry Accounts (Theoretica Chimica Acta)* **103**, 124–140 (1999).

[128] VandeVondele, J. & Hutter, J. An efficient orbital transformation method for electronic structure calculations. *Journal of Chemical Physics* **118**, 4365–4369 (2003).

[129] VandeVondele, J. *et al.* Quickstep: Fast and accurate density functional calculations using a mixed gaussian and plane waves approach. *Computer Physics Communications* **167**, 103–128 (2005).

[130] Phillips, J. C. Energy-band interpolation scheme based on a pseudopotential. *Physical Review* **112**, 685 (1958).

[131] Heine, V. The pseudopotential concept. *Solid State Physics* **24**, 1–36 (1970).

[132] Cohen, M. L. Pseudopotentials and total energy calculations. *Physica Scripta* **1982**, 5 (1982).

[133] Starkloff, T. & Joannopoulos, J. Local pseudopotential theory for transition metals. *Physical Review B* **16**, 5212 (1977).

[134] Hamann, D., Schlüter, M. & Chiang, C. Norm-conserving pseudopotentials. *Physical Review Letters* **43**, 1494 (1979).

[135] Bachelet, G., Hamann, D. & Schlüter, M. Pseudopotentials that work: From H to Pu. *Physical Review B* **26**, 4199 (1982).

[136] Troullier, N. & Martins, J. L. Efficient pseudopotentials for plane-wave calculations. *Physical Review B* **43**, 1993 (1991).

[137] Goedecker, S., Teter, M. & Hutter, J. Separable dual-space gaussian pseudopotentials. *Physical Review B* **54**, 1703 (1996).

[138] Yu, Y. B., Privalov, P. L. & Hodges, R. S. Contribution of translational and rotational motions to molecular association in aqueous solution. *Biophysical Journal* **81**, 1632–1642 (2001).

[139] Glasstone, S. *Textbook of Physical Chemistry* (Macmillan, 1951).

[140] Ryde, U. A fundamental view of enthalpy–entropy compensation. *Med. Chem. Comm.* **5**, 1324–1336 (2014).

[141] McQuarrie, D. A. *Statistical thermodynamics* (Harper and Row, 1973).

[142] Groß, A. Theoretical surface science: A microscopic perspective (2007).

[143] McQuarrie, D. & Simon, J. Chemical kinetics I: Rate laws. *Physical Chemistry: A Molecular Approach* 1165–1169 (1997).

[144] Bechstedt, F. *Principles of surface physics* (Springer Science & Business Media, 2012).

[145] Rapaport, D. C., Blumberg, R. L., McKay, S. R., Christian, W. *et al.* The art of molecular dynamics simulation. *Computers in Physics* **10**, 456–456 (1996).

[146] Tuckerman, M. *Statistical mechanics: theory and molecular simulation* (Oxford University Press, 2010).

[147] Marx, D. & Hutter, J. *Ab initio molecular dynamics: basic theory and advanced methods* (Cambridge University Press, 2009).

[148] Verlet, L. Computer “experiments” on classical fluids. i. thermodynamical properties of Lennard-Jones molecules. *Physical Review* **159**, 98 (1967).

[149] Swope, W. C., Andersen, H. C., Berens, P. H. & Wilson, K. R. A computer simulation method for the calculation of equilibrium constants for the formation of physical clusters of molecules: Application to small water clusters. *Journal of Chemical Physics* **76**, 637–649 (1982).

[150] Nosé, S. A molecular dynamics method for simulations in the canonical ensemble. *Molecular physics* **52**, 255–268 (1984).

[151] Nosé, S. A unified formulation of the constant temperature molecular dynamics methods. *Journal of Chemical Physics* **81**, 511–519 (1984).

[152] Hoover, W. G. Canonical dynamics: equilibrium phase-space distributions. *Physical Review A* **31**, 1695 (1985).

[153] Sharma, M., Donadio, D., Schwegler, E. & Galli, G. Probing properties of water under confinement: Infrared spectra. *Nano letters* **8**, 2959–2962 (2008).

[154] Wan, Q., Spanu, L., Galli, G. A. & Gygi, F. Raman spectra of liquid water from ab initio molecular dynamics: vibrational signatures of charge fluctuations in the hydrogen bond network. *Journal of Chemical Theory and Computation* **9**, 4124–4130 (2013).

[155] Hellmann, H. *Hans Hellmann: Einführung in Die Quantenchemie: Mit Biografischen Notizen von Hans Hellmann Jr.* (Springer-Verlag, 2015).

[156] Feynman, R. P. Forces in molecules. *Physical Review* **56**, 340 (1939).

[157] Martin, R. M. *Electronic structure: basic theory and practical methods* (Cambridge university press, 2004).

[158] Jand, S. P., Chen, Y. & Kaghazchi, P. Comparative theoretical study of adsorption of lithium polysulfides (Li_2S_x) on pristine and defective graphene. *Journal of Power Sources* **308**, 166–171 (2016).

[159] Yamin, H., Gorenshtein, A., Penciner, J., Sternberg, Y. & Peled, E. Lithium sulfur battery oxidation/reduction mechanisms of polysulfides in THF solutions. *Journal of the Electrochemical Society* **135**, 1045–1048 (1988).

[160] Becke, A. D. Density-functional exchange-energy approximation with correct asymptotic behavior. *Physical Review A* **38**, 3098 (1988).

[161] Lee, C., Yang, W. & Parr, R. G. Development of the Colle-Salvetti correlation-energy formula into a functional of the electron density. *Physical Review B* **37**, 785 (1988).

[162] Becke, A. D. Beckes three parameter hybrid method using the LYP correlation functional. *Journal of Chemical Physics* **98**, 5648–5652 (1993).

[163] Wang, H. *et al.* Graphene-wrapped sulfur particles as a rechargeable lithium–sulfur battery cathode material with high capacity and cycling stability. *Nano Letters* **11**, 2644–2647 (2011).

[164] Evers, S. & Nazar, L. F. Graphene-enveloped sulfur in a one pot reaction: a cathode with good coulombic efficiency and high practical sulfur content. *Chemical Communications* **48**, 1233–1235 (2012).

[165] Wang, J., Yang, J., Xie, J., Xu, N. & Li, Y. Sulfur–carbon nano-composite as cathode for rechargeable lithium battery based on gel electrolyte. *Electrochemistry Communications* **4**, 499–502 (2002).

[166] Wang, J. *et al.* Polymer lithium cells with sulfur composites as cathode materials. *Electrochimica Acta* **48**, 1861–1867 (2003).

[167] Liang, C., Dudney, N. J. & Howe, J. Y. Hierarchically structured sulfur/carbon nanocomposite material for high-energy lithium battery. *Chemistry of Materials* **21**, 4724–4730 (2009).

[168] Liu, F. *et al.* Reduced graphene oxide encapsulated sulfur spheres for the lithium-sulfur battery cathode. *Results in Physics* **7**, 250–255 (2017).

[169] Yao, X. *et al.* High-performance all-solid-state lithium–sulfur batteries enabled by amorphous sulfur-coated reduced graphene oxide cathodes. *Advanced Energy Materials* (2017).

[170] Partovi-Azar, P., Nafari, N. & Tabar, M. R. R. Interplay between geometrical structure and electronic properties in rippled free-standing graphene. *Physical Review B* **83**, 165434 (2011).

[171] Ahlrichs, R., Bär, M., Häser, M., Horn, H. & Kölmel, C. Electronic structure calculations on workstation computers: The program system turbomole. *Chemical Physics Letters* **162**, 165–169 (1989).

[172] Turbomole-V6. A development of University of Karlsruhe and Forschungszentrum Karlsruhe GmbH, 1989–2007, TURBOMOLE GmbH since 2007. *see also: http://www.turbomole.com* (2010).

[173] Mulliken, R. S. Electronic population analysis on LCAO–MO molecular wave functions. I. *Journal of Chemical Physics* **23**, 1833–1840 (1955).

[174] Ma, J., Alfe, D., Michaelides, A. & Wang, E. Stone-wales defects in graphene and other planar sp^2-bonded materials. *Physical Review B* **80**, 033407 (2009).

[175] Lusk, M. T. & Carr, L. D. Nanoengineering defect structures on graphene. *Physical Review Letters* **100**, 175503 (2008).

[176] Zhang, H. *et al.* Diffusion and coalescence of vacancies and interstitials in graphite: A first-principles study. *Diamond and Related Materials* **19**, 1240–1244 (2010).

[177] Thrower, P. & Mayer, R. Point defects and self-diffusion in graphite. *Physica Status Solidi (A)* **47**, 11–37 (1978).

[178] Carlsson, J. M. & Scheffler, M. Structural, electronic, and chemical properties of nanoporous carbon. *Physical Review Letters* **96**, 046806 (2006).

[179] Han, K. *et al.* Free-standing nitrogen-doped graphene paper as electrodes for high-performance lithium/dissolved polysulfide batteries. *Chem. Sus. Chem.* **7**, 2545–2553 (2014).

[180] Gu, X. *et al.* A porous nitrogen and phosphorous dual doped graphene blocking layer for high performance Li–S batteries. *Journal of Materials Chemistry A* **3**, 16670–16678 (2015).

[181] Jand, S. P., Zhang, Q. & Kaghazchi, P. Theoretical study of superionic phase transition in Li_2S. *Scientific Reports* **7**, 5873 (2017).

[182] Gao, W. & Sammes, N. M. *An introduction to electronic and ionic materials* (World Scientific Publishing Company, 1999).

[183] Bruce, P. G. Solid-state chemistry of lithium power sources. *Chemical Communications* 1817–1824 (1997).

[184] Minh, N. Q. Ceramic fuel cells. *Journal of the American Ceramic Society* **76**, 563–588 (1993).

[185] Bonanos, N., Knight, K. & Ellis, B. Perovskite solid electrolytes: structure, transport properties and fuel cell applications. *Solid State Ionics* **79**, 161–170 (1995).

[186] Carrette, L., Friedrich, K. A. & Stimming, U. Fuel cells: principles, types, fuels, and applications. *Chem. Phys. Chem.* **1**, 162–193 (2000).

[187] Adachi, G.-y. & Imanaka, N. Rare earth contribution in solid state electrolytes, especially in the chemical sensor field. *Journal of Alloys and Compounds* **250**, 492–500 (1997).

[188] Kamaya, N. *et al.* A lithium superionic conductor. *Nature Materials* **10**, 682 (2011).

[189] Seino, Y., Ota, T., Takada, K., Hayashi, A. & Tatsumisago, M. A sulphide lithium super ion conductor is superior to liquid ion conductors for use in rechargeable batteries. *Energy & Environmental Science* **7**, 627–631 (2014).

[190] Hassoun, J. & Scrosati, B. A high-performance polymer tin sulfur lithium ion battery. *Angewandte Chemie International Edition* **49**, 2371–2374 (2010).

[191] Hwa, Y., Zhao, J. & Cairns, E. J. Lithium sulfide (Li_2S)/graphene oxide nanospheres with conformal carbon coating as a high-rate, long-life cathode for Li/S cells. *Nano Letters* **15**, 3479–3486 (2015).

[192] Cai, K., Song, M.-K., Cairns, E. J. & Zhang, Y. Nanostructured Li_2S–C composites as cathode material for high-energy lithium/sulfur batteries. *Nano Letters* **12**, 6474–6479 (2012).

[193] Mori, K. *et al.* Direct observation of fast lithium-ion diffusion in a superionic conductor: $Li_7P_3S_{11}$ metastable crystal. *Physical Review Applied* **4**, 054008 (2015).

[194] Keen, D. & Hull, S. The high-temperature structural behaviour of copper(I) iodide. *Journal of Physics: Condensed Matter* **7**, 5793 (1995).

[195] Hull, S. & Keen, D. Structural characterization of the superionic transition in Ag_2HgI_4 and Cu_2HgI_4. *Journal of Physics: Condensed Matter* **12**, 3751 (2000).

[196] Keen, D. A. & Hull, S. Determination of structural disorder in superionic by neutron total scattering. *Journal of Physics: Condensed Matter* **10**, 8217 (1998).

[197] Hull, S. Superionics: crystal structures and conduction processes. *Reports on Progress in Physics* **67**, 1233 (2004).

[198] Wang, Y. *et al.* Design principles for solid-state lithium superionic conductors. *Nature Materials* **14**, 1026 (2015).

[199] Mohn, C. E., Støl en, S. & Hull, S. Diffusion within α-CuI studied using ab-initio molecular dynamics simulations. *Journal of Physics: Condensed Matter* **21**, 335403 (2009).

[200] Keen, D. *et al.* Nature of the superionic transition in Ag^+ and Cu^+ halides. *Physical Review B* **68**, 014117 (2003).

[201] Chu, I.-H. *et al.* Insights into the performance limits of the $Li_2P_3S_{11}$ superionic conductor: A combined first–principles and experimental study. *ACS Applied Materials & Interfaces* **8**, 7843–7853 (2016).

[202] Zhang, S. & Northrup, J. E. Chemical potential dependence of defect formation energies in GaAs: Application to Ga self-diffusion. *Physical Review Letters* **67**, 2339 (1991).

[203] Van de Walle, C. G., Laks, D., Neumark, G. & Pantelides, S. First-principles calculations of solubilities and doping limits: Li, Na, and N in ZnSe. *Physical Review B* **47**, 9425 (1993).

[204] Persson, C., Zhao, Y.-J., Lany, S. & Zunger, A. n-type doping of $CuInSe_2$ and $CuGaSe_2$. *Physical Review B* **72**, 035211 (2005).

[205] Yildirim, H., Kinaci, A., Chan, M. K. & Greeley, J. P. First-principles analysis of defect thermodynamics and ion transport in inorganic SEI compounds: LiF and NaF. *ACS Applied Materials & Interfaces* **7**, 18985–18996 (2015).

[206] Freysoldt, C., Neugebauer, J. & Van de Walle, C. G. Fully ab initio finite-size corrections for charged-defect supercell calculations. *Physical Review Letters* **102**, 016402 (2009).

[207] Sun, R., Chan, M., Kang, S., Ceder, G. *et al.* Intrinsic stoichiometry and oxygen-induced p-type conductivity of pyrite FeS_2. *Physical Review B* **84**, 035212 (2011).

[208] Blöchl, P. E. Projector augmented-wave method. *Physical Review B* **50**, 17953 (1994).

[209] Moradabadi, A. & Kaghazchi, P. Thermodynamics and kinetics of defects in Li_2S. *Applied Physics Letters* **108**, 213906 (2016).

[210] Altorfer, F. *et al.* Fast ionic diffusion in Li_2S investigated by quasielastic neutron scattering. *Journal of Physics: Condensed Matter* **6**, 9937 (1994).

[211] Yang, Y. *et al.* High-capacity micrometer-sized Li_2S particles as cathode materials for advanced rechargeable lithium-ion batteries. *Journal of the American Chemical Society* **134**, 15387–15394 (2012).

[212] Lide, D. R. *et al. CRC Handbook of Chemistry and Physics* (CRC press, 2012).

[213] Lin, Z., Liu, Z., Dudney, N. J. & Liang, C. Lithium superionic sulfide cathode for all-solid lithium–sulfur batteries. *ACS Nano* **7**, 2829–2833 (2013).

[214] Wenzel, S. *et al.* Interphase formation and degradation of charge transfer kinetics between a lithium metal anode and highly crystalline $Li_7P_3S_{11}$ solid electrolyte. *Solid State Ionics* **286**, 24–33 (2016).

[215] Jand, S. P. & Kaghazchi, P. Theoretical study of cubic-$Li_7La_3Zr_2O_{12}$ (001)/$LiCoO_2$ (10–14) interface. *MRS Communications* **8**, 591–596 (2018).

[216] Jand, S. P. & Kaghazchi, P. First principles study of ion interchange at cubic-$Li_7La_3Zr_2O_{12}$–$LiCoO_2$ interface. *in preparation* (2018).

[217] Munshi, M. Z. A. *Handbook of solid state batteries and capacitors* (World Scientific, 1995).

[218] Nemori, H. *et al.* Stability of garnet-type solid electrolyte $Li_xLa_3A_{2-y}B_yO_{12}$ (A = Nb or Ta, B = Sc or Zr). *Solid State Ionics* **282**, 7–12 (2015).

[219] Zhu, Y., He, X. & Mo, Y. First principles study on electrochemical and chemical stability of solid electrolyte–electrode interfaces in all-solid-state Li-ion batteries. *Journal of Materials Chemistry A* **4**, 3253–3266 (2016).

[220] Sumita, M., Tanaka, Y., Ikeda, M. & Ohno, T. Theoretical insight into charging process in a Li_3PO_4(100)/$LiFePO_4$(010) coherent interface system. *Solid State Ionics* **285**, 59–65 (2016).

[221] Tang, W., Kanoh, H. & Ooi, K. Preparation of lithium cobalt oxide by LiCl flux method for lithium rechargeable batteries. *Electrochemical and Solid-State Letters* **1**, 145–146 (1998).

[222] Koksbang, R., Barker, J., Shi, H. & Saidi, M. Cathode materials for lithium rocking chair batteries. *Solid State Ionics* **84**, 1–21 (1996).

[223] Mizushima, K., Jones, P., Wiseman, P. & Goodenough, J. Li_xCoO_2 ($0<x\leq1$): A new cathode material for batteries of high energy density. *Solid State Ionics* **3**, 171–174 (1981).

[224] Ohzuku, T. & Ueda, A. Why transition metal (di) oxides are the most attractive materials for batteries. *Solid State Ionics* **69**, 201–211 (1994).

[225] Du Pasquier, A., Plitz, I., Menocal, S. & Amatucci, G. A comparative study of Li-ion battery, supercapacitor and nonaqueous asymmetric hybrid devices for automotive applications. *Journal of Power Sources* **115**, 171–178 (2003).

[226] Ohta, S., Kobayashi, T., Seki, J. & Asaoka, T. Electrochemical performance of an all-solid-state lithium ion battery with garnet-type oxide electrolyte. *Journal of Power Sources* **202**, 332–335 (2012).

[227] Sumita, M., Tanaka, Y., Ikeda, M. & Ohno, T. Theoretically designed Li_3PO_4(100)/$LiFePO_4$(010) coherent electrolyte/cathode interface for all solid-state Li ion secondary batteries. *Journal of Physical Chemistry C* **119**, 14–22 (2014).

[228] Sumita, M., Tanaka, Y., Ikeda, M. & Ohno, T. Charged and discharged states of cathode/sulfide electrolyte interfaces in all-solid-state lithium ion batteries. *Journal of Physical Chemistry C* **120**, 13332–13339 (2016).

[229] Haruyama, J., Sodeyama, K., Han, L., Takada, K. & Tateyama, Y. Space–charge layer effect at interface between oxide cathode and sulfide electrolyte in all-solid-state lithium-ion battery. *Chemistry of Materials* **26**, 4248–4255 (2014).

[230] Dudarev, S., Botton, G., Savrasov, S., Humphreys, C. & Sutton, A. Electron-energy-loss spectra and the structural stability of nickel oxide: An LSDA + U study. *Physical Review B* **57**, 1505 (1998).

[231] Ghosh, P., Mahanty, S., Raja, M., Basu, R. N. & Maiti, H. S. Structure and optical absorption of combustion-synthesized nanocrystalline $LiCoO_2$. *Journal of Materials Research* **22**, 1162–1167 (2007).

[232] Kushida, K. & Kuriyama, K. Narrowing of the co-3d band related to the order–disorder phase transition in $LiCoO_2$. *Solid State Communications* **123**, 349–352 (2002).

[233] Rosolen, J. & Decker, F. Photoelectrochemical behavior of $LiCoO_2$ membrane electrode. *Journal of Electroanalytical Chemistry* **501**, 253–259 (2001).

[234] Van Elp, J. *et al.* Electronic structure of coo, li-doped coo, and $LiCoO_2$. *Physical Review B* **44**, 6090 (1991).

[235] Miara, L. J. *et al.* Effect of rb and ta doping on the ionic conductivity and stability of the garnet $Li_{7+2x-y}(La_{3-x}Rb_x)(Zr_{2-y}Ta_y)O_{12}$ ($0 \leq x \leq 0.375$, $0 \leq y \leq 1$) superionic conductor: A first principles investigation. *Chemistry of Materials* **25**, 3048–3055 (2013).

[236] Santosh, K., Longo, R. C., Xiong, K. & Cho, K. Point defects in garnet-type solid electrolyte (c-$Li_7La_3Zr_2O_{12}$) for Li-ion batteries. *Solid State Ionics* **261**, 100–105 (2014).

[237] Jalem, R. *et al.* Concerted migration mechanism in the Li ion dynamics of garnet-type $Li_7La_3Zr_2O_{12}$. *Chemistry of Materials* **25**, 425–430 (2013).

[238] Miara, L. J., Richards, W. D., Wang, Y. E. & Ceder, G. First-principles studies on cation dopants and electrolyte— cathode interphases for lithium garnets. *Chemistry of Materials* **27**, 4040–4047 (2015).

[239] Meier, K., Laino, T. & Curioni, A. Solid-state electrolytes: revealing the mechanisms of Li-ion conduction in tetragonal and cubic llzo by first-principles calculations. *Journal of Physical Chemistry C* **118**, 6668–6679 (2014).

[240] Adams, S. & Rao, R. P. Ion transport and phase transition in $Li_{7-x}La_3(Zr_{2-x}M_x)O_{12}$ (M = Ta^{5+}, Nb^{5+}, x = 0, 0.25). *Journal of Materials Chemistry* **22**, 1426–1434 (2012).

[241] Wolf, D. Reconstruction of NaCl surfaces from a dipolar solution to the Madelung problem. *Physical Review Letters* **68**, 3315–3318 (1992).

[242] Jand, S. P. & Kaghazchi, P. The role of electrostatic effects in determining the structure of LiF-graphene interfaces. *Journal of Physics: Condensed Matter* **26**, 262001 (2014).

[243] Rodrigues, I., Wontcheu, J. & MacNeil, D. Post-synthetic treatments on $Ni_xMn_xCo_{1-2x}(OH)_2$ for the preparation of lithium metal oxides. *Materials Research Bulletin* **46**, 1878–1886 (2011).

[244] Ensling, D., Thissen, A., Laubach, S., Schmidt, P. C. & Jaegermann, W. Electronic structure of $LiCoO_2$ thin films: A combined photoemission spectroscopy and density functional theory study. *Physical Review B* **82**, 195431 (2010).

[245] Okubo, M. *et al.* Nanosize effect on high-rate Li-ion intercalation in $LiCoO_2$ electrode. *Journal of the American Chemical Society* **129**, 7444–7452 (2007).

[246] Kramer, D. & Ceder, G. Tailoring the morphology of $LiCoO_2$: a first principles study. *Chemistry of Materials* **21**, 3799–3809 (2009).

[247] Thompson, T. *et al.* Electrochemical window of the Li-ion solid electrolyte $Li_7La_3Zr_2O_{12}$. *ACS Energy Letters* **2**, 462–468 (2017).